UAV mission planning based on Prognosis & Health Management

Ricardo Schacht Rodriguez

UNIVERSITÉ DE LORRAINE

École doctorale IAEM Lorraine

Planification de la mission des drones basée sur le pronostic et la gestion de la santé

THÈSE

présentée et soutenue publiquement le 2 décembre 2019

pour l'obtention du

Doctorat de l'Université de Lorraine

(mention Automatique)

par

Ricardo SCHACHT-RODRIGUEZ

Composition du jury

Superviseur:	Jean Christophe PONSART - HdR, Professeur Université de Lorraine Carlos Daniel GARÍA-BELTRÁN - Professeur à CENIDET - Mexique Carlos Manuel ASTORGA-ZARAGOZA - Professeur à CENIDET - Mexique
Rapporteurs :	Cristina MANIU - HdR, Professeur Contractuelle à CentraleSupélec John Jairo MARTINEZ-MOLINA - HdR, Maitre de Conférences à Grenoble-INP
Examinateurs :	Tarek RAISSI - HdR, Professeur CNAM Paris Pedro CASTILLO - HdR, CR CNRS, Laboratoire Heudiasyc Philippe WEBER - HdR, Professeur Université de Lorraine
Invité :	Didier THEILLIOL - HdR, Professeur Université de Lorraine

Centre de Recherche en Automatique de Nancy — UMR 7039

Mis en page avec la classe thesul.

UNIVERSITÉ DE LORRAINE

École doctorale IAEM Lorraine

UAV mission planning based on Prognosis & Health Management

THÈSE

présentée et soutenue publiquement le December 2, 2019

pour l'obtention du

Doctorat de l'Université de Lorraine

(mention Automatique)

par

Ricardo SCHACHT-RODRIGUEZ

Composition du jury

Superviseur:	Jean Christophe PONSART - HdR, Professeur Université de Lorraine Carlos Daniel GARÍA-BELTRÁN - Professeur à CENIDET - Mexique Carlos Manuel ASTORGA-ZARAGOZA - Professeur à CENIDET - Mexique
Rapporteurs :	Cristina MANIU - HdR, Professeur Contractuelle à CentraleSupélec John Jairo MARTINEZ-MOLINA - HdR, Maitre de Conférences à Grenoble-INP
Examinateurs :	Tarek RAISSI - HdR, Professeur CNAM Paris Pedro CASTILLO - HdR, CR CNRS, Laboratoire Heudiasyc Philippe WEBER - HdR, Professeur Université de Lorraine
Invité :	Didier THEILLIOL - HdR, Professeur Université de Lorraine

Centre de Recherche en Automatique de Nancy — UMR 7039

Mis en page avec la classe thesul.

To my family

Acknowledgments

This adventure started approximately 4 years and some months ago, and during that time I had the opportunity to meet extraordinary people both Mexico and France...

and it is to all of them that I want to say a big thanks!

If you are reading this and you knew me between at the beginning of April 2015 and at the end of December 2019, just when I was developing my PhD studies, please feel within this recognition. Directly or indirectly you are part of that special group of people who supported me, from the simple fact of listening to me, helping me with my procedures (both Mexico and France), giving me advice, having faith in me, having patience, accompanying me on trips, introducing me to other friends, giving me your friendship, trust and respect... as well as, advising me in the development of this thesis, listening to my ideas and allowing me to grow academically and professionally.

I write this in this way because I do not want to exclude you...

Thank you for so much for everything!

Abstract

Rotorcraft Unmanned Aerial Vehicles (UAV) with take-off and vertical landing capabilities or multirotors have proved to be an efficient and low-cost solution for civil flight applications due to significant advances in the development of robust and more efficient altitude and attitude control strategies, planning and re-planning algorithms capable of detecting and evading obstacles and Fault Diagnosis & Fault Tolerant Control methods.

In most applications where multirotors are used, they develop different task as exploration, photogrammetry, filming, mapping and more recently all those dedicated to precision agriculture such as irrigation and crop monitoring. During the development task, the multirotor executes a mission which consists to fly through a set of paths connected by n reference points or way-points inside a known or unknown area. However, during the mission development, different negative factors decrease the multirotor flight performance such as environmental conditions, occurrence of faults or failures in actuators/sensors and energetic limitations due to the power source constraints. The energetic limitation problem in a multirotor are due to power capabilities that on-board battery can supply.

Due to power and energy requirements, the multirotors are powered by Lithium Polymer batteries which are rechargeable batteries of Lithium-Ion technology. They possess a polymer electrolyte instead of a liquid electrolyte and provide high power and energy densities. However, according to the use due to the number of charge/discharge cycles and other factors like damage provoked by over-discharges, the battery performances tend to decrease. Such decrease or aging causes a reduction in the efficiency of the UAV multirotor flight by decrease the total mission time or flight endurance, and leads to maneuverability problem, which increases the risk of crash and collision.

This thesis topic addresses the issues concerning to battery performances and its influence into the mission and path planning tasks. By considering model-based prognosis techniques and path planning methods, a hierarchy mission planning strategy based on energy consumption is proposed and validated at simulation level considering different flight situations. The UAV performances, as well as its capability to execute and fulfill a mission is weighted by determine the battery State of Health (SoH) which is an index to measure the degradation level of the battery. The SoH helps to estimate the battery Remaining Useful Life (RUL) and establishes the energy limitation by the computation of the Maximum Flight Endurance (MFE). Such information is necessary to path planning generation which not only consider the constraints related to the power source but also the scopes and limitations of the mission to be executed. In addition, the main concern of this thesis are long time-distance missions e.g. exploration or inspection of remote areas where it is fundamental to have a proper use of energy aboard the multirotor.

Résumé étendu en français

Actuellement, les véhicules aériens télépilotés (UAV) avec capacité de décollage et d'atterrissage vertical ou multirotors se sont avérés être une solution efficace et peu coûteuse dans les applications de vol civil grâce aux progrès significatifs dans le développement de méthodes plus efficaces de contrôle, planification et prise de décision. Pour de telles applications, les multirotors développent différentes tâches comme l'exploration, la photogrammétrie, le tournage, la cartographie et plus récemment toutes celles dédiées à l'agriculture de précision comme l'irrigation et le suivi des cultures.

Durant la mission de développement, le multirotor exécute une mission qui consiste à parcourir un ensemble de trajectoires reliées par n points de référence ou way-points dans une zone connue ou inconnue. Cependant, pendant l'accomplissement de la mission, différents facteurs négatifs affectent la performance du véhicule comme les conditions environnementales, l'apparition de fautes ou de pannes et les limitations énergétiques dues aux contraintes de l'alimentation en énergie. Le problème de limitation énergétique dans un multirotor est dû aux capacités de puissance que la batterie embarquée peut fournir.

Les drones multirotors sont propulsés par des batteries Lithium Polymère qui sont des batteries rechargeables de technologie Lithium-Ion. Ils possèdent un électrolyte polymère au lieu d'un électrolyte liquide et fournissent une puissance et une densité d'énergie élevées. Cependant, en fonction de l'utilisation due au nombre de cycles de charge/décharge et d'autres facteurs tels que les dommages provoqués par des décharges excessives, les performances de la batterie ont tendance à diminuer. Une telle diminution ou un tel vieillissement entraîne une réduction de l'efficacité du vol multirotor de l'UAV en diminuant le temps de mission total ou l'endurance du vol, et conduit à un problème de manoeuvrabilité, ce qui augmente le risque d'accident et de collision.

Habituellement, une mission pour tout drone multirotor alimenté par une batterie Li-Po consiste à décoller, en volant à travers un ensemble de chemins reliés par des points de cheminement n à l'intérieur d'un espace de travail sous contrainte qui peut aussi être complètement connu ou inconnu et finalement atterrir. Au début de la mission, la batterie de bord est considérée comme complètement chargée et, au fur et à mesure que le temps de vol s'écoule, la batterie est déchargée jusqu'à atteindre la tension minimale ou Fin de Décharge (EoD). Avant l'atteinte de l'EoD, la mission devrait être terminée et le multirotor a atterri. Le temps qui s'écoule entre le début de la mission et le début de la manifestation d'intérêt est habituellement appelé l'endurance en vol (EF). La figure 1.1-(a) présente un exemple de l'élaboration et de la réalisation attendues d'une mission, où E_0 représente l'énergie totale au début de la mission, E_c est la consommation d'énergie mesurée pendant l'élaboration et E_f représente le reste à la fin.

En outre, au cours du développement de la mission, différents facteurs négatifs affectant les performances de vol sont rencontrés, tels que les conditions environnementales, l'apparition de pannes ou de défaillances dans les composants du véhicule et les limitations énergétiques dues aux capacités de la source d'énergie, comme le montre la figure 1-(b). Problèmes liés à l'atténuation des effets des défaillances et des défaillances des composants du véhicule tels que les actionneurs et les capteurs, ainsi que des perturbations dues aux conditions environnementales, les rafales de vent étant traitées au moyen de contrôleurs de position et d'orientation robustes. Cependant, ces problèmes liés à la consommation d'énergie et à la maximisation du temps de vol sont devenus plus populaires en raison de l'intérêt d'augmenter l'endurance de vol (FE) du véhicule afin d'effectuer des missions de longue durée.

Différentes solutions dédiées à l'augmentation de la consommation d'énergie ont été présentées dans le contexte de la planification des trajets, par exemple les auteurs dans ([113, 114, 196]) ont présenté une méthodologie de génération de trajet énergétique minimum basée sur la minimisation de la consommation énergétique considérant le déplacement du véhicule du point initial à un dernier. Les auteurs dans ([161])

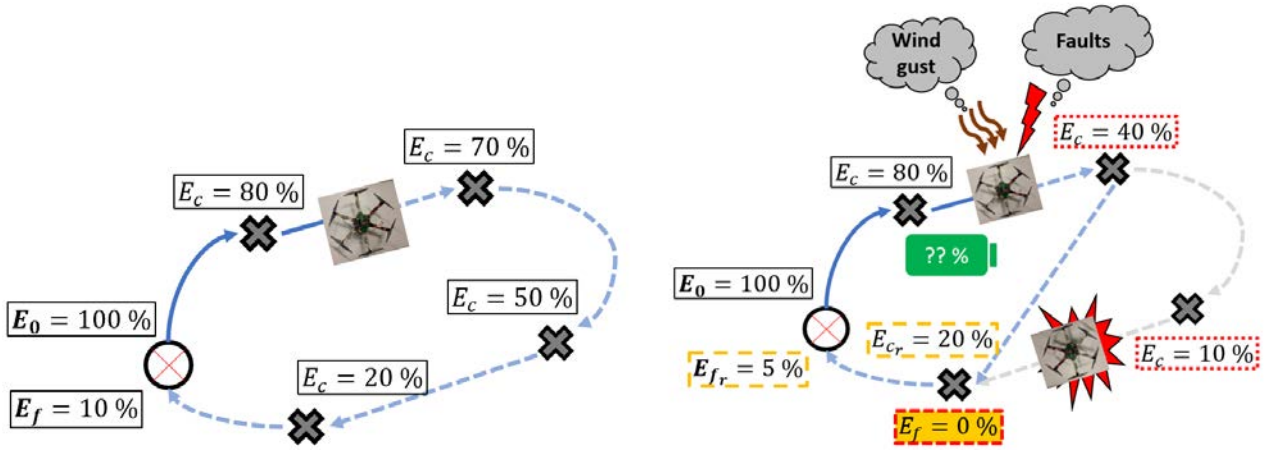

(a) (b)

Figure 1: a) Perspectives d'achèvement d'une mission et b) facteurs négatifs ayant une incidence sur les performances du vol pendant la mission.

et ([164]) rouvrent le problème de génération de chemins d'énergie minimum en ajoutant la dynamique de la décharge de la batterie et sa dépendance de la source d'énergie State of Health. D'autre part, dans ([1, 2, 44, 59, 86]) des modèles mathématiques empiriques pour calculer et maximiser l'endurance de vol en tenant compte de la géométrie du véhicule et des exigences énergétiques pour garder la portance pendant le vol ont été proposés et validés.

Les batteries Li-Po utilisées pour fournir l'énergie nécessaire à l'alimentation du système de propulsion du multirotor (l'ensemble hélice - moteurs brushless DC (BLDCM) - Electronic Control Speed ou ESC) ainsi que d'autres éléments (tels que contrôleur de vol et différents capteurs comme GPS, gyroscope, accéléromètres et RF & Wireless Communication system) est composé pour plusieurs cellules à haute capacité en ampères-heures (Ah Ah) en connexion série. Ils possèdent généralement une plage de tension opérationnelle de 2,5 V (V_{min})à 4,2 V (V_{max}) ([173]) et une tension nominale de 3,7 V. En général, le BLDCM et l'ESC nécessitent une tension de service comprise entre 10 V et 17 V ([45]). En ce sens, il est possible de trouver des batteries avec trois, quatre ou même six cellules en série pour générer des tensions nominales entre 11,1 V et 22,2 V. Afin de générer une force de poussée suffisante pour le décollage du véhicule et de maintenir le véhicule en position stationnaire, les BLDCMs produisent une quantité significative de courant dont l'amplitude augmente le taux de décharge des batteries. Dans la figure 1.2, le courant (ligne bleue) généré par quatre BLDCM d'un quadrotor et la réponse en tension de la batterie (ligne rouge) sont indiqués. Pendant le décollage (entre 0-25 sec), l'augmentation du courant pour atteindre une valeur de 14 A et l'augmentation du taux de décharge de la batterie provoquent une chute de tension de 11,6 V à 11,2 V. Deux changements d'altitude font passer le courant de 14 A à 18 entre 25 - 50 sec et 75 - 100 sec et leurs effets provoquent une chute instantanée de la tension batterie suivie d'une récupération. Enfin, lorsque le quadrotor atterrit, le courant chute à zéro et la tension est rétablie à un niveau proche de la tension initiale.

La batterie utilisée dans la figure 2 a une capacité maximale de 2,2 Ah, ce qui signifie que si la batterie est complètement chargée et qu'un courant de 2,2 A est appliqué pendant une heure, elle se décharge complètement. Si le courant est doublé ou triplé, le temps de décharge diminue. Cet effet est représenté par le taux de décharge de la batterie et il est appelé C-rate [119]. Habituellement, il est possible de calculer l'EF et l'énergie maximales en fonction du courant demandé en évaluant la relation entre le débit C et le temps de décharge comme on peut le voir dans la Figure 3. Cependant, une telle relation n'est valable qu'au début de la vie de la batterie (BoL), et selon le vieillissement de la batterie, la capacité maximale diminue.

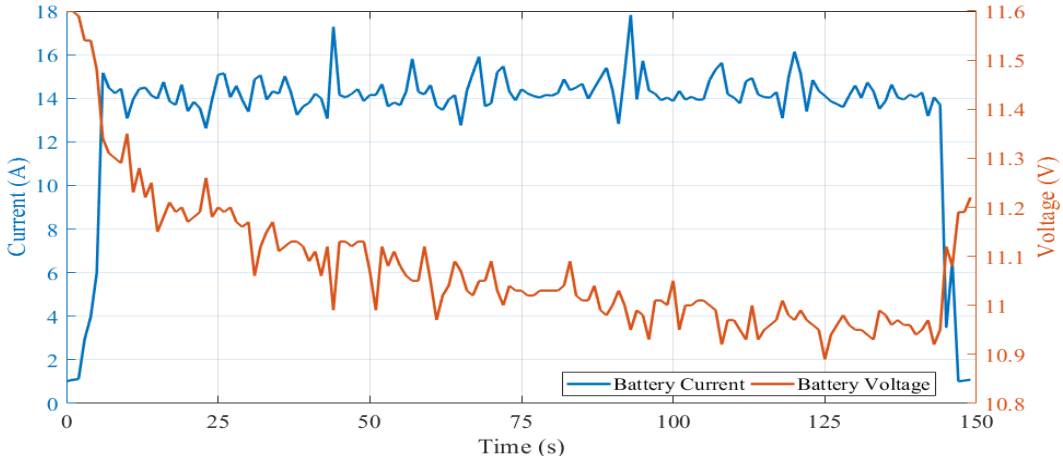

Figure 2: Exemple de décharge de batterie d'un quadrotor en position de vol stationnaire.

De plus, le vieillissement de la batterie est évalué en calculant l'état de santé (SoH) et en fonction des niveaux de SoH, il est possible de déterminer la dégradation réelle de la batterie. L'utilisation continue de la batterie (interprétée comme des cycles de charge/décharge) et des conditions de fonctionnement extrêmes comme un taux de C et une température de décharge élevés, et des décharges profondes, un dommage est provoqué dans la batterie provoquant une dégradation accélérée en réduisant la capacité à stocker l'énergie et à fournir une puissance requise. Une telle dégradation tend également à diminuer la durée de vie utile de la batterie et rend impossible la détermination de l'endurance de vol ou même si une mission peut être lancée et accomplie. De même, une batterie dégradée entraîne des problèmes de manœuvrabilité et un risque élevé d'accident et de collision pendant la mission de développement. L'augmentation des performances de la batterie signifie l'augmentation des capacités de vol multirotor. Dans ce sens, il est nécessaire de prendre en compte les différents aspects négatifs affectant le SoH de la batterie et de l'intégrer dans un cadre de planification de mission.

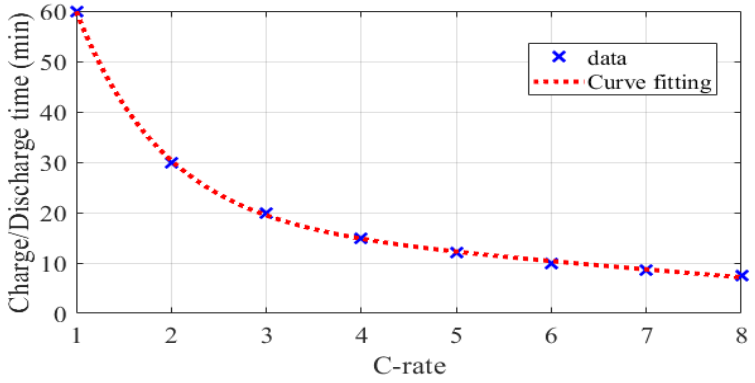

Figure 3: Relation entre le *C-rate* et le temps de chargement/déchargement.

Ce thème de thèse aborde les questions concernant les performances des batteries et leur influence sur les tâches de planification de la mission et de la trajectoire. En considérant les techniques de pronostic basées sur des modèles et les méthodes de planification de trajectoire, une stratégie de planification de mission hiérarchique basée sur la consommation d'énergie est proposée et validée au niveau de la simulation en considérant différentes situations de vol. Les performances du drone, ainsi que sa capacité à effectuer et à

remplir une mission, sont pondérées en déterminant l'état de santé de la batterie (SoH) qui est un indice permettant de mesurer le niveau de dégradation de la batterie. Le SoH aide à estimer la durée de vie utile restante de la batterie (RUL) et établit la limitation d'énergie par le calcul de l'endurance maximale de vol (MFE). De telles informations sont nécessaires à la génération de la planification des trajectoires qui ne prennent pas seulement en compte les contraintes liées à l'utilisation du mais aussi la portée et les limites de la mission à exécuter.

Le document de thèse est organisé comme suit :

- **Chapitre 1**: Ce chapitre présente le contexte général de la thèse en établissant les principaux problèmes des drones multirotors, notamment ceux liés à la consommation d'énergie lors du développement de la mission. De plus, les objectifs atteints ainsi que les contributions (conférences et articles de journaux) de cette recherche ont été sollicités.

- **Chapitre 2**: Ce chapitre présente l'état actuel d'Arte autour de la planification de la mission et de la planification du cheminement basée sur la consommation d'énergie, la méthodologie PHM en particulier le modèle basé sur le pronostic.

- **Chapitre 3**: Ce chapitre présente le modèle mathématique du drone multirotor et présente également le modèle mathématique du système de propulsion : batterie et moteurs. Une boucle de régulation en cascade est conçue pour contrôler la position et l'orientation du véhicule en tenant compte de la relation entre la vitesse angulaire du moteur et le taux de décharge de la batterie.

- **Chapitre 4**: Ce chapitre présente l'élaboration du module Pronostic et gestion de la santé pour estimer le SoC et le SoH et déterminer l'EF pour les objectifs de planification de mission.

- **Chapitre 5**: Ce chapitre présente la planification de la mission proposée et décrit tous les éléments qui l'ont intégrée. De plus, la génération de trajets d'énergie minimum est établie en tenant compte de l'état de santé de la batterie et de ses limites. Enfin, ce chapitre se termine par les résultats de la simulation dans différentes conditions de vol.

- **Chapitre 6**: Ce chapitre présente les perspectives et les travaux futurs de la thèse et met en lumière les contributions.

Contents

List of Figures **III**

List of Tables **VII**

Acronyms **IX**

1 Generalities of topic thesis **1**
1.1 Introduction . . . 1
1.2 Motivation . . . 2
1.3 Objectives and aims of topic thesis . . . 4
1.4 Scope . . . 5
1.5 Contributions and publications . . . 5
1.6 Thesis organization . . . 6
1.7 Conclusion . . . 7

2 State of the Art **9**
2.1 Prognosis and Health Management . . . 10
2.1.1 Prognosis methods . . . 11
2.1.2 Short and Long term predictions . . . 13
2.1.3 PHM in multirotor UAV . . . 14
2.2 Mission planning . . . 16
2.3 Path planning . . . 19
2.4 Conclusions . . . 20

3 Mathematical model of UAV hexarotor **21**
3.1 Multirotor configurations . . . 21
3.2 Hexarotor dynamics . . . 22
3.3 Propulsion system . . . 29
3.3.1 Lithium Polymer battery dynamics . . . 29
3.3.2 BrushLess DC Motor dynamics . . . 31
3.4 Position and orientation controller design . . . 33
3.4.1 Cascade Control Loop (CCL) development . . . 33
3.4.2 Integration of Propulsion system in CCL . . . 37
3.5 Conclusion . . . 43

4 Prognosis and Health Management of multirotor UAV **45**
4.1 Prognosis module . . . 45
4.1.1 State Estimation . . . 46
4.1.2 Propagation and Prediction of estimated states . . . 47
4.2 Multirotor Flight Endurance . . . 49

4.2.1 Endurance model . . . 49
4.2.2 Flight Endurance Prediction . . . 50
4.2.3 SoC estimation . . . 51
4.3 Battery Health prediction . . . 52
4.4 Conclusions . . . 58

5 Energy aware mission planning **59**
5.1 Mission planning strategy . . . 59
5.1.1 Energy consumption of hexarotor . . . 61
5.1.2 Path generation based on energy consumption . . . 62
5.2 Simulation results . . . 74
5.3 Conclusions . . . 82

6 Conclusions and perspectives **83**
6.1 Prognosis and Health Management module . . . 83
6.2 Mission planning and path planning . . . 84

Appendix **86**
Appendix A. Parametrization of lithium battery . . . 87

Bibliography **92**

List of Figures

1 a) Perspectives d'achèvement d'une mission et b) facteurs négatifs ayant une incidence sur les performances du vol pendant la mission. . . . 9
2 Exemple de décharge de batterie d'un quadrotor en position de vol stationnaire. . . . 10
3 Relation entre le *C-rate* et le temps de chargement/déchargement. . . . 10

1.1 (a) Expectation of the fulfillment of a mission and (b) negative factors affecting the flight performance during mission. . . . 2
1.2 Example of battery discharge of a quadrotor in hover position. . . . 3
1.3 Relationship of C-rate and charge/discharge time. . . . 4

2.1 State of Art organization. . . . 9
2.2 Cost associated with different maintenance strategies [74]. . . . 11
2.3 Classification of different prognosis methods [84]. . . . 11
2.4 Application domains of physics-based and data-driven prognostics algorithms [84]. . . . 13
2.5 Evolution of the system behavior. . . . 14
2.6 Single-vehicle mission planning hierarchy [168]. . . . 17
2.7 Multi-vehicles mission planning hierarchy [168]. . . . 17
2.8 Mission intelligent flow [182]. . . . 18
2.9 Autonomous control level trend [182]. . . . 18
2.10 Health management-based hierarchical architecture model for multi-vehicle mission system [183]. . . . 19

3.1 Trirotor flight configurations ([58]). . . . 21
3.2 Quadrotor + and **X** flight configurations ([58]) 22
3.3 (a) Hexarotor + and X flight configuration. (b) Hexarotor coaxial-rotor design configuration ([58]). . . . 22
3.4 (a) Octorotor + and **X** flight configuration. (b) Octorotor V design configuration. (c) Octorotor X flight and coaxial-rotor design configuration ([58]). . . . 23
3.5 Reference frames of the UAV hexarotor. . . . 23
3.6 Propulsion system of multirotor. . . . 29
3.7 Connexion of Li-Po battery - ESC - BLDCM. . . . 29
3.8 Typically Li-Po battery used in multirotor UAV applications. . . . 30
3.9 Electrical equivalent circuit of Li-Po battery. . . . 30
3.10 Interaction between propulsion system and hexarotor dynamics. . . . 32
3.11 Hexarotor Cascade Control Loop. . . . 34
3.12 Result of hexarotor stabilization. . . . 35
3.13 Control inputs. . . . 35
3.14 (a) Hexarotor position $x-y-z$ axis. (b) Hexarotor orientation $\phi-\theta-\psi$ angles. . . . 37
3.15 (a) Control inputs. (b) Angular speed of BLDCMs. . . . 37
3.16 (a) Hexarotor position $x-y-z$ axis. (b) Hexarotor orientation $\phi-\theta-\psi$ angles. . . . 38
3.17 Control inputs. . . . 39

3.18 Angular speed of BLDCMs. . . . 39
3.19 (a) Duty Cycle per BLDCM. (b) Demanded current per BLDCM. . . . 40
3.20 Battery response: current, voltage and State of Charge. . . . 40
3.21 Hexarotor position in 3D view for a complete path. . . . 41
3.22 (a) Hexarotor position $x-y-z$ axis. (b) Hexarotor orientation $\phi-\theta-\psi$ angles. . . . 41
3.23 Control inputs. . . . 42
3.24 Angular speed of BLDCMs. . . . 42
3.25 (a) Duty cycle per BLDCM. (b) Demanded current per BLDCM. . . . 43
3.26 Battery response: current, voltage and State of Charge. . . . 43

4.1 Prognosis and Health Management scheme in multirotor UAV. . . . 46
4.2 Model-based Prognosis methodology. . . . 47
4.3 Evolution of the system behavior. . . . 47
4.4 Relationship of C-rate and time. . . . 50
4.5 (a) Voltage variation of a cell subjected to discharge cycles. (b) Evolution of capacity C_T and (c) Internal resistance R_{int} ([153]). . . . 53
4.6 Fitting of capacity loss with polynomial functions. . . . 54
4.7 (a) Evolution of Capacity loss C_T. (b) Identification of Capacity loss model. . . . 54
4.8 (a) Evolution of internal resistance R_{int} according to N_{cycle}. (b) Identification of power fade model. . . . 55
4.9 Safety Voltage Threshold of the Li-Po battery. . . . 56
4.10 3D Path of hexarotor UAV. . . . 56
4.11 (a) Demanded current I_{batt} and (b) comparison between battery voltage and $\hat{V}_{batt}$. . . . 56
4.12 Comparison between SoC_{CC} and $\hat{SoC}$. . . . 57
4.13 Comparison between the predictions of both prediction functions. . . . 57
4.14 Prediction of flight endurance with 1^{st} order polynomial. . . . 58
4.15 Prediction of flight endurance with 2^{st} order polynomial. . . . 58
4.16 RMT staring from the first prediction. . . . 58

5.1 Structure of mission planning based on Prognosis module for flight Endurance estimation. 60
5.2 Example of crop irrigation path for multirotors. . . . 61
5.3 Example of path generation with polynomial function. . . . 64
5.4 Example of multi-segment path ([37]) . . . 65
5.5 (a) Example of path in 3D. (b) Path in x-y plane. . . . 65
5.6 Compassion of battery response between Stop-and-go and Continuous motion. . . . 66
5.7 Energy battery . . . 67
5.8 (a) Interaction of different dynamics in hexarotor. (b) Control system with reference angular speed . . . 68
5.9 Case 1: 3D Position around $x-y-z$ axis. . . . 70
5.10 Case 1: Position and linear speed around $x-y-z$ axis. . . . 71
5.11 Case 1: Orientation and angular speed around Euler angles $[\phi\,\theta\,\psi]$. . . . 71
5.12 Case 1: Battery response. . . . 72
5.13 Case 1: Battery temperature. . . . 72
5.14 Case 2: Position and linear speed around $x-y-z$ axis. . . . 73
5.15 Case 2: Hexarotor position and linear speed around $x-y-z$ axis. . . . 73
5.16 Case 2: Battery response. . . . 74
5.17 Comparison of battery response between minimization problem and polynomial approach. 75
5.18 Structure of mission planning based on Prognosis module for flight Endurance estimation. 75
5.19 Area to cover and safety zone. . . . 76
5.20 Minimum energy path and way-points. . . . 76

5.21 Results of the tracking controller. 77
5.22 Battery response: current and voltage. 77
5.23 State of Charge estimation. 78
5.24 Remaining Mission Time and maximum Flight Endurance. 78
5.25 Comparison between battery current (a) and voltage (b) in healthy and faulty situation. . 79
5.26 Battery State of Charge at nominal and faulty case (a) and Remaining Mission Time (b). 80
5.27 Battery battery current with reconfiguration of fault in actuator 1. 81
5.28 Battery battery current with reconfiguration of fault in actuator 2. 81
5.29 Battery SoC after reconfiguration. 81
5.30 Remaining Mission Time after reconfiguration. 82

6.1 Equivalent Circuit Model of Li-Po battery. 87
6.2 Discharge current profile and battery voltage. 88
6.3 State of charge of the demanding current. 89
6.4 Relationship between the SoC and the open circuit voltage. 89
6.5 Relationship between the SoC and the open circuit voltage. 89
6.6 Comparison 1 between the mathematical model and experimental data. 91
6.7 Comparison 2 between the mathematical model and experimental data. 91

List of Tables

4.1 Coefficients of identified models 55

5.1 Boundary conditions of trajectory 63
5.2 Results of multi-objective minimization problem with SoH variations. 74

6.1 Characteristics of the battery 87
6.2 Parameters of the battery model 90

Acronyms

Ah Ampere-hour

CBM Condition Based Maintenance

CCL Cascade Control Loop

CM Corrective Maintenance

BLDCM BrushLess DC Motor

ECM Equivalent Circuit Model

EKF Extended Kalman Filter

ESC Electronic Speed Control

EoD End of Discharge

FE Flight Endurance

Li-Po Lithium Polymer

LCC Life Cycle Cost

MFE Maximum Flight Endurance

PHM Prognosis and Health Management

PID Proportional-Integral-Derivative

PM Preventive Maintenance

PWM Pulse-Width Modulation

RMT Remaining Mission Time

RUL Remaining Useful Life

RVM Relevance Vector Machine

SoC State of Charge

SoH State of Health

SVM Support Vector Machine

SVT Safety Voltage Threshold

UAV Unmanned Aerial Vehicle

Chapter 1

Generalities of topic thesis

1.1 Introduction

Nowadays, Unmanned Aerial Vehicles (UAV) with take-off and vertical landing capabilities or multirotors have proved to be an efficient and low-cost solution in civil flight applications due to significant advances in the development of more effective control, planning and make decision methodologies. For such applications, multirotors develop different task as exploration, photogrammetry, filming, mapping and more recently all those dedicated to precision agriculture such as irrigation and crop monitoring [40, 57, 65, 108, 130, 141, 199].

During the development task, the multirotor executes a mission which consists to fly through a set of paths connected by n reference points or way-points inside a known or unknown area. However, during the mission fulfillment, different negative factors affect the vehicle performance as environmental conditions, occurrence of faults or failures and energetic limitations due to the power source constraints. The energetic limitation problem in a multirotor are due to power capabilities that on-board battery can supply.

The UAV multirotors are powered by Lithium Polymer batteries which are rechargeable batteries of Lithium-Ion technology. They possess a polymer electrolyte instead of a liquid electrolyte and provide high power and energy densities. However, according to the use due to the number of charge/discharge cycles and other factors like damage provoked by over-discharges, the battery performances tend to decrease. Such decrease or aging causes a reduction in the efficiency of the UAV multirotor flight by decrease the total mission time or flight endurance, and leads to maneuverability problem, which increases the risk of crash and collision.

This thesis topic addresses the issues concerning to battery performances and its influence into the mission and path planning tasks. By considering model-based prognosis techniques and path planning methods, a hierarchy mission planning strategy based on energy consumption is proposed and validated at simulation level considering different flight situations. The UAV performances, as well as its capability to carry out and fulfill a mission, is weighted by determine the battery State of Health (SoH) which is an index to measure the degradation level of the battery. The SoH helps to estimate the battery Remaining Useful Life (RUL) and establishes the energy limitation by the computation of the Maximum Flight Endurance (MFE). Such information is necessary to path planning generation which not only consider the constraints related to the power source but also the scopes and limitations of the mission to be executed.

1.2 Motivation

Usually, a mission for any multirotor UAV powered by a Li-Po battery consists of take-off, flying through a set of paths connected by n way-points inside a constraint workspace which can be also completely known or unknown and finally landing. At the beginning of the mission the on-board battery is considered fully charged and as the flight time elapses the battery is discharged until reach the minimum voltage or End of Discharge (EoD). Before the EoD is reached, the mission is expected to be completed and the multirotor has landed. The time between the beginning of mission and the EoD is usually referred as Flight Endurance (FE). An example of the expected development and fulfillment of a mission can be seen in Figure 1.1-(a) where E_0 represents the total energy at the beginning of the mission, E_c is the energy consumption measured during the mission development and E_f represents the remainder energy at the end of the mission.

In addition, during the mission development different negative factors affecting the flight performances are encountered as environmental conditions, the occurrence of faults or failures in vehicle components and energetic limitations due to the power source capabilities as it is shown in Figure 1.1-(b). Problems related to the mitigation of the fault and failure effects in vehicle components such as actuators and sensors, as well as disturbances due to environmental conditions as wind gusts are addressed by means of robust position and orientation controllers ([53, 187, 209]) and Fault Tolerant Control ([77, 127, 151]). However, those problems related to energy consumption and maximization of flight time have become more popular due to the interest to increase the vehicle Flight Endurance (FE) in order to perform long time missions.

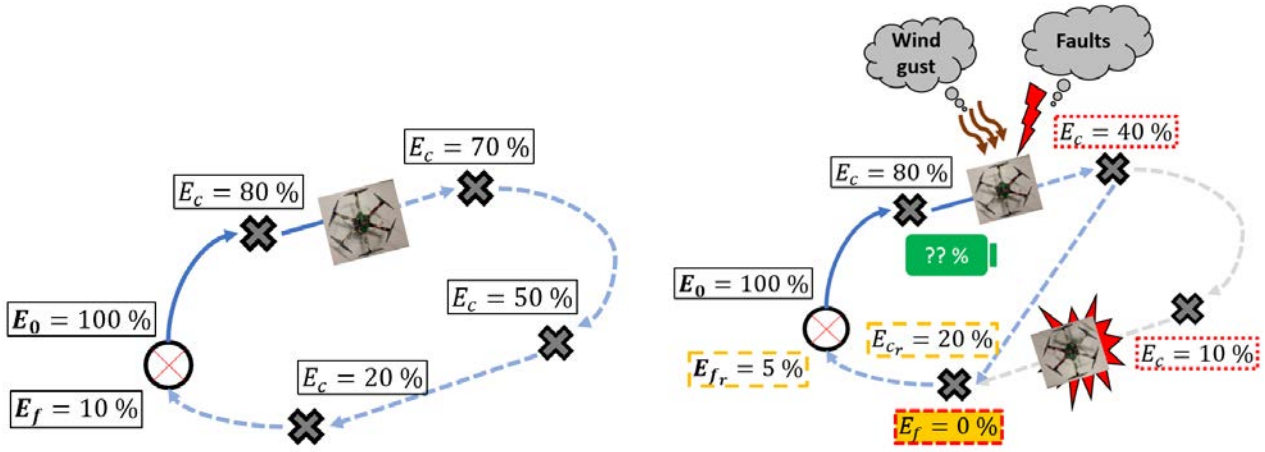

(a) (b)

Figure 1.1: (a) Expectation of the fulfillment of a mission and (b) negative factors affecting the flight performance during mission.

Different solutions dedicated to increase the FE have been presented in the context of path planing, e.g. the authors in [113, 114, 196] presented a minimum energy path generation methodology based on the minimization of energy consumption considering the vehicle displacement from an initial to a final point. The authors in [161] and [164] reopen the generation of minimum energy paths problem by adding the dynamics of the battery discharge and its dependency of power source State of Health. On the other hand in [1, 2, 44, 59, 86] empirical mathematical models to compute and maximize the flight endurance taking into account the vehicle geometry and energetic requirements to keep the lift during the flight have been proposed and validated.

The Li-Po batteries used to supply the energy to powered the propulsion system of multirotor (the ensemble

propeller - BrushLess DC motors (BLDCM) - Electronic Control Speed or ESC) as well as other elements (such as flight controller and different sensors like GPS, gyroscope, accelerometers and RF & Wireless Communication system) is composed for several cells with high capacity in Amperes-hours (Ah) in series connection. Usually they possess a voltage operational range of 2.5 V (V_{min})to 4.2 V (V_{max}) [173] and a nominal voltage of 3.7 V. Generally, the BLDCM and ESC require an operating voltage level between 10 V and 17 V [45]. In that sense it is possible to find batteries with three, four or even six cells in series connection to generate nominal voltages levels between 11.1 V to 22.2 V. In order to generate sufficient thrust force for the vehicle take-off and to keep the vehicle in hover position, the BLDCMs generates a significant amount of current whose magnitude increase the battery discharge rate. In Figure 1.2 the current (blue line) generated by four BLDCM of a quadrotor and battery voltage response (red line) are shown. During the take-off (between 0-25 sec) the current increase to reach a value of 14 A and the battery discharge rate increase causing a voltage drop from initial voltage 11.6 V to 11.2 V. Two altitude changes increase the current from 14 A to 18 between 25- 50 sec and 75 - 100 sec and their effects cause an instant drop in the battery voltage followed by a recovery effect. Finally, when the quadrotor lands, the current drops to zero and the voltage is recovered close to initial voltage.

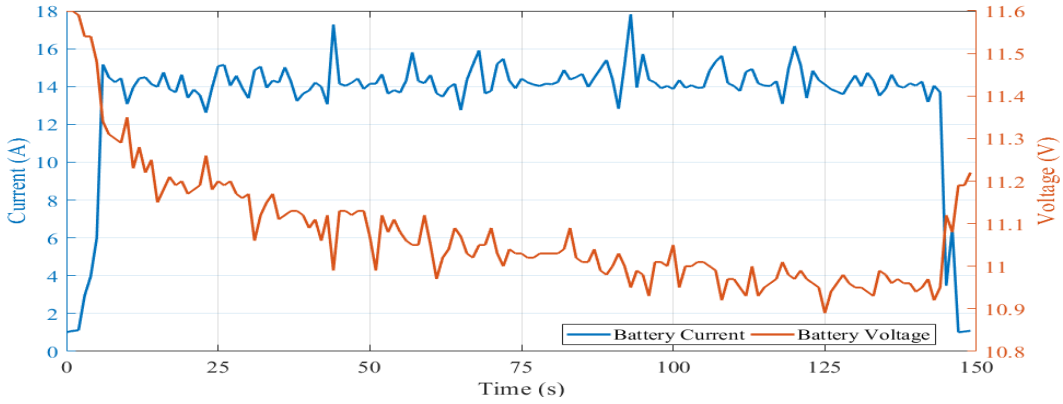

Figure 1.2: Example of battery discharge of a quadrotor in hover position.

The battery used in Figure 1.2 has a maximum capacity of 2.2 Ah which means that if the battery is fully charged and a current of 2.2 A is applied during one hour the battery will be completely discharged. If the current is increased to double or triple, the discharge time decreases. Such effect is represented by battery discharge rate and it is called as C-rate [119]. Usually, it is possible to compute the maximum FE and energy according to demanded current by evaluate the relationship between the C-rate and discharge time as it can be seen in Figure 1.3. However, such relationship is just valid at the battery Begin of Life (BoL), and according to battery aging the maximum capacity decreases. In addition the battery aging is evaluated by computing the State of Health (SoH) and according to SoH levels, it is possible to determines the actual battery degradation. The ongoing use of the battery (interpreted as charge/discharge cycles) and extreme operating conditions like high discharge C-rate and temperature, and deep discharges, a damage is provoked in the battery causing an accelerated degradation by reducing the ability to store energy and supply a required power. A such degradation also tends to decrease the battery useful life and make it impossible to determinate the flight endurance or even if a mission can be launched and fulfilled. Likewise, a degraded battery leads to generation of maneuverability problems and a high risk of crash and collision during the development mission. The increase of battery performance means the increase of multirotor flight capabilities. In that sense it is necessary to take into account the different negative aspects affecting the battery SoH and integrate it in a mission planning framework.

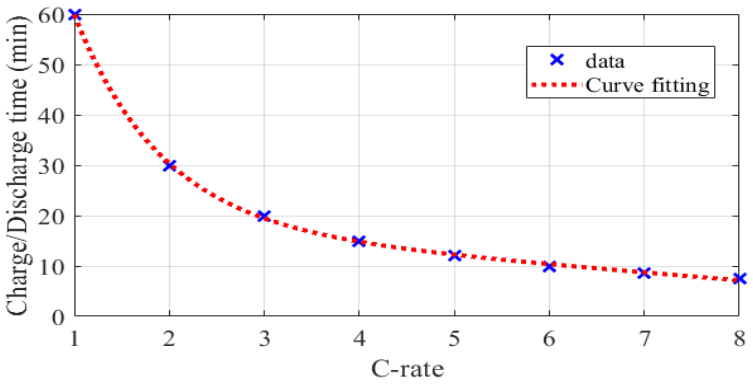

Figure 1.3: Relationship of C-rate and charge/discharge time.

1.3 Objectives and aims of topic thesis

With the aim to establish an appropriate energy consumption during the mission development for multi-rotor vehicle with vertical take off and landing capabilities and at the same time to maximize the useful life time of the battery, the present investigation has as a general objective:

To develop a mission planning and re-planning methodology based on energy consumption and battery State of Health (SoH).

The mission planning and re-planning encompasses from the definition of the requirements of the mission (maximum flight height, speed of displacement, stop and follow), the path planning task for trajectory generation and way-points definition. Within of mission planning routines, the main target is the path planning task which addresses the generation of minimum energy paths. Such paths are considered in order to execute efficient low energy consumption flights. In addition, the mission planning methodology ensure:

- Identify the energy limitations of multirotor UAV during mission development
- Improve the multirotor flight capabilities by taking into account the energy consumption.
- Maximize the Flight Endurance (FE) in order to have long-time mission for general applications (surveillance, exploring, mapping and photogrammetry).

On the other hand, the battery State of Health (SoH) is evaluated by developing empirical degradation models which are will be able to:

- Establish the basics of battery health in UAV applications.
- Model the two main degradation phenomena affecting battery life: capacity loss and power fade.
- Determine the Remaining Useful Life (RUL) of battery associated to number of flights.

Considering that the mission planning has the objective to maximize the FE while the analysis of battery SoH is to determine the RUL, it is necessary to establish the link between both objectives. In that sense, a PHM is proposed and developed considering model-based Prognosis techniques. The PHM scheme (also called Prognosis Module or PM) execute the following tasks:

- Estimation of battery State of Charge (SoC).
- Computation of battery SoH by using degradation models.
- Prediction of FE during mission development and computation of Remaining Mission Time (RMT).

1.4 Scope

The main scope of this thesis is to evaluate at mission and path planning level the effect of the energy consumption by considering the modeling of the power source and the evaluation of its State of Health and use such information to create a hierarchy control structure able to re-planning the mission or path according to energy constraints. Likewise, the proposed methodology is validated at simulation level considering realistic flight situations.

1.5 Contributions and publications

The main contributions of this topic thesis are:

1. Generation of empirical degradation models able to predict the RUL and EoL of Lithium Polymer battery.
2. Development of a mission planning and re-planning strategy able to consider the energy minimization and battery SoH.

Along of thesis developments, several publications were made both international congress and journals. Such works describe the main elements of general contribution that this research presents:

Journals

- **Schacht-Rodríguez, R.**, Ponsart, J. C., García-Beltrán, C. D., Astorga-Zaragoza, C. M., Theilliol, D., & Zhang, Y. (2018). Path planning generation algorithm for a class of uav multirotor based on state of health of lithium polymer battery. Journal of Intelligent & Robotic Systems, 91(1), 115-131.

- **Schacht-Rodríguez, R.**, Ortiz-Torres, G., Garcia-Beltran, C. D., Astorga-Zaragoza, C. M., Ponsart, J. C., & Perez-Estrada, A. J. (2018). Design and development of an UAV Experimental Platform. IEEE Latin America Transactions, 16(5), 1320-1327.

- Torres-Ortíz, G., **Schacht-Rodríguez, R.**, Reyes-Reyes, J., Garcia-Beltran, C. D., Sanchez-Guerrero, M. E., & Astorga-Zaragoza, C. M. (2018). Development of Experimental Platform for Control System of a Planar Vertical Take-off and Landing Unmanned Aerial Vehicle. IEEE Latin America Transactions, 16(2), 342-349.

Conferences

- **Schacht-Rodríguez, R.**, Ortiz-Torres, G., Garcia-Beltran, C. D., Astorga-Zaragoza, C. M., Ponsart, J. C., & Theilliol, D. (2017, June). SoC estimation using an Extended Kalman filter for UAV applications. In 2017 International Conference on Unmanned Aircraft Systems (ICUAS) (pp. 179-187). IEEE.

- **Schacht-Rodríguez, R.**, Ponsart, J. C., Theilliol, D., García-Beltrán, C. D.,& Astorga-Zaragoza, C. M. (2018, September). Path Planning Based on State-of-Health of the Power Source for a Class of Multirotor UAVs. In 2018 UKACC 12th International Conference on Control (CONTROL) (pp. 309-314). IEEE.

- **Schacht-Rodríguez, R.**, Ponsart, J. C., García-Beltrán, C. D., Astorga-Zaragoza, C. M., (2018, August). Prognosis & health management for the prediction of UAV flight endurance. In 10th IFAC Symposium on Fault Detection, Supervision and Safety for Technical Processes, SAFEPROCESS 2018.

- **Schacht-Rodríguez, R.**, Ponsart, J. C., García-Beltrán, C. D., Astorga-Zaragoza, C. M., & Theilliol, D. (2019, June). Mission Planning Strategy for Multirotor UAV Based on Flight Endurance Estimation. In 2019 International Conference on Unmanned Aircraft Systems, ICUAS 2019. IEEE

- **Schacht-Rodríguez, R.**, Ponsart, J. C., García-Beltrán, C. D. & Astorga-Zaragoza, C. M (2019 September). Analysis of energy consumption in multirotor UAV under actuator fault effects. In 4th International Conference on Control and Fault-Tolerant Systems (SysToL 2019). IEEE

Awards

- BEST STUDENT PAPER AWARD - 12th UKACC International Conference on Control (Control 2018), Sheffield, UK

1.6 Thesis organization

The thesis document is organized as follows:

- **Chapter 2**: This chapter presents the actual State of the Art around the mission planning and path planning based on energy consumption, PHM methodology particularly model based Prognosis.

- **Chapter 3**: This chapter presents the mathematical model of multirotor UAV and also introduce the mathematical model of propulsion system: battery and motors. A cascade control loop is designed to control the vehicle position and orientation taking into account the relationship between the angular speed of motor and the battery discharge rate.

- **Chapter 4**: This chapter introduces the development of Prognosis and Health Management module to estimate the SoC and SoH and determines the FE for mission planning objectives.

- **Chapter 5**: This chapter describes the proposed mission planning and describes all elements integrated it. In addition the generation of minimum energy paths is established considering the battery health and its limitations considering also the effect of fault in actuators and the introduction of an ideal FTC strategy based on control allocation method. Finally, this chapters concludes with the simulation results at different flight conditions.

- **Chapter 6**: This chapter enlists the perspectives and future works of topic thesis and highlighting the contributions.

1.7 Conclusion

In this chapter the general context of topic thesis is presented by establishing the issues in mission planning and path planning for multirotors UAV, specifically those related to energy consumption during the mission development. In addition, the reached objectives as well as the contributions (conference and journals papers) of this research were enlisted. In the next Chapter the State of the Art around topic research will be presented.

Chapter 2

State of the Art

In this chapter the more recent works about Prognosis and Health Management (PHM) and Mission Planning in multirotors UAV are described. Such works constitute the core of the thesis State of Art, and they allow to locate the problem as well as the explored solutions that thesis topic is addressing. In Figure. 2.1 the main such topics and their relationship between them are shown. As it can be observed, the link between the mission planning and PHM techniques allows to increase the mission reliability in multirotor UAV and to improve the flight capabilities. The more recent developments around the *Prognosis and Health Management* as Model-based Prognosis techniques, State of Health (SoH) computation and Remaining Useful Life (RUL) prediction dedicate to power source of multirotor UAVs will be described in Section 2.1. On the other hand, in Section 2.2 the different elements comprising of Mission planning problem as mission requirements, motion and path planning as well as the different proposed algorithms around the context of multirotor UAV are presented.

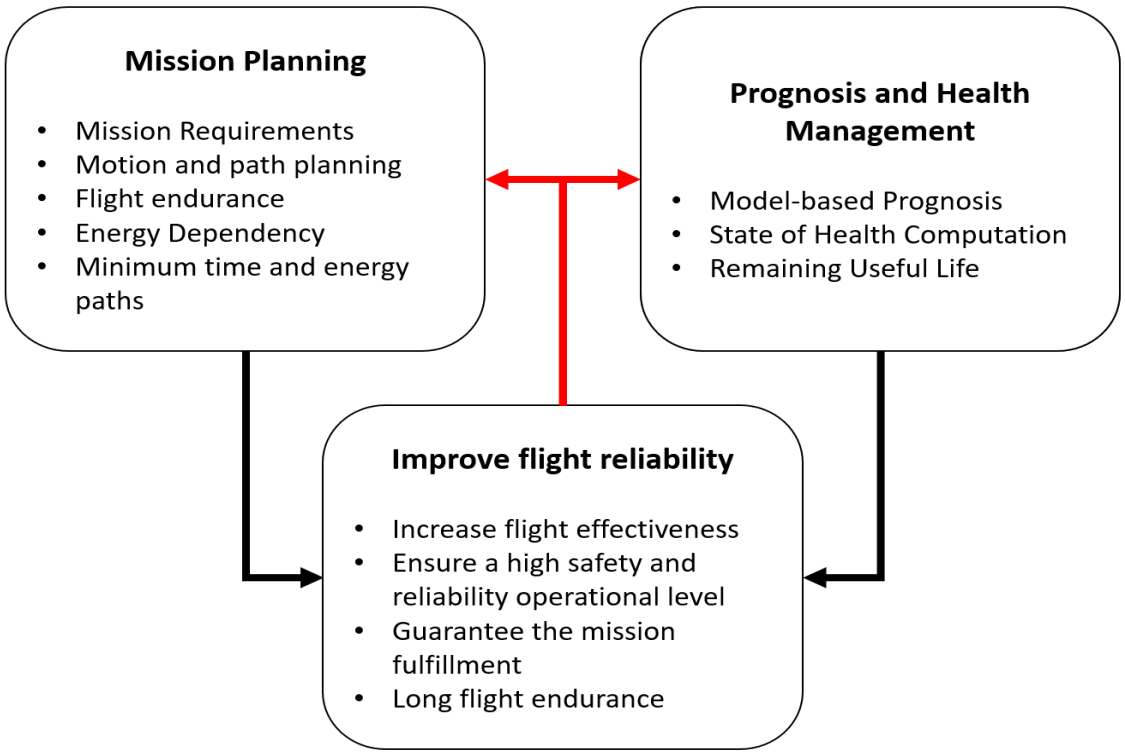

Figure 2.1: State of Art organization.

2.1 Prognosis and Health Management

The Prognosis and Health Management ([62, 74, 84]) or PHM has recently emerged as a key technology which uses data analysis or model based techniques to assess the actual health conditions of an engineered system (health reasoning) and predict *how* and *when* the system is likely to fail (health prognosis) by evaluate the lifetime of the system. In addition, the necessity of PHM is being considered by the growing demand of Condition based Maintenance (CBM) and extension of operational life in high-value engineered systems like nuclear power plants, wind turbines, pipelines, satellites and aircraft. One of the main objectives of the PHM is to predict how the system will behave in the future in order to know if more stress or changes in the nominal operations on the system will likely cause an acceleration towards a certain undesirable *event* or *failure condition*, and the time when such event will occurs. The obtained prediction is used to compute the Remaining Useful Life (RUL) of the component and/or system. According to [73] the PHM is developed by executing four basic functions:

- Health Sensing: acquire sensor signals for an engineered system by in-situ monitoring techniques and to ensure a high likelihood of damage detection.
- Health Reasoning: extract health-relevant system information from the acquire sensor signals using feature extraction techniques and to classify system health states by using health classification techniques.
- Health Prognosis: define a threshold for each unusual or abnormal state and predict the RUL, i.e., the amount of time remaining before the system can not longer performance its required functions.
- Health Management: enable optimal decision making on maintenance of the system based on the RUL prediction to minimize the Life Cycle Cost (LCC).

In addition, other works like [84] define that the necessary steps to develop the PHM includes:

- Data acquisition: collect measurements data from sensors and process them to extract useful features for diagnosis.
- Diagnostics: a fault is detected for any abnormal state, isolated to determine which component is failing and identified in order to know how severe it is with respect to the failure threshold.
- Prognostics: predict how long it will take until failure under the current operating conditions.
- Health Management: manage in optimal manner the maintenance scheduling and logistics support.

Among previous steps, prognostics is the key enabler that permits the reliability of a system to be evaluated in its actual life cycle conditions. In other works, it predicts the time at which a system or a component will no longer perform its intended function, thus giving users the opportunity to mitigate system level risks while extending its useful life.

Nowadays, most maintenance systems applied to engineered systems are either corrective (repairing or replacing a system after it fails) or preventive (inspecting a system on a routine schedule regardless of whether inspection is actually needed). The former strategy is called corrective maintenance (CM) and the latter is called preventive maintenance (PM). Both approaches are expensive and incur high LCCs. PHM meanwhile, uses sensor signals from a system in operation to assess the actual health of the system and predict when and how the system is likely to fail. The health and life information provide by PHM enables field engineers to take a maintenance action only when needed. This is referred to as a condition based maintenance (CBM) strategy. CBM often results in a lower LCC than CM and/or PM strategies as it can be seen in Figure 2.2.

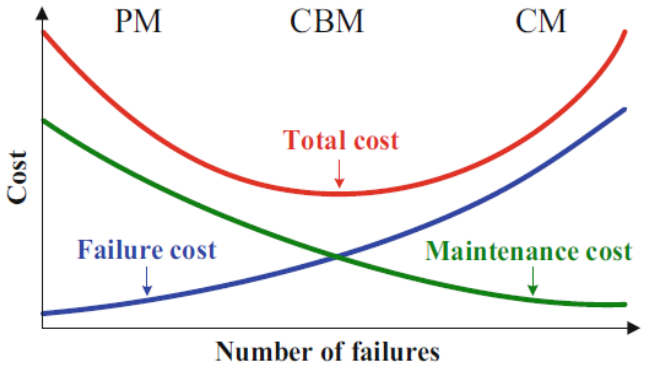

Figure 2.2: Cost associated with different maintenance strategies [74].

2.1.1 Prognosis methods

Generally, PHM methods can be classified into [172]: physics model-based, data-driven, reliability-based and probability-based methods. The applicability of each of these methods depends mainly on the knowledge of the system. However the main methods emerging today and offering a high prediction level of future health state are physics based and data driven approaches [9] as it can be seen in Figure. 2.3.

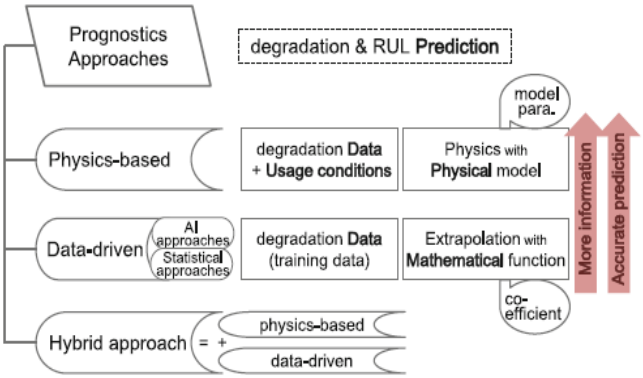

Figure 2.3: Classification of different prognosis methods [84].

Model-based Prognosis methods

Model-based Prognosis or Physics-based approaches ([41, 78, 94, 133]) combine a mathematical model (also called physics model in PHM literature) describing the behavior of the system degradation and measured data containing information about usage conditions. The data allows to identify model parameters to predict the future behavior. The final result is a degradation model describing the main aging phenomena and failure modes. Once a degradation model is developed, it can be reused for different systems or different designs by tuning model parameters. The method is generally considered as computationally efficient that data-driven method. however, model development requires a thorough understanding of the system. If any important physical phenomenon is missed, then it can lead to failure of predicting degradation behavior. Also, high fidelity models, especially for numerical models can be computational intensive.

Since the behavior of damage depends on model parameters in Model-based Prognosis approaches, identifying them is the most important issue in predicting future damage behaviors. Due to uncertainty in usage conditions and noise in data, most algorithms identify model parameters as probability distributions rather than deterministic values based on Bayesian inference ([21]) that is a statistical method in which observations are used to estimate and update unknown model parameters in the form of a probability density function. The most typical technique is the particle filter ([124, 125, 190]) that expresses the distribution of parameters with a number of particles and their weights based on sequential Bayesian updating. The Kalman filter is also a filtering method based on the sequential Bayesian updating, which gives the exact posterior distribution in the case of a linear system with Gaussian noise. Other Kalman filter family techniques, such as extended/unscented Kalman filter have been developed to improve the performance for nonlinear systems ([27, 97, 207]). Finally, the nonlinear least squares ([54]) that is a nonlinear version of the least squares is often used, but in which the parameters are estimated with deterministic values and their variances.

Data-driven methods

Data-driven approaches use informations from collected data at current and previous usage conditions (usually called training data) to identify the characteristics of the currently measured degradation state and to predict the future trend ([13, 63, 72, 116, 166]). The conceptual understanding for data-driven approaches is an extrapolation with mathematical functions based on identified coefficients. Since this approach simply fits the trend of data, there is no guarantee that the extrapolation will be meaningful since failure progression from current state forward may be unrelated to prior failure progression. The success of data-driven methods depends on collecting statistics of failure as a function of current state, which requires large volume of data. Without having a comprehensive understanding of the system, it is difficult to know how much data are sufficient for the purpose of prognosis.

The most common techniques in data-driven approaches, is the artificial neural network (so-called neural network) as an artificial intelligence method, in which a network model learns a way to produce a desired output, such as the level of degradation or lifespan, by reacting to given inputs, such as time and usage conditions ([150, 167, 170]). Also, the Gaussian process (GP) regression ([89, 156]) is a commonly used method among regression-based data-driven approaches, which is a linear regression like the least squares method with the assumption that errors between a regression function and data are correlated. Including the least squares regression, there are a wide variety of algorithms such as the fuzzy logic ([159, 169]), relevance/support vector machine (RVM/SVM) ([23, 43]), gamma process ([64, 201]), Wiener processes ([192, 202]), hidden Markov model ([47, 206]) and deep-learning ([82, 204]).

In the viewpoint of practicality, data-driven approaches are easy and fast to implement. In fact, several off-the-shelf packages are available for data mining and machine learning. By collecting enough data, it is possible to identify relationships that were not previously considered. Also, since the method works with objective data, it can consider all relationships without any prejudice. However, this method requires a lot of data that include all possible modes of failure for the same or similar systems. Since no physical knowledge is involved, the results may be counter-intuitive and it is dangerous to accept a result without understanding the cause of the problem. The method can be computationally intensive, in both analysis and implementation. In addition, the application domains of both model-based and data-driven methods can be illustrated in terms of reliability of physics model and availability of data, as shown in Figure 2.4. When a highly reliable physics model is available, physics-based approaches will work well even with a small number of data. When much data are available, both methods can be applied. The issue is when a reliable physics model is not available. In this case, if much data are available, then data-driven approach can be applied without requiring physics model. However, if a small number of data are available, there is no reliable prognostics approaches and thus health assessment will be unreliable.

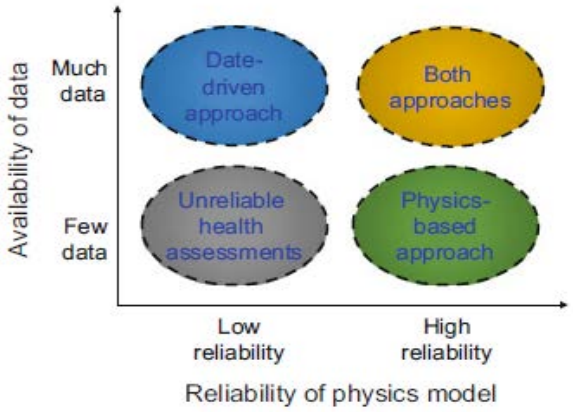

Figure 2.4: Application domains of physics-based and data-driven prognostics algorithms [84].

On the other hand, hybrid approaches ([55, 56, 134]) integrate advantages of both physics-based and data-driven methods to improve the prediction capability. For practical complex systems, it might not be efficient to use physics-based or data-driven approaches alone. Instead, both approaches are used together to maximize the prediction capability. For example, the knowledge on physical behavior can be used to determine the mathematical model (e.g., determining the order of polynomial or exponential functions) in data-driven method. It is also possible to use data-driven system model in conjunction with a physics-based fault model, or vice versa.

2.1.2 Short and Long term predictions

As it was mentioned in previous paragraph, the main objective of PHM is to increase the system performances by improving the system maintenance time. Such task is carried out by monitoring the actual health state of the system and to determine possible future deviations of its nominal operation. Usually, two fundamental situations make that the system is out of its nominal operations, the fault occurrence and degradation caused by fatigue due to constant usage or operation. The effect of fault occurrence can be addressed by firstly using fault diagnosis methods to detect, isolate and identify the fault. Then the fault effect can be mitigated by generate fault tolerant control system in order to guarantee the system operation. On the other hand, the degradation caused by continuous use is determined by computing the actual health state of the system and compare it with the Begin of Life (BoL) value. With this, it is possible to define what is the degradation level and its evolution. Once the actual degradation trend and its causes are known, it is possible to make progression and to predict its future evolution for both short and long term predictions. The use of short or long term predictions depends on the system dynamics, lifetime of the system or component and accuracy of the prediction ([131, 175]). Figure 2.5 shows the prediction of the possible trend that the performance of a system could have. The solid dark blue line represents the past evolution of the system behavior until present time t_a, and the brown area is the *Safety Zone (SZ)* or the nominal operational limit. According to different factors such as the inputs of the system, aging, or even external disturbances, the system behavior could be progressed until reach values outside of its nominal operation. In that sense, if such factors are known, the future trajectory of the system behavior can be predicted until reaching the SZ (segmented blue lines).

When the system behavior reaches or exceed the upper limit of the SZ at some time t_{f_i}, it is stated that the system has reached its *End of Life (EoL$_i$)*. Then, the *Remaining Useful Time (RUL$_i$)* until reach the

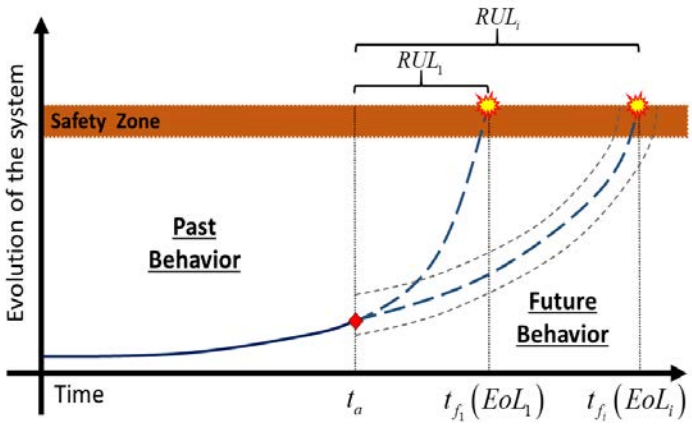

Figure 2.5: Evolution of the system behavior.

EoL_i is computed as

$$RUL_i = t_{f_i}(EoL_i) - t_a. \tag{2.1}$$

2.1.3 PHM in multirotor UAV

In addition, the PHM is useful to determine the actual and future evolutions of system performances considering short and long term predictions. However the predictions executed around the PHM approaches are not limited to evaluate only the system health. In UAV applications, the PHM have been used to improve the flight performance by developing health management systems which allows designers to examine optimal fault accommodation techniques that can increase availability, improve safety, and optimize maintenance resource planning for complex vehicle systems ([48, 60, 107, 208]). On the other hand, one emerging application for UAV PHM electrically powered is the prognosis of battery performance and prediction of flight endurance.

PHM of UAV power source

The application of PHM techniques to monitor the health and to evaluate the performances of power source in UAVs has enabled a better use of energy on-board. Usually Lithium batteries have been used for UAV electrically powered because they are able to provide high power and energy densities. The prediction of battery performance has been addressed considering model-based and data driven techniques. However, some efforts have been dedicated to evaluate the battery health without considering the final application as:

- Model-based:
  - Particle filter [3, 104, 110, 154, 177, 194, 195, 200]
  - Empirical aging model [12, 38, 71, 98, 99, 101]
  - Kalman filter [10, 70, 197]
  - Bayes model [30, 111, 121, 205]
  - Observers [61]
- Data-driven

- Neural networks [39, 103, 160, 203]
- Gaussian Process [100, 198]
- Wiener process [179]
- Support vector regression [102, 188, 191]
- Deep learning [82].

On the other hand, other works have made efforts to integrate PHM strategies into the UAV operations focused in the prediction of battery End of Discharge and flight endurance.

Flight endurance prediction

Nowadays, the use of Lithium Polymer (Li-Po) battery as powertrain for UAV multirotor with capabilities of vertical take-off and landing (VTOL) has become in a power source capable and economical, due to its high energy and power densities, discharge rate (C-rate), and zero emission of pollutants ([46]). By considering a new and fully charged battery, the flight endurance is between 10 to 30 minutes ([26, 114, 148]), where 85% of the energy is consumed by the propulsion system. The remaining consumption is caused by the sensors, (such as GPS, accelerometers, compass, gyroscope ([6])), the flight control computer, and for some payload (gimbals system, cameras, and other kind of sensors).

However, the flight endurance is gradually reduced over timer due to aging of the battery. The effect of aging is characterized by a capacity loss and immediately power fade. The aging is caused by several factors such as high-rate cycling, overdischarge and overcharge, and drastically changes of operation temperature ([193]). To avoid damages and reduce the aging rate during the charge/discharge cycles of the battery, it is necessary to monitor the State of Charge (SoC) and to establish safety limits around the End of Discharge (EoD) (also called *cut-off voltage*). At a given time, the SoC is the proportion of the available charge, compared to the total charge available when the battery is fully charged, it is analog to a car gas fuel gauge. On the other hand, the EoD indicates that the battery is fully discharged. In the literature of Electrical Cars, such concepts are the main criterion in the design of Battery Manage Systems (BMS) ([155]), where the main objective is to define adequate operation regimes to extend the life of the battery and maximize the energy supplied. In the case of UAVs, the monitoring of SoC battery during the development of a mission will allow to establish a voltage safety limit before reaching the EoD to ensure the fulfillment of the mission, safeguard the integrity of the battery, and have an adequate use of the energy supplied to maximize the flight endurance.

Several researches have addressed the problem of flight endurance for different types of UAV considering mainly three types of powertrain such as batteries, fuel cells, and solar cells ([109, 155, 178, 181]). The main objectives of such researches were the development of methodologies and strategies to improve and extend the flight endurance taking into account the geometry of the UAV, disturbance as the wind, the type of trajectory, the maximum altitude and the power requirement to perform a mission. In the specific case of UAV multirotor powered by Li-Po batteries, the efforts have been focused to generate strategies to ensure the fulfillment of a mission and increase flight time, e.g. ([42]) are presented an integrated planning and control approach to increase the probability of completion of fly-by missions by battery-powered UAV quadrotor. The authors in ([1]) proposed a technique to extend the endurance of battery-powered rotorcraft by sub-diving the monolithic battery into multiple smaller capacity batteries which are sequentially discharged and released. Also, in ([2]) the authors characterized the power consumption of multirotor and derived an endurance estimation model. ([114]) are presented two optimal control problems with respect to the angular accelerations of four electrical motors of an UAV quadrotor to improve its flight endurance. More recently ([44]) are presented experimental results of an analysis of the energy consumption and derivation and validation of empirical formulas to estimate the power consumption and

the remaining flight time. The works mentioned above were mainly engaged in developing strategies to improve the consumption of the energy supply, which allows the battery to extend the power consumption for UAV applications, to extend the flight endurance and to ensure the fulfillment of a mission.

2.2 Mission planning

The mission planning concept comprise all those items related to *operation modes* during a flight and how they enable to increase the flight efficient and to reduce the risk to humans ([168]). Such operation modes demand more versatility in the face of changing objectives and environment specifications, adaptability to uncertain events in the immediate and broader environments and good performances and robustness in changing operating conditions. In that sense, the main requirement is to have an autonomous vehicle able to execute a *task selection* and a *decision making* to perform a motion for a given objective and execute them. During the task selection, the UAV must make plans taking into account the available information about the course of the mission and consequently take decisions. *Decision making* determines the main most important requirements as the choice of the way-points and evaluates possible environment uncertainties. In sequential, decision making, the UAV seeks to choose the best actions based on its observations of the world. On the other hand, path planning deals with the trajectory algorithmic development based on the available information of the mission. Depending on mission requirements, it can contain slow or fast speed parts, short or long distance between way-points, and in special cases, the UAV should stay in a particular position for certain period of time.

Based on the previous definitions an autonomous UAV must be capable to performance mission without human intervention considering:

- Perceive its environment, consequently update its activity and response to changes in its own state,
- Control the actuators and keep as close as possible to the planned trajectory despite un-modeled dynamics, parametric uncertainties and sensor noise,
- Regulate its motion with respect to the local environment,
- Be able to avoid obstacles and other UAV and assess the information from the multi-sensor environment,
- Follow mission plans, account for changing weather and changes in its operating environments,
- Be able to assess its *current condition* and determine if that condition meets the requirements of the mission on course.

The implementation of previous requirements is made by considering a hierarchical structure of the UAV system, which also permits to reduce the complexity of large scale systems depending on if it is a single or multi-vehicle system:

- Single-vehicle (Figure 2.6). The lowest level is the reference trajectory tracking. The computer control (also called autopilot) uses as references the trajectory and path generated by the second level (from the bottom), while satisfying vehicle constraints and clearance. Such paths and trajectories have been calculated using the set of way-points or flight plan that has been determined depending on the assigned mission. The highest level is the mission planning, it determines the mission targets areas, probable obstacles and restricted areas of flight. This level uses decision making either deterministic or under uncertainty.

- Multi-vehicle (Figure 2.7), trajectory generation and tracking are still considered in the lowest level. While the highest level is still the mission planning, the fourth level (from bottom) is the multi-objective decision making level. The team must be able to plan its mission, to choose what goal it will address among those proposed, in what order and how it will perform its operations. The cooperation of the vehicle teams is on the third level while resource allocation and way-point selection have to be executed on the second level. The vehicles must be able to generate a new plan in response to events occurring during the mission that could invalidate the mission in progress.

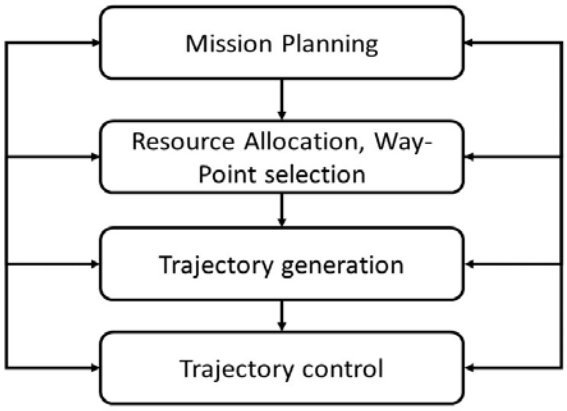

Figure 2.6: Single-vehicle mission planning hierarchy [168].

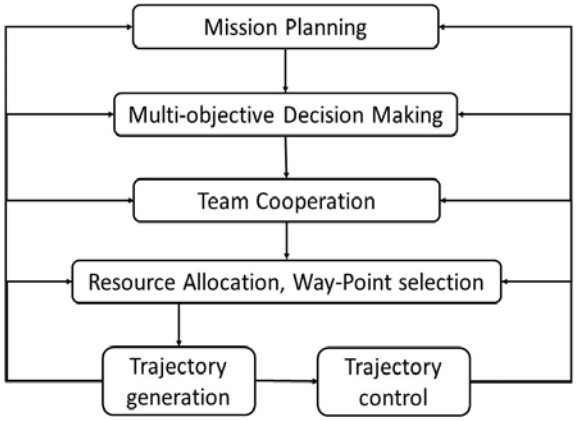

Figure 2.7: Multi-vehicles mission planning hierarchy [168].

Multiple objectives can be defined and reached considering single or multi vehicle hierarchy. They depend on the application and the mission complexity. This thesis focuses in mission planning for a single-vehicle taking into account the hierarchy structure in Figure 2.6 and its impact in UAV.

Different works have considered a hierarchy control structure for a single-UAV vehicle taking into from the possible structural design to the necessary software to carry out different types of missions autonomously. In ([182]) the authors presented an integrated/hierarchical approach to vehicle instrumentation, computing, modeling and control to enable an autonomy degree able to allow that the vehicle operate safely in unstructured environments within their flight envelope, to accommodate subsystems/component failure modes without major performance degradation or loss of vehicles and perform extreme maneuvers without

violating stability limits. Such hierarchical control structure for mission intelligent flow is presented in Figure 2.8 where the main routine to execute consist to determine if the mission can be fulfillment or not according to UAV state. Likewise the authors presented in Figure 2.9 the expected UAV autonomy capabilities according to the U.S. DoD's UAV autonomy roadmap ([147]).

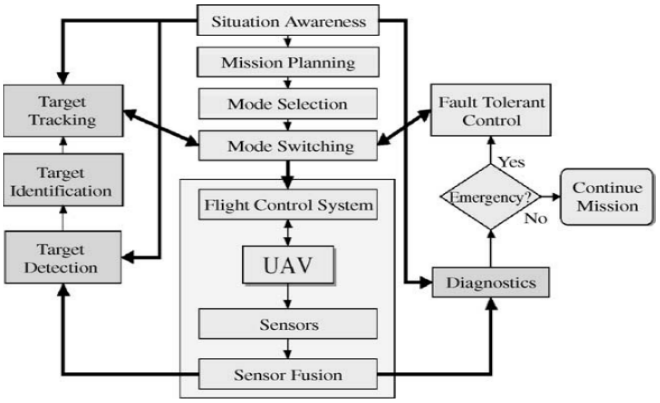

Figure 2.8: Mission intelligent flow [182].

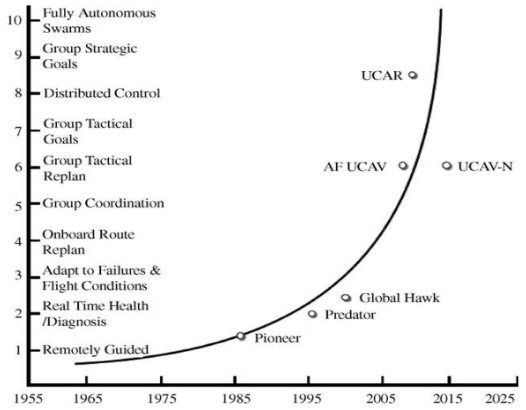

Figure 2.9: Autonomous control level trend [182].

In ([183]), the authors presented techniques to improve mission level functional reliability through better system self-awareness and adaptive mission planning in the context of multiple vehicle operations and autonomous multi-agent teams. The mission planning technique is based on the health management information (Figure 2.10). Each mission system component is used to improve the mission system's self-awareness and adapt vehicle, guidance, task and mission plans.

The schemes in Figures 2.9 and 2.10 consider the main components and routines necessaries to execute the corresponding task evolving the mission planning concept. Other works like ([50, 149, 176]) have added elements related to contingency management during the fault occurrence by penalty the health conditions of the system components. In addition, other problem addressed in the context of mission planning is the obstacle avoidance [14, 184] which requires to have an adequate understanding and knowledge of environment and equip the UAV with different sensor able to collect data for decision making. As it can be noted in the previous works, the mission planning encompass different routines and techniques to increase the autonomous capabilities to guarantee the surveillance of the UAV and reduce human risk.

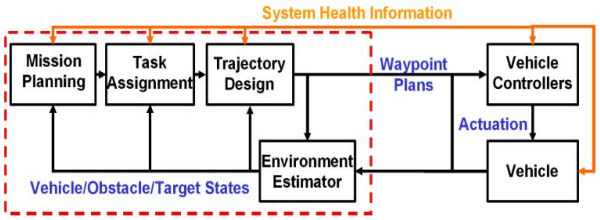

Figure 2.10: Health management-based hierarchical architecture model for multi-vehicle mission system [183].

2.3 Path planning

The multirotors are usually controlled remotely while some of them can fly autonomously based on pre-programmed flight paths. Missions currently undertaken by the UAV systems are predefined. In that sense, the UAV follows a *flight plan* initially developed as a commercial aircraft with a *Flight Management System*. The flight plan is a sequence of reference points or way points usually defined by latitude and longitude which describes the UAV position around 3D plane. The number of way-points and their location depends on the application and mission type. The way points are assumed to be joined by straight line segments, originating just after take-off phase and terminating at the landing phase.

According to [106], the main issues that a path planning algorithm for UAV multirotors must consider are: the autonomous navigation in three dimensions (3D) inside a cluttered or uncluttered environment, the obstacle avoidance, and the dynamical constraints of the UAV. In order to solve such issues, different path planning algorithms have been developed. In [17], a path planning algorithm for autonomous robotic exploration and inspection based on an on-line planning method in a receding horizon fashion by sampling possible future configuration in geometric random tree was introduced. The authors in [122] presented a method to path definition based on a Cascaded control architecture and using a nonlinear control technique for both control loops (position and attitude) taking into account obstacles perceived in real-time and avoids collisions. In [144], the authors focused on the analysis of different algorithms dedicated to path planning considering the flight time and the distance traveled from one point to another one and evaluating the autonomously avoiding obstacles. In [145], an algorithm for trajectory generation based on the differentially flat quadrotor model through complex real-world environments with an optimizing polynomial path segments was presented. As it can be noticed, in these works the path planning is developed with the consideration of the trajectory characteristics and the UAV dynamics constraints. However, they do not take into account the dependency between the energy consumed during the flight and the battery performance. In this work we are focused on path planning algorithms dedicated to minimize the energy consumption.

One way to consider the dependency between energy consumed during the flight and the battery performances is to determine the maximum flight endurance. According to [33], the flight endurance is mainly determinate by two power-related factors: the required power to sustain the desired flight profile and the battery discharge performances. The power required is associated to the total energy necessary to take-off, move between way-points and landing, i.e. the elements which define the trajectory, and the battery discharge performances which depend on the actual condition of the battery or State of Health (SoH) and determine the battery aging rate. The battery aging is mainly caused by two factors: the storage and the use (cyclic charge/discharge) ([22]). However, other factors contribute to increase the battery aging such as deep discharges, inadequate charging methods, and operating temperature variations. In that sense, it is necessary to quantify the battery aging by defining the SoH between flights in order to use this informa-

tion in a complete path planning strategy to guarantee the fulfillment of the mission and the UAV integrity.

Different solutions have been presented to overcome the problems associated with the path planning based on energy supplied. Such solutions have focused into generate strategies to optimize the energy consumption, and improve the efficiency of the flight performances considering two approaches: mechanics and analytics. The mechanics approaches are associated to geometric characteristics of the UAV, e.g. in ([139]) an experimental platform based on quadrotor was designed to maximize the thrust using an aero-elastic blade design was presented. In ([49]), the authors introduce a four-rotor configuration that merges the simplicity of a quadrotor with the energy efficiency of a helicopter, while improving maneuvering rotor bandwidth. The authors in ([185]) conceived a compound multirotor configuration specifically for flight through narrow corridors, and the design combines the contradictory requirements of limited width, high agility and long endurance while carrying a significant payload. On the other hand, the analytics approaches are dedicated to generate optimal path planning or flight profiles, e.g. in ([114]), a path planning method based on two optimal control with respect to the angular accelerations of the motor for a quadrotor is presented, and the solution was yielded in to find minimum energy and fixed-energy paths. In ([44]) was presented the results of an analysis of the energy consumption in various discrete movement states of a multirotor. A systematic relationship between the system and movement parameters and the energy consumption was established, and finally a generic energy consumption profile model was generated and validated. The authors in ([86]) investigated three prominent types of smooth trajectories (minimum acceleration, minimum jerk and minimum snap), and evaluate their energetic efficiency through the total energy consumption. The energy consumed by each trajectory type was determined via aerodynamics-based expressions for power consumption of rotorcraft. In ([25]), a flatness-based flight trajectory planning/re-planing strategy considering the occurrence of faults in actuators is presented, and the trajectory planning/re-planning problem is formulated as a constrained optimization problem. As it can be seen, different analytically solutions have been proposed to address the path planning problem along the energy consumption. However, these works do not take into account the influence of the battery performance and the variations of SoH in the path planning problem.

2.4 Conclusions

In this Chapter, the main elements forming the core of State of Art of this work as Prognosis, mission and path planning were presented as well as the more recently works. In addition, the introduction of energy dependency into mission and path planning problem are one of main interest to generate more safety and reliable autonomous vehicles as well as the increase of the flight capabilities. While some works have focused on addressing the problem from the point of view of the multirotor and its energy requirements due to the aerodynamics of the vehicle at the simulation level, others have presented results using a practical approach by conducting experimental tests and trying to characterize the main energy phenomena in the vehicle during flight. However, such studies show the effect of energy consumption at the beginning of the battery life without taking into account the phenomena of aging or the effect of discharge. In that sense, in this research it is proposed to integrate all the elements related to the mission and path planning together with the effects of aging that affect the performances of the battery. This will provide a unified framework for mission planning taking into account energy dependence. In the following chapters, the main elements integrating the methodology proposed will be developed. The next chapter is dedicated to the presentation of multirotor mathematical model and it propulsion system as well as the development of a control strategy taking into account the dynamics of battery discharge.

Chapter 3

Mathematical model of UAV hexarotor

In this Chapter, the nonlinear dynamics around the position and orientation of the multirotor UAV is described as well as the elements which integrating the propulsion system that are the Lithium Polymer (Li-Po) Battery and BrushLess DC Motors (BLDCMs). Firstly, the most common multirotor flight and design configuration will be presented in Section 3.1 following by the nonlinear mathematical model describing the dynamics around the multirotor, described in Section 3.2. Then the nonlinear mathematical model of the propulsion system is described in Section 3.3. Finally, a cascade control loop derived from linear hexarotor dynamics and based on PID (Proportional Integrative-Derivative) controllers both position and orientation is introduced in Section 3.4. In addition, the coupling between the Li-Po battery and BLDCMs is analyzed in this section as well as the effect of discharge rate into the controller performance.

3.1 Multirotor configurations

A multirotor is a particular helicopter lifted and propelled by two or more BLDCMs with vertical take off and landing capabilities ([58]). Usually, the multirotors are classified as rotorcraft, as opposed to fixed-wing aircraft, because their lift is generated by a set of revolving narrow-chord airfoils. Unlike most helicopters, multirotors generally have symmetrically pitched blades. Control of vehicle motion (position and orientation) is achieved by modifying the rotation rate and/or the axis of rotation direction of one or more BLDCMs, thereby changing its torque load and thrust/lift characteristics. According to number of BLDCMs it is possible to get different design configurations and flight modes, e.g. in Figure 3.1 two Trirotors flight configuration are shown where (a) all rotors are co-rotating or (b) one of the rotors (green one) counter-rotates.

Figure 3.1: Trirotor flight configurations ([58]).

Usually, multirotors with more than three rotors as quadrotor (Figure 3.2), hexarotor (Figure 3.3) and octorotors (Figure 3.4) can be controlled to fly either in + flight configuration, i.e. pointing an arm in the

navigation zone (according to x-y-z directions), or in **X** flight configuration where the navigation direction is in the middle plane between two arms. In addition, other less common design configurations are more suitable for heavier payload and major safety demanding flight mission such as V design in which the eight rotors are equally split on two divergent bars as it can be seen in Figure 3.4-(b). On the other hand, the **Y** and *X* design configurations where the multirotor is lifted by a configuration of coaxially coupled rotors can be generated for both hexarotor and octorotor vehicles as it can be seen in Figures 3.3-(b) and 3.4-(c) respectively.

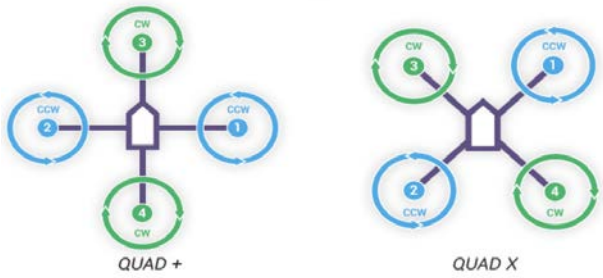

Figure 3.2: Quadrotor + and **X** flight configurations ([58]) .

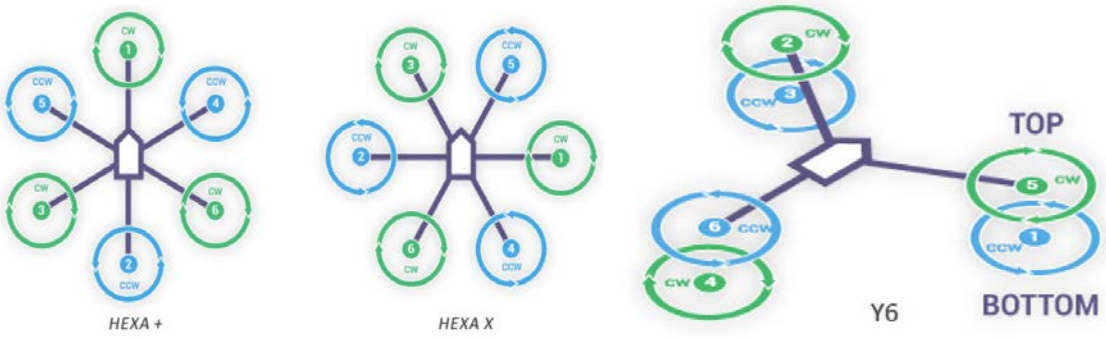

(a) (b)

Figure 3.3: (a) Hexarotor + and X flight configuration. (b) Hexarotor coaxial-rotor design configuration ([58]).

In this work, the considered multirotor configuration is the hexarotor **X** due to redundancy of BLDCM contained to generate the enough thrust force to lift the vehicle during the flight. However the results obtained in the development of mission planning and re-planning as well as the generation of minimum energy paths can be easily extended to the others configuration. In the next sections, the nonlinear model around hexarotor dynamics as well as the elements integrating the propulsion system will be developed.

3.2 Hexarotor dynamics

The considered multirotor is composed by six BrushLess DC Motors (BLDCMs) attached to a rigid and symmetrical six-arm frame as it can be seen in Figure 3.5. In turn, each BLDCM has a rigid propeller connected to its rotor and generates a positive thrust f_i and torques τ_i, $i = 1, \cdots, 6$, proportionally to the square angular speed of the propeller. The sum of the individuals forces produces the total thrust T_{thr} to lift, and the difference generates the torques acting on the hexarotor. Moreover, the BLDCMs 1, 3, and 5 rotate in clockwise whiles BLDCMs 2, 4, and 6 rotate in counterclockwise given the so-called **X**

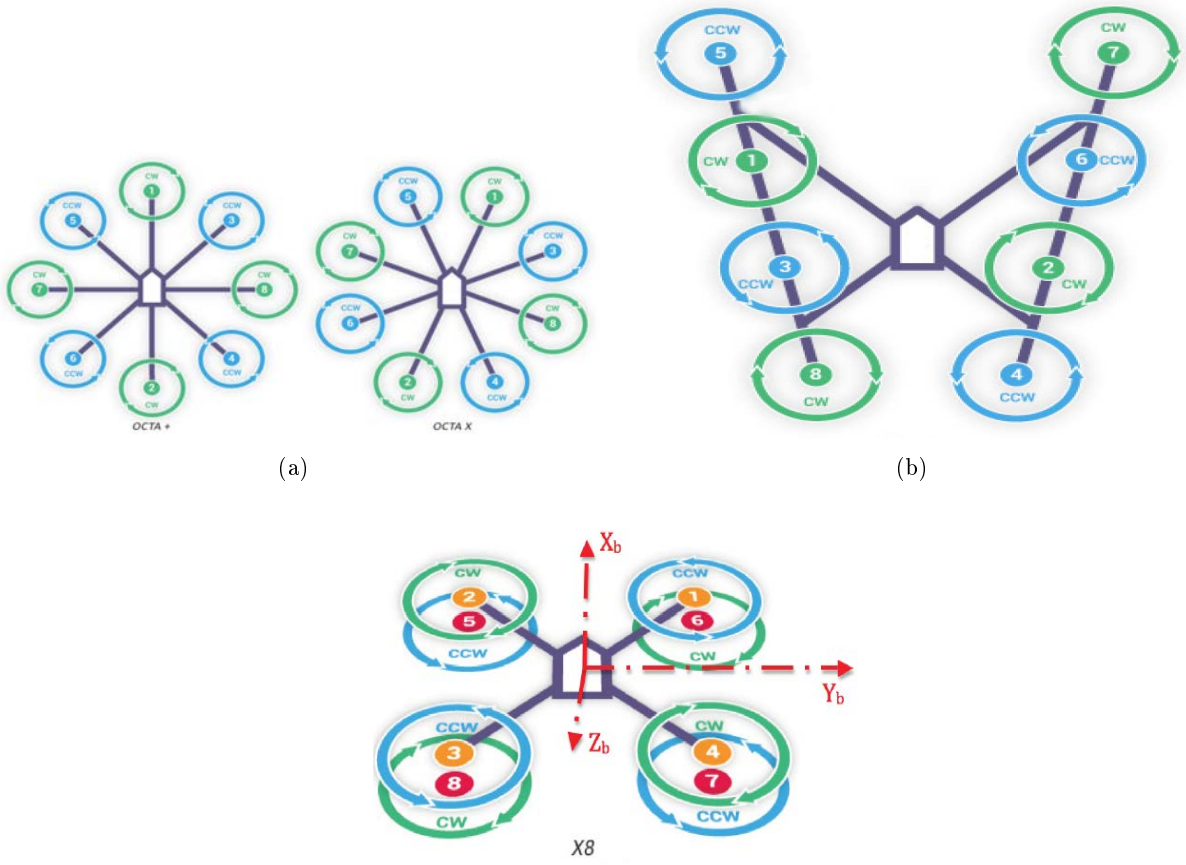

(a) (b)

(c)

Figure 3.4: (a) Octorotor + and **X** flight configuration. (b) Octorotor V design configuration. (c) Octorotor X flight and coaxial-rotor design configuration ([58]).

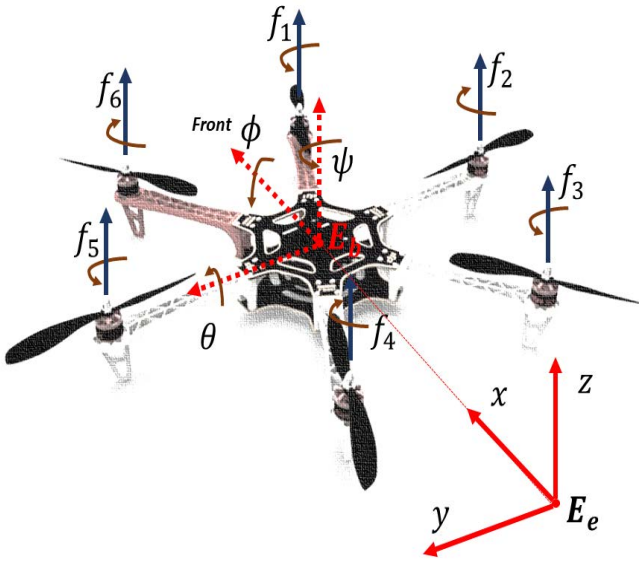

Figure 3.5: Reference frames of the UAV hexarotor.

configuration. Such configuration allows to cancel gyroscopic effects and aerodynamic torques. In addition, it is important to remark that the hexarotor is considered an over-actuated system, i.e. the amount of actuators is greater than control inputs.

The movement of the hexarotor is performed around two reference frames: the fixed inertial frame, denoted by E_e (hexarotor position), and the non-inertial frame or rigid body frame, denoted by E_b (hexarotor orientation), and assuming that the non-inertial frame coincides with the center of gravity of the hexarotor. By adopting the Euler angles parametrization, the orientation of the hexarotor in the space is given by the rotation from E_b to E_e by the rotation matrix $\mathbf{R}(\phi, \theta, \psi) \in S0(3)$ defined as:

$$\mathbf{R} = \begin{bmatrix} \mathbf{c}\psi\mathbf{c}\theta & \mathbf{c}\psi\mathbf{s}\theta\mathbf{s}\phi - \mathbf{s}\psi\mathbf{c}\phi & \mathbf{c}\psi\mathbf{s}\theta\mathbf{c}\phi + \mathbf{s}\psi\mathbf{s}\phi \\ \mathbf{s}\psi\mathbf{c}\theta & \mathbf{s}\psi\mathbf{s}\theta\mathbf{s}\phi + \mathbf{c}\psi\mathbf{c}\phi & \mathbf{s}\psi\mathbf{s}\theta\mathbf{c}\phi - \mathbf{c}\psi\mathbf{c}\phi \\ -\mathbf{s}\theta & \mathbf{c}\theta\mathbf{c}\phi & \mathbf{c}\theta\mathbf{c}\phi \end{bmatrix}, \tag{3.1}$$

where $\mathbf{c}$ and $\mathbf{s}$ are the trigonometric functions cos and sin respectively. By considering the Newton-Euler formalism, the dynamic of the hexarotor considered as a rigid body under external forces applied to the center of mass expressed on the non-inertial frame is expressed as ([24, 128]):

$$\begin{aligned} \dot{\xi} &= v \\ m\dot{v} &= f \\ \dot{R} &= R\hat{\bar{\omega}} \\ I\hat{\bar{\omega}} &= -\bar{\omega} \times I\bar{\omega} + \tau, \end{aligned} \tag{3.2}$$

where $\xi = [x\ y\ z]^{\mathrm{T}} \in \mathbb{R}^3$ is the position of the hexarotor with respect to the inertial frame E_e relative to a fixed origin, $v \in E_e$ is the linear velocity expressed in the inertial frame, $\bar{\omega} \in E_b$ is the angular velocity of the hexarotor expressed in the body frame E_b, m is the total mass, $I \in \mathbb{R}^{3\times3}$ denotes the constant inertia matrix around the center of mass, $\hat{\bar{\omega}}$ is the skew-symmetric matrix of the vector $\bar{\omega}$. $f \in E_e$ is the vector of the principal non-conservative forces and includes the thrust T_{thr} and drag terms associated with the BLDCMs. $\tau \in E_b$ is derived from differential thrust associated with pairs of BLDCMs along with aerodynamics effects and gyroscopic effects.

Translational and gravitational forces. The forces acting on the hexarotor are given by the translational force T_{thr} and the gravitational force g. The translational force is defined as:

$$T_{thr} = \sum_{i=1}^{6} f_i, \tag{3.3}$$

where the thrust f_i produced by the ith-BLDCM in free air is modeled as $f_i = b\omega_i^2$ in the z-direction, where $b > 0$ is a constant associated to propeller geometry and ω_i is the angular speed of the ith-BLDCM. In that sense, (3.3) is rewritten as :

$$T_{thr} = b\left(\sum_{i=1}^{6} \omega_i^2\right), \tag{3.4}$$

and the gravitational force applied to the hexarotor is:

$$f_g = -mgE(3), \tag{3.5}$$

where $E(3) = [0\,0\,1]^{\mathrm{T}}$ is an unitary vector in E_e. Finally, the force applied to hexarotor is defined as:

$$F = R_{E(3)} T_{thr} + f_g, \tag{3.6}$$

where $R_{E(3)} = \mathbf{R}E(3)$, with $\mathbf{R}$ as the rotation matrix (3.1).

Torques. The torque generated by each BLDCM is denoted by τ_{BLDCMi}, moreover the torque of the BLDCM is opposed by an aerodynamic drag $\tau_d = d\omega_i^2$, where $d > 0$ is a constant associated for the quasi-stationary maneuvers (near hover) in free flight. In a steady stable condition, i.e. $\dot{\omega_i} = 0$ it it is assumed that $\tau_{BLDCMi} = \tau_d$ and the generalized torques considering the hexarotor geometry are defined as:

$$\tau\left(E_b\right) = \begin{bmatrix} \frac{bl}{2}\left(-\omega_1^2 - 2\omega_2^2 - \omega_3^2 + \omega_4^2 + 2\omega_5^2 + \omega_6^2\right) \\ \frac{bl\sqrt{3}}{2}\left(-\omega_1^2 + \omega_3^2 + \omega_4^2 - \omega_6^2\right) \\ d\left(-\omega_1^2 + \omega_2^2 - \omega_3^2 + \omega_4^2 - \omega_5^2 + \omega_6^2\right) \end{bmatrix}, \tag{3.7}$$

where $\tau\left(E_b\right) = [\tau_\phi\, \tau_\theta\, \tau_\psi]^{\mathrm{T}}$ are the generalized torques around roll, pitch and yaw movements, l is the distance from each BLDCM to the center of mass of the hexarotor, and $c = \sqrt{3}$ is a constant associated with hexarotor geometry. It is also assumed that each rotor can be considered as a rigid disc rotating around the z-axis in the body frame with angular speed ω_i, and furthermore the rotary shaft of the rotor is considered itself moving with the angular speed of the frame, which leads to gyroscopic torques (also called gyroscopic effect [20]) applied to the hexarotor:

$$\tau_{G_b} = -\left(\bar{\omega} \times E(3)\right) \sum_{i=1}^{6} J_m \omega_i, \tag{3.8}$$

where J_m is the inertial of the rotor. Finally the differential thrust associated with the torques is expressed as:

$$\tau = \tau\left(E_b\right) + \tau_{G_b}. \tag{3.9}$$

By considering equations (3.6) and (3.9), system (3.2) is rewriting as

$$\begin{aligned} \dot{\xi} &= v \\ m\dot{v} &= R_{E(3)} T_{thr} - mgE(3) \\ \dot{R} &= R\hat{\bar{\omega}} \\ I\hat{\bar{\omega}} &= -\bar{\omega} \times I\bar{\omega} + \tau\left(E_b\right) + \tau_{G_b}. \end{aligned} \tag{3.10}$$

In order to express the final representation of the model describing the dynamics of hexarotor movement in the inertial and rigid body reference frames, the system (3.2) is separated into position dynamics (denoted as ξ) and orientation dynamics (denoted as η). In that sense, the system (3.2) with respect to ξ is defined as

$$\ddot{\xi} = \frac{1}{m}\left(\mathbf{R}E(3)T_{thr} - mgE(3)\right) \tag{3.11}$$

where

$$\mathbf{R}E(3) = \begin{bmatrix} \mathbf{s}\phi\mathbf{s}\psi + \mathbf{c}\phi\mathbf{c}\psi\mathbf{s}\theta \\ \mathbf{c}\phi\mathbf{s}\psi\mathbf{s}\theta - \mathbf{c}\psi\mathbf{s}\phi \\ \mathbf{c}\theta\mathbf{c}\phi \end{bmatrix} \tag{3.12}$$

and defining $U_1 = T_{thr}$ the following equation system describing the hexarotor position around $x - y - z$ axis is obtained:

$$\begin{aligned} \ddot{x} &= (\mathbf{c}\phi\mathbf{s}\theta\mathbf{c}\psi + \mathbf{s}\phi\mathbf{s}\psi)\frac{U_1}{m} \\ \ddot{y} &= (\mathbf{c}\phi\mathbf{s}\theta\mathbf{s}\psi - \mathbf{s}\phi\mathbf{c}\psi)\frac{U_1}{m} \\ \ddot{z} &= -g + (\mathbf{c}\phi\mathbf{c}\theta)\frac{U_1}{m}. \end{aligned} \tag{3.13}$$

Likewise, the system equation describing the hexarotor orientation around Euler angles is obtained by considering that the angular velocity of the hexarotor expressed in the body frame describes the orientation dynamics, i.e. $\bar{\omega} \approx \dot{\eta}$ and the torques around body frame are represented as $\tau_\phi = U_2$, $\tau_\theta = U_3$, and $\tau_\psi = U_4$ as follows

$$\begin{aligned} \ddot{\phi} &= \frac{I_y - I_z}{I_x}\dot{\theta}\dot{\psi} + \frac{J_m}{I_x}\omega_G\dot{\theta} + \frac{U_2}{I_x} \\ \ddot{\theta} &= \frac{I_z - I_x}{I_y}\dot{\phi}\dot{\psi} - \frac{J_m}{I_y}\omega_G\dot{\phi} + \frac{U_3}{I_y} \\ \ddot{\psi} &= \frac{I_x - I_y}{I_z}\dot{\theta}\dot{\phi} + \frac{U_4}{I_z}, \end{aligned} \tag{3.14}$$

where I_x, I_y and I_z are the body inertial constants, respectively and ω_G is the gyroscopic effect. According to equations (3.6) and (3.9), the inputs of the system are defined as:

$$\begin{aligned} U_1 &= b\left(\omega_1^2 + \omega_2^2 + \omega_3^2 + \omega_4^2 + \omega_5^2 + \omega_6^2\right) \\ U_2 &= \frac{bl}{2}\left(-\omega_1^2 - 2\omega_2^2 - \omega_3^2 + \omega_4^2 + 2\omega_5^2 + \omega_6^2\right) \\ U_3 &= \frac{bl\sqrt{3}}{2}\left(-\omega_1^2 + \omega_3^2 + \omega_4^2 - \omega_6^2\right) \\ U_4 &= d\left(-\omega_1^2 + \omega_2^2 - \omega_3^2 + \omega_4^2 - \omega_5^2 + \omega_6^2\right) \\ \omega_G &= -\omega_1 + \omega_2 - \omega_3 + \omega_4 - \omega_5 + \omega_6^2 \end{aligned} \tag{3.15}$$

Finally, by grouping of (3.13) and (3.14) the following nonlinear set equations is established:

$$\begin{aligned} \ddot{x} &= (\mathbf{c}\phi\mathbf{s}\theta\mathbf{c}\psi + \mathbf{s}\phi\mathbf{s}\psi)\frac{U_1}{m} \\ \ddot{y} &= (\mathbf{c}\phi\mathbf{s}\theta\mathbf{s}\psi - \mathbf{s}\phi\mathbf{c}\psi)\frac{U_1}{m} \\ \ddot{z} &= -g + (\mathbf{c}\phi\mathbf{c}\theta)\frac{U_1}{m} \\ \ddot{\phi} &= \frac{I_y - I_z}{I_x}\dot{\theta}\dot{\psi} + \frac{J_m}{I_x}\omega_T\dot{\theta} + \frac{U_2}{I_x} \\ \ddot{\theta} &= \frac{I_z - I_x}{I_y}\dot{\phi}\dot{\psi} - \frac{J_m}{I_y}\omega_T\dot{\phi} + \frac{U_3}{I_y} \\ \ddot{\psi} &= \frac{I_x - I_y}{I_z}\dot{\theta}\dot{\phi} + \frac{U_4}{I_z}, \end{aligned} \tag{3.16}$$

In addition, the nonlinear system (3.16) can be written in a state space form $\dot{X} = f(X,U)$ as

$$\dot{X} = f(X,U) = \begin{bmatrix} x_2 \\ (\mathbf{c}x_7\mathbf{s}x_9\mathbf{c}x_{11} + \mathbf{s}x_7\mathbf{s}x_{11})\frac{U_1}{m} \\ x_4 \\ (\mathbf{c}x_7\mathbf{s}x_9\mathbf{s}x_{11} - \mathbf{s}x_7\mathbf{c}x_{11})\frac{U_1}{m} \\ x_6 \\ -g + (\mathbf{c}x_7\mathbf{c}x_9)\frac{U_1}{m} \\ x_8 \\ \frac{I_y - I_z}{I_x}\dot{x}_{10}\dot{x}_{12} + \frac{J_m}{I_x}\omega_G\dot{x}_{10} + \frac{U_2}{I_x} \\ x_{10} \\ \frac{I_z - I_x}{I_y}\dot{x}_8\dot{x}_{12} - \frac{J_m}{I_y}\omega_G\dot{x}_8 + \frac{U_3}{I_y} \\ x_{12} \\ \frac{I_x - I_y}{I_z}\dot{x}_8\dot{x}_{10} + \frac{U_4}{I_z} \end{bmatrix}, \tag{3.17}$$

where $X = \left[x\,\dot{x}\,y\,\dot{y}\,z\,\dot{z}\,\phi\,\dot{\phi}\,\theta\,\dot{\theta}\,\psi\,\dot{\psi}\right]^{\mathrm{T}} = [x_1\,x_2\,x_3\,x_4\,x_5\,x_6\,x_7\,x_8\,x_9\,x_{10}\,x_{11}\,x_{12}]^{\mathrm{T}}$ is the state vector, and $U = [U_1\,U_2\,U_3\,U_4]^{\mathrm{T}}$ is the input vector.

Linear representation. According to [25], even though the hexarotor model (3.16) with the inputs (3.15) is a simple and deterministic representation of the real system behavior, it remains a relatively complex model to deal with. Nevertheless, several simplified models can be derived to design a controller able to stabilize the orientation dynamics and control the position dynamics by tracking a reference position around x-y-z axis. In that sense, a linear model will be derived from nonlinear dynamics in order to generate the cascade control loop for both position and orientation hexarotor. The following assumptions are considered over nonlinear hexarotor model (3.16) ([58]):

- The variation around roll (ϕ) and pitch (θ) angles are considered very small and yaw (ψ) angle is keeping constant i.e. $\phi = 0$.
- The drag coefficient d is negligible by establishing low rotational speed.
- The dynamics around x-y is decoupled from z dynamics by considering hovering conditions i.e. $U_1 = g$.

Remark. The assumptions considered in the linear representation of nonlinear hexarotor dynamics allows to derived a model able to characterize the movement around internal and non inertial frame considering no-aggressive movements or big changes in hexarotor orientation. i.e. the Euler angles are limited to $\pm\frac{\pi}{2}$ for roll and pitch angles and $\pm\pi$. In addition, the linear model will be used to derive the control loop associated to hexarotor position and orientation using the classic control technique as the PID controller. The development of a PID controller requires a tunning process to adjust the controller gains. In that sense, a linear model is usually useful to carry out the tunning process according to control objectives.

Then, by taking into account the previous considerations the following linear model describing the position and orientation dynamics in hovering condition is obtained:

$$\begin{array}{ll} \ddot{x} = g\theta & \ddot{\phi} = \frac{U_2}{I_x} \\ \ddot{y} = -g\phi & \ddot{\theta} = \frac{U_3}{I_y} \\ \ddot{z} = -g + \frac{U_1}{m} & \ddot{\psi} = \frac{U_4}{I_z}, \end{array} \tag{3.18}$$

As it can be noted, the relationship between the position around x-y and orientation around $\phi - \theta$ Euler angles is established in this linear representation. This characteristic will be used in the design of cascade control loop developed in Section 3.4. In addition, the equation system (3.18) can be rewrite in state space for $\dot{\bar{X}} = A\bar{X} + BU$ as

$$\dot{\bar{X}} = A\bar{X} + BU \quad = \quad \begin{bmatrix} x_2 \\ gx_9 \\ x_4 \\ -gx_7 \\ x_6 \\ -g + \frac{U_1}{m} \\ x_8 \\ \frac{U_2}{I_x} \\ x_{10} \\ \frac{U_3}{I_y} \\ x_{12} \\ \frac{U_4}{I_z} \end{bmatrix}, \tag{3.19}$$

where $\bar{X} = \left[x\,\dot{x}\,y\,\dot{y}\,z\,\dot{z}\,\phi\,\dot{\phi}\,\theta\,\dot{\theta}\,\psi\,\dot{\psi}\right]^{\mathrm{T}} = [x_1\,x_2\,x_3\,x_4\,x_5\,x_6\,x_7\,x_8\,x_9\,x_{10}\,x_{11}\,x_{12}]^{\mathrm{T}}$ is the state vector, and $U = [U_1\,U_2\,U_3\,U_4]^{\mathrm{T}}$ is the input vector.

Remark. As it can be note from (3.18) the linear model leads to the development of a linear controller around hovering conditions. Usually, the procedure to follow for controller development is to design it using the line model and then validate its performance with the non-linear model. This methodology although it allows to generate a controller using linear control techniques could result in the generation of modeling uncertainties because the controller does not take into account the non-linearity present in the model. In Section (3.4) the design of control loop associated to position and orientation controller will be described taking into account the linear model representation of hexarotor dynamics.

3.3 Propulsion system

The propulsion system of any UAV multirotor with vertical take off and landing capabilities is composed by a set of BrushLess DC Motors (BLDCM) with a propeller attached to its shaft. The BLDCMs are powered by a Lithium Polymer battery through an Electronic Speed Control (ESC) as it can be seen in Figure 3.6.

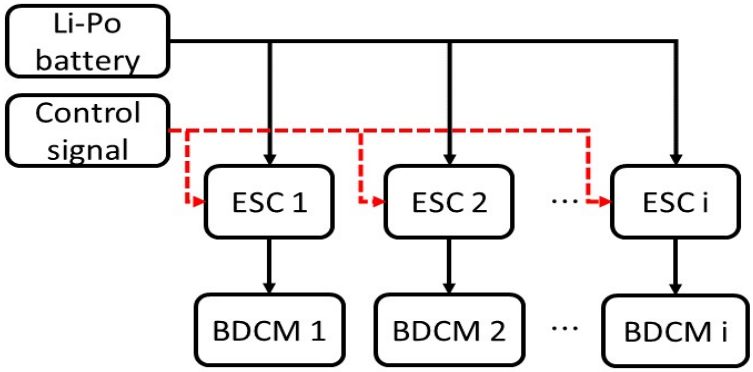

Figure 3.6: Propulsion system of multirotor.

In Figure 3.7 the connection Li-Po battery - ESC - BLDCM is detailed for one motor. The ESC adjusts the angular speed of the BLDCM through a Pulse-With Modulation (PWM) signal. In this study the dynamic around the ESC is neglected and it is assumed that the voltage supply by the battery and the generated current by the motors are averaged with respect to the duty cycle value produced by the control signal.

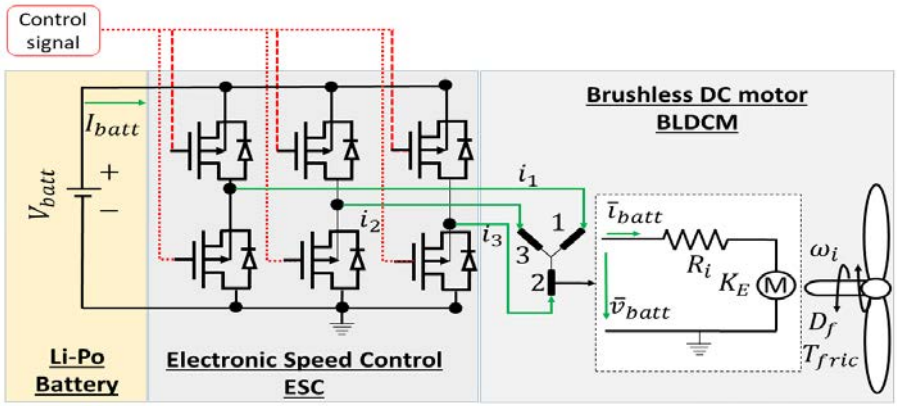

Figure 3.7: Connexion of Li-Po battery - ESC - BLDCM.

3.3.1 Lithium Polymer battery dynamics

Lithium Polymer (Li-Po) batteries are devices converting the energy released by spontaneous chemical reaction to electricity work. Due to their rechargeable capability they belong to the Secondary Lithium batteries family and possess properties such as high discharge rate (C-rate), high energy and power densities. The Lithium Polymer (Li-Po) battery is made of several individual cells connected to each other in series (to have a high voltage value) or parallel (to have a high capacity in Ah) ([80]). In Figure 3.8 a

typical Li-Po battery used in aeromodelling applications ([35]) with four cells in series, a capacity of 6300 mAh, C-rate of 35C and operational voltage of 2.7 V to 4.2 V per cell.

Figure 3.8: Typically Li-Po battery used in multirotor UAV applications.

Electrical dynamics

The battery model describes the mathematical relationship and evolution of voltage and State of Charge (SoC), which is the proportion of the charge available at a given time compared to the total charge available when the battery is fully charged. The range of the SoC is $SoC \in \left[\begin{array}{cc} 0 & 1 \end{array}\right]$, where 1 corresponds to 100 % of the charge, i.e. the battery is fully charged, and 0 indicates that the battery is fully discharge, i.e. the End of Discharge (EoD) or cut-off voltage value has been reached. In lithium battery literature, there are different methods or techniques to determines the battery SoC. The so-called *Ampere Hour Counting* or *Coulomb Counting* ([61, 120]), which just takes into account the evolution of demanded current and its relationship with the nominal battery capacity:

$$SoC = SoC_{t_0} - \frac{1}{3600 \cdot C_T} \int_{t_o}^{t} I_{batt} dt, \tag{3.20}$$

where t_o represents the initial time, C_T is the total capacity of the battery expressed in (Ah). Other methods are based on the development of a state estimator like Luenberger observers ([16, 75]), Kalman Filters ([69, 136]) and sliding mode observers ([29, 83]). In Chapter 4, the development of SoC estimation will be developed as well as the proposed method.

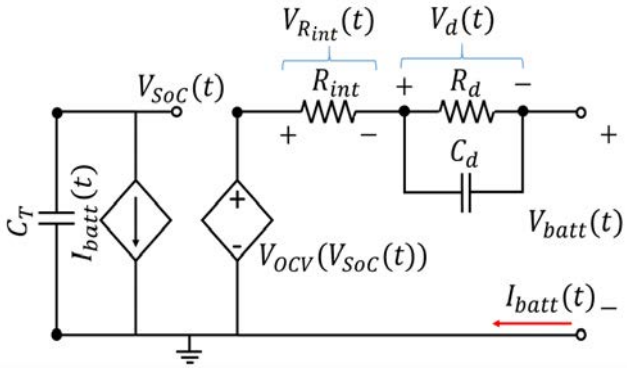

Figure 3.9: Electrical equivalent circuit of Li-Po battery.

The mathematical model of the Li-Po battery is based on an Equivalent Circuit Representation (ECR) according to Figure 3.9 ([28]). In Figure 3.9, (on the left-side of the circuit), the voltage $V_{SoC}(t)$ models the state of charge $SoC(t)$ of the battery from the capacity C_T. The voltage $V_{OCV}(V_{SoC})$ is the Open Circuit Voltage (OCV), i.e. it is the effective voltage in the battery terminals, and it is modeled as a function of the state of charge of the battery. The voltage $V_{R_{int}}(t)$ characterizes the ohmic over-potential due to the internal resistance of the battery R_{int}. $V_d(t)$ represents the transitory response of the voltage when a current is demanding to the battery. It is characterized by a first order response and its time constant depends on the value of parameters R_d and C_d. The mathematical model of the battery is given by:

$$\begin{aligned} \dot{V}_{SoC} &= -\frac{I_{batt}}{3600 \cdot C_T} \\ \dot{V}_d &= -\frac{V_d}{R_d \cdot C_d} + \frac{I_{batt}}{C_d} \\ V_{Batt} &= V_{OCV}(V_{SoC}) - V_d - R_{int}\, I_{batt}, \end{aligned} \tag{3.21}$$

where, the $V_{OCV}(V_{SoC})$ is experimentally defined as:

$$V_{OCV}(V_{SoC}) = \sum_{i=0}^{n} \lambda_i V_{SoC}^i + \ln(V_{SoC}) V_{SoC}. \tag{3.22}$$

n determines the order of the polynomial, and λ_i are the polynomial coefficients. It can be noted that the nonlinear function (3.22) is not unique and its formulation is obtained through experimental tests. In Appendix A, the characterization of Li-Po battery through experimental data is developed.

Thermal dynamics

The temperature of the battery is modeled by the Newton's law of cooling ([19]), and it is assumed that the heat is generated and distributed uniformly in the battery:

$$\begin{aligned} Q_b &= R_{int} \cdot I_{batt}^2, \\ \dot{T}_{batt} &= \frac{hA}{c}(T_{air} - T_{batt}) + \frac{Q_b}{c}, \end{aligned} \tag{3.23}$$

where T_{batt} is the battery temperature, h is the heat transfer coefficient, A is the surface area of the battery, c is the heat capacity of the battery, T_{air} is the temperature of the cooling air, and Q_{batt} is the heat generated in the battery.

3.3.2 BrushLess DC Motor dynamics

The BrushLess DC motor is a type of permanent magnet synchronous motor. It is drive by a DC voltage source and a current commutation achieved by solid-state switches. The main advantages that render this type of motor suitable for aerial robotic applications are a long operating life, high dynamic response, better speed and torque characteristics and higher torque-weight ratio ([52]). The mathematical model that describes the dynamics of the angular speed is divided into the electrical and the mechanical sub-models described by the following equations ([117]):

$$\begin{aligned} \bar{v}_{batt_i} &= R\bar{i}_{batt_i} + K_E \omega_i, \\ \dot{\omega}_i &= \frac{1}{J_m}(K_E \bar{i}_{batt_i} - d\omega^2 - D_f \omega_i - T_{fric}), \end{aligned} \tag{3.24}$$

where $R = \frac{2}{3}(\sum_{j=1}^{3} R_j)$ is the equivalent electric resistance of each coil, K_E is the back electromotive force, $\omega_i(t)$ is the angular velocity of the ith BLDCM, T_{fric} is the friction torque, D_f is the viscous damping coefficient, d is the drag constant, associated to the geometry of the propeller, and J_m is the inertia of the BLDCM. The average voltage $\bar{v}_{batt_i}(t)$ and current $\bar{i}_{batt_i}(t)$ are the voltage and current generated by the ESC and they are computed as follows:

$$\begin{aligned} \bar{v}_{batt_i} &= V_{batt} \cdot Dc_i \\ I_{BLDCM_i} &= \bar{i}_{batt_i} \cdot Dc_i, \end{aligned} \tag{3.25}$$

where V_{batt} is the battery voltage, I_{BLDCM_i} is the current generated by the ith BLDCM and $I_{batt} = \sum_{i=1}^{6} I_{BLDCM_i}$. Dc_i is the duty cycle of Pulse-Width Modulation (PWM) signal, which corresponds to control signal of the BLDCM speed. $Dc_i \in [0\,1]$ is defined as function of the reference angular speed of the ith-BLDCM and it is determined through experimental correlations, such as:

$$Dc_i = f(\omega^2_{ref_i}). \tag{3.26}$$

where ω_{ref_i} is the reference angular speed of the ith BLDCM.

In Figure 3.10 the interaction between the propulsion system and hexarotor dynamics is presented. As it can be noted, the dynamic of battery discharge affects directly the angular speed generated by each BLDCM according to mathematical relationship between duty cycle (3.26) and battery voltage (3.25). In addition the control loop must adjust the duty cycle in order to generate the angular speed of each BLDCM to keep the lift of hexarotor. In the following section, such considerations will be explained in the design of control loop for both hexarotor position and orientation.

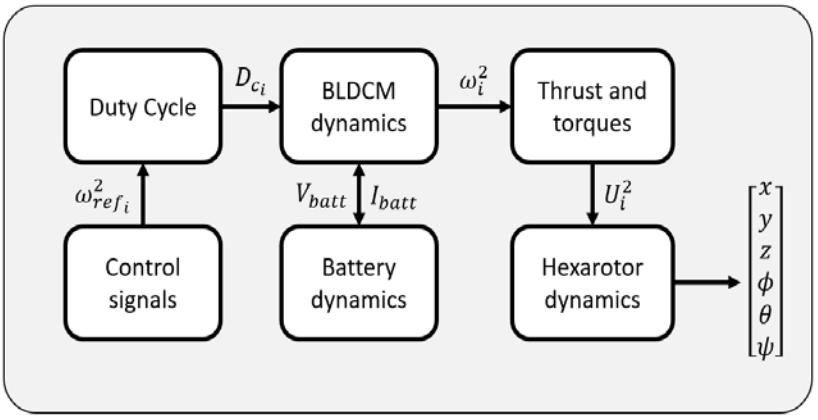

Figure 3.10: Interaction between propulsion system and hexarotor dynamics.

3.4 Position and orientation controller design

In order to keep the orientation of the vehicle stable during the flight and at the same time to follow a reference trajectory around x-y-z axis describing the fixed inertial frame, several control strategies have been developed using different methods and techniques which are based on the mathematical model of the vehicle. Generally such control techniques can be classified in two types: linear ([93, 112, 174]) and nonlinear ([67, 95, 96, 129]) controllers.

According to [174], multirotors are multivariable highly coupled nonlinear systems. The use of linear control for this system consists of an algebraic manipulation for state variables of linear model under certain environmental conditions. For trajectory tracking, the linear control can be applied only if the trajectory and the flying conditions for the quadrotor are not complex and difficult. In such cases, the coupled nature of the system requires high variations in the angular velocities and fast variations in the altitude, which cannot be realized by such controllers. For such linear controller techniques, the most common are the Proportional Integral Derivative (PID) controller ([5, 11, 91, 118, 142]), the Linear Quadratic Regulator (LQR) ([8, 66, 79, 87, 88, 171]) and H-Infinity controller ([7, 126, 143]).

On the other hand, the nonlinear controller are based on nonlinear mathematical representation of multirotor vehicle. They are able to manage the stabilization problem taking into account the nonlinear coupling of orientation dynamics around Euler angles, and the trajectory tracking considering complex flying conditions as well as obstacle avoidance. Among nonlinear controller techniques applied to multirotor the following are the most common: Sliding Mode Control, Backstepping Control ([32, 92, 146]), Feedback Linearization ([18, 92, 186]), Neural Network and Fuzzy Logic ([81, 157, 189]), Model Based Predictive Control (MBPC) ([85, 135, 140]), Adaptive Control ([76, 115, 123]) and Robust Control Algorithms ([4, 15, 90]).

In the next section, the development of a Cascade Control Loop (CCL) for both stabilization of hexarotor orientation and tracking of a reference position based on a classical PID controller strategy will be explained. In addition, the effect of the battery discharge will be analyzed considering the impact on the control signals and the angular speed of BLDCM by adding the dynamics of propulsion system.

3.4.1 Cascade Control Loop (CCL) development

Since the objective of this work is not to develop an advanced control law, the trajectory tracking controller is based on a position and orientation classical Cascade Control Loop (CCL) as it can be seen in Figure 3.11. The implementation of this control loop is developed by split the hexarotor dynamics described by (3.17) into translational and rotational dynamics. The rotational dynamics describes the orientation of the vehicle from Euler angles $[\phi\,\theta\,\psi]^{\mathbb{T}}$ and the translational dynamics represents the position around the $x-y-z$ axis of fixed inertial frame and it also depends on the Euler angles variation. As it can be not from Figure 3.11 on left side, the position and orientation controllers generates the reference control signals (thrust force and torques) denoted by $\bar{U}_i$. In addition, the position controller also generates the roll (ϕ_r) and pitch (θ_r) reference angles (inputs of the orientation controller) by considering that a variation on roll and pitch angles generate a movement around and y and x position respectively. On the other hand, the yaw (ψ) reference angle is generated externally. The reference control signals are distributed around of BLDCMs and the angular speed generated by them produce the control inputs denoted by U_i. The coupling between the propulsion system and the reference control signals will be explained in Subsection 3.4.2.

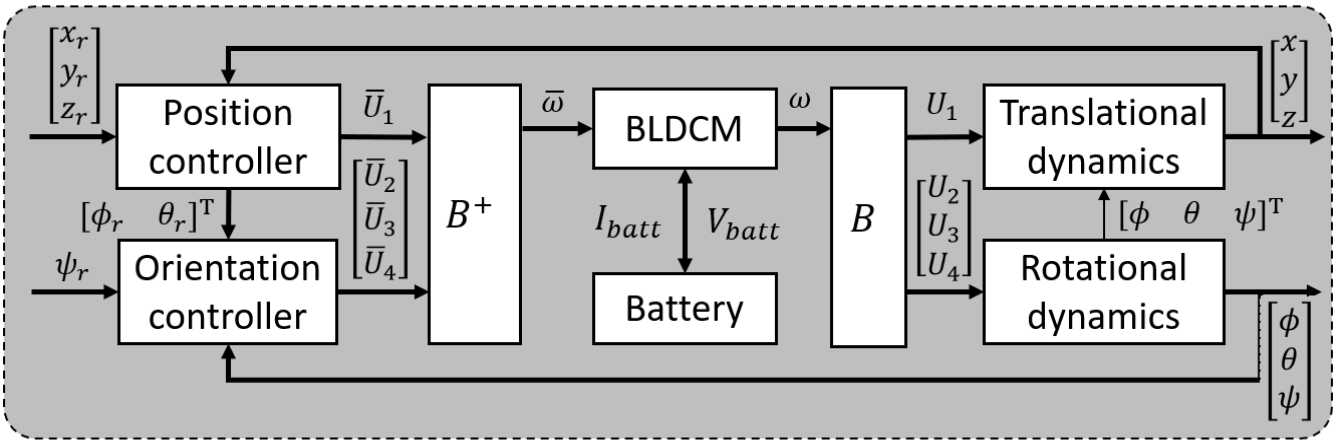

Figure 3.11: Hexarotor Cascade Control Loop.

Stabilization of hexarotor UAV

The stabilization of hexarotor UAV is performed by mean of orientation controller considering a PID control. The PID controller exhibits a simple structure with easy implementation. The general form of PID controller is

$$\begin{aligned} e &= x_d - x \\ u &= K_P\, e + K_I \int_0^t e\, dt + K_D \frac{d\, e}{dt}, \end{aligned} \tag{3.27}$$

where u is the control input, e is the difference between the desired state x_d and the present state x and K_P, K_I and K_D are the gains for the proportional, integral and derivative actions of PID controller. The computation of PID gains is explained in Appendix B by considering the hexarotor linear model (3.18).

In hexarotor, there are six states positions ξ and angles η, but only four control inputs. The interaction between the states and the total thrust and torques created by the BLDCMs are visible from nonlinear hexarotor dynamics defined by equations (3.13), (3.14) and (3.15). The total thrust U_1 affects the acceleration in the direction of the z-axis and holds the hexarotor in the air. The torques U_2, U_3 and U_4 have an effect on the acceleration of angles ϕ, θ, and ψ respectively. In that sense, the PID controllers to generate the control inputs are defined as follows ([105]):

$$\begin{aligned} U_1 &= \left(g + K_{P,z}(z_d - z) + K_{I,z} \int (z_d - z) + K_{D,z}(\dot{z}_d - \dot{z}) \right) \frac{m}{\cos\phi \cos\theta} \\ U_2 &= \left(K_{P,\phi}(\phi_d - \phi) + K_{I,\phi} \int (\phi_d - \phi) + K_{D,\phi}(\dot{\phi}_d - \dot{\phi}) \right) I_x \\ U_3 &= \left(K_{P,\theta}(\theta_d - \theta) + K_{I,\theta} \int (\theta_d - \theta) + K_{D,\theta}(\dot{\theta}_d - \dot{\theta}) \right) I_y \\ U_4 &= \left(K_{P,\psi}(\psi_d - \psi) + K_{I,\psi} \int (\psi_d - \psi) + K_{D,\psi}(\dot{\psi}_d - \dot{\psi}) \right) I_z, \end{aligned} \tag{3.28}$$

where g is the constant associated to gravity, m is the mass of hexarotor and I_x, I_y, I_z are the inertia moments around body frame. The result of hexarotor stabilization is shown in Figure 3.12 where all Euler

angles and z position have an initial condition at 0 rad and a reference of 0.25, 0.35, 0.5 rad and 1.5 m respectively. As it can be noted, the controller is capable to change the position and orientation from an initial state to a final state within a time window of 5 sec without static error. On the other hand, the control signals are plotted in Figure 3.13 where thrust (U_1) increase to 45 N at the take off and the torques ($U_{2,3,4}$) are limited to $\pm$ 4 Nm without sudden changes.

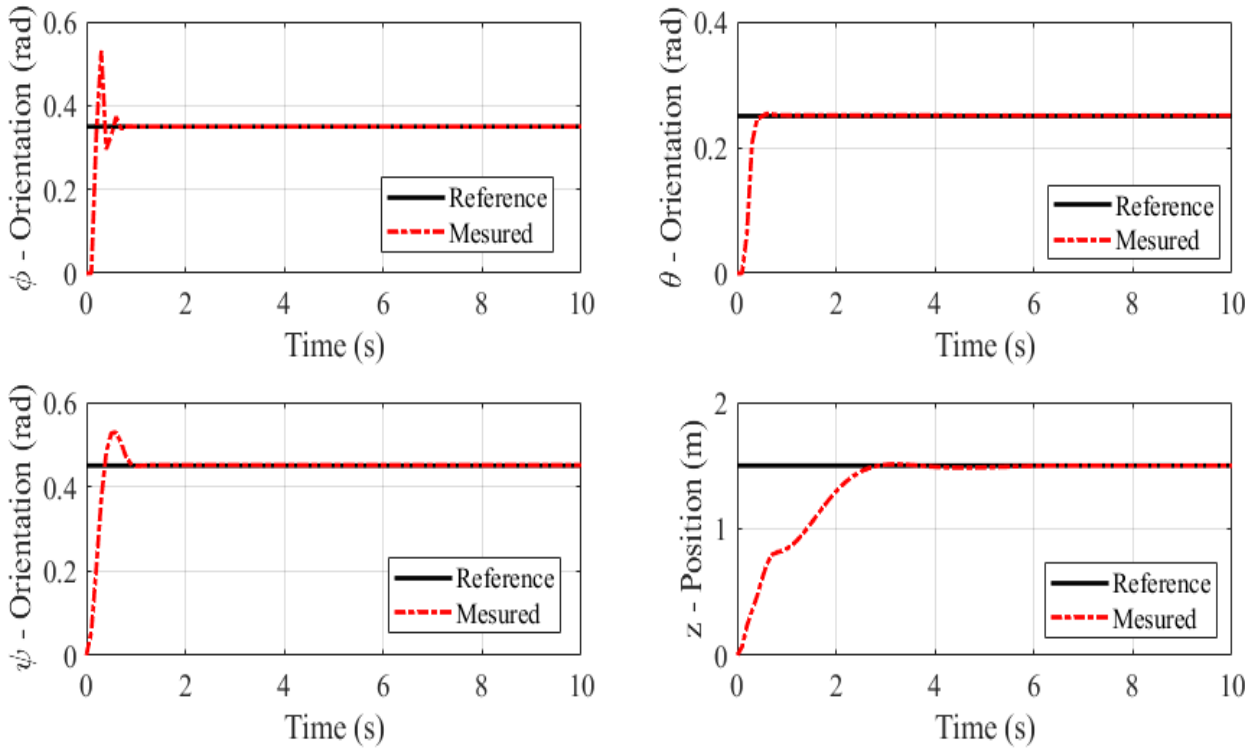

Figure 3.12: Result of hexarotor stabilization.

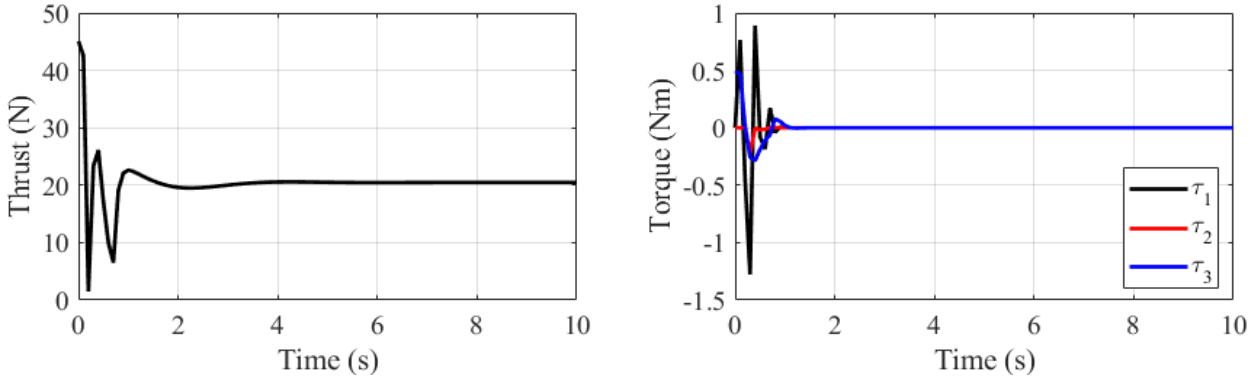

Figure 3.13: Control inputs.

The control inputs are used to determine the angular speed of BLDCM which are necessary to make the link between the propulsion system and hexarotor dynamics. Then, the relationship between the control inputs and angular speeds is established by considering (3.15) in matrix form $U = B\bar{\omega}$ as

$$B = \begin{bmatrix} b & b & b & b & b & b \\ -\frac{bl}{2} & \frac{bl}{2} & bl & \frac{bl}{2} & -\frac{bl}{2} & -bl \\ \frac{\sqrt{3}bl}{2} & \frac{\sqrt{3}bl}{2} & 0 & -\frac{\sqrt{3}bl}{2} & -\frac{\sqrt{3}bl}{2} & 0 \\ -d & d & -d & d & -d & d \end{bmatrix}, \tag{3.29}$$

where b and d are the thrust and drag constants and l is the distance from each motor to the center of mass of the hexarotor. From here, the control inputs generated by PID controllers (3.28) will be called as *reference control inputs* denoted as $\bar{U}_i$. Then, the relationship between the reference control inputs $\bar{U}_i$ and the effective control inputs actuating on the hexarotor U_i are determined by computing the reference angular speed of BLDCM $\bar{\omega}$. The angular speed for each BLDCM denoted by $\bar{\omega}$ is computed by Moonro-Penrose inverse of matrix B as $\bar{\omega} = B^{+}\bar{U}$ as:

$$B^{+} = \begin{bmatrix} \frac{1}{6b} & -\frac{1}{6bl} & \frac{\sqrt{3}}{6bl} & -\frac{1}{6d} \\ \frac{1}{6b} & \frac{1}{6bl} & \frac{\sqrt{3}}{6bl} & \frac{1}{6d} \\ \frac{1}{6b} & \frac{1}{3bl} & 0 & -\frac{1}{6d} \\ \frac{1}{6b} & \frac{1}{6bl} & -\frac{\sqrt{3}}{6bl} & \frac{1}{6d} \\ \frac{1}{6b} & -\frac{1}{6bl} & -\frac{\sqrt{3}}{6bl} & -\frac{1}{6d} \\ \frac{1}{6b} & -\frac{1}{3bl} & 0 & \frac{1}{6d} \end{bmatrix}. \tag{3.30}$$

Position Controller

Once the hexarotor stabilization is done by orientation controller, the next step is to generate the position controller around x-y axis. The relationship between the position and orientation in the hexarotor is established by linear model (3.18) where a change in roll and pitch angles generate a change in y and x position respectively. In that sense the PID controllers to generate the reference for roll and pitch angles are defined as:

$$\begin{aligned} \theta_d &= K_{P,x}(x_d - x) + K_{I,x}\int (x_d - x) + K_{D,x}(\dot{x}_d - \dot{x}) \\ \phi_d &= (K_{P,y}(y_d - y) + K_{I,y}\int (y_d - y) + K_{D,y}(\dot{y}_d - \dot{y}), \end{aligned} \tag{3.31}$$

The result of CCL considering the initial and final references as $[x_0\, y_0\, z_0\, \phi] = [0\,0\,0\,0]$ $[x_f\, y_f\, z_f\, \phi] = [2\,2\,2\,0.5]$ is shown in Figure 3.14 (a)-(b). According to (3.31) the controller around x-y axis generates the reference for pitch and roll angles as it can be noted in Figure 3.14 (b). Such changes are reflected in the control inputs in Figure 3.15 - (a) where the thrust is affected by the movement around x-y axis in addition the thrust in hover position is 18.64 N. On the other hand, the angular speed of the BLDCMs is shown in Figure 3.15 - (b) where angular speed per each BLDCMs in hover position is 454.7 rad/s.

In order to avoid unrealistic changes in BLDCM dynamics, a physical constraint is added in the angular speed of each motor as $\omega_i \in [0\,1200]$ rad/s. Such values are associated to parameters used in the simulation of BLDCM and according to motor characteristics, the angular speed limit can be different. In addition the hexarotor orientation has also constraint associated to maximum and minimum angular change as $\pm\frac{\pi}{2}$ for roll and pitch angles and $\pm\pi$ for yaw angle.

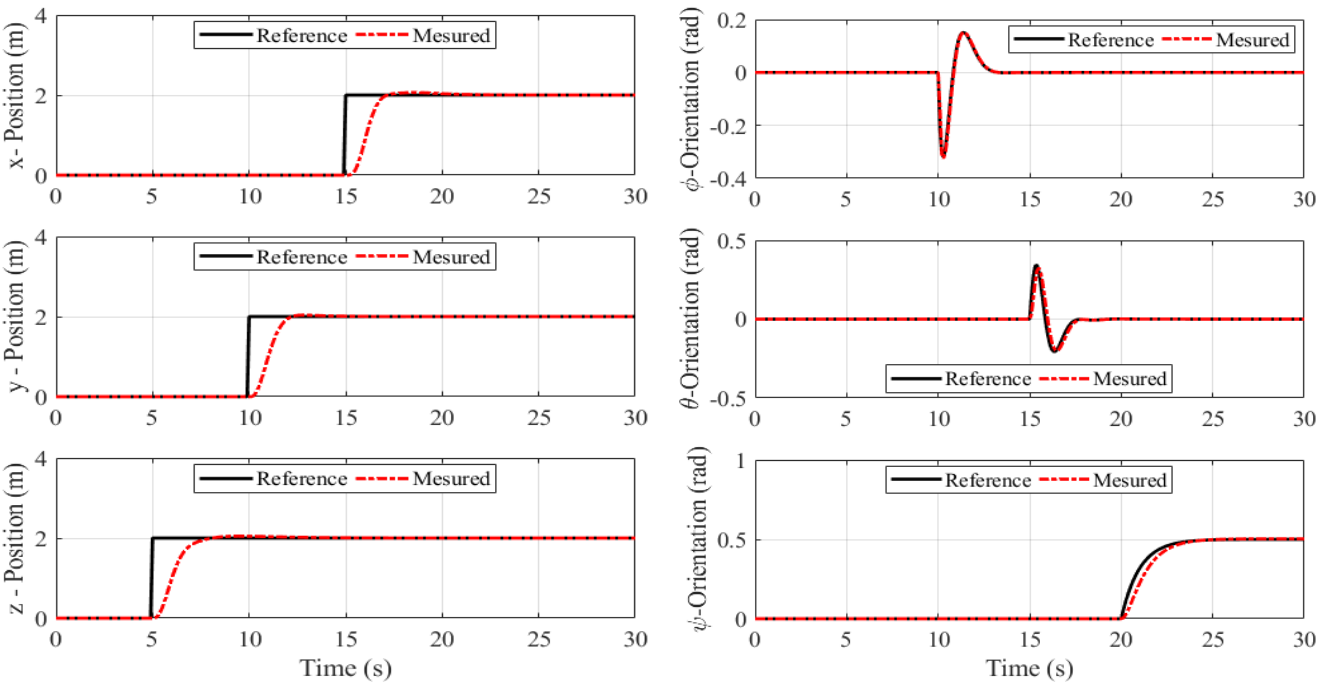

(a) (b)

Figure 3.14: (a) Hexarotor position $x-y-z$ axis. (b) Hexarotor orientation $\phi-\theta-\psi$ angles.

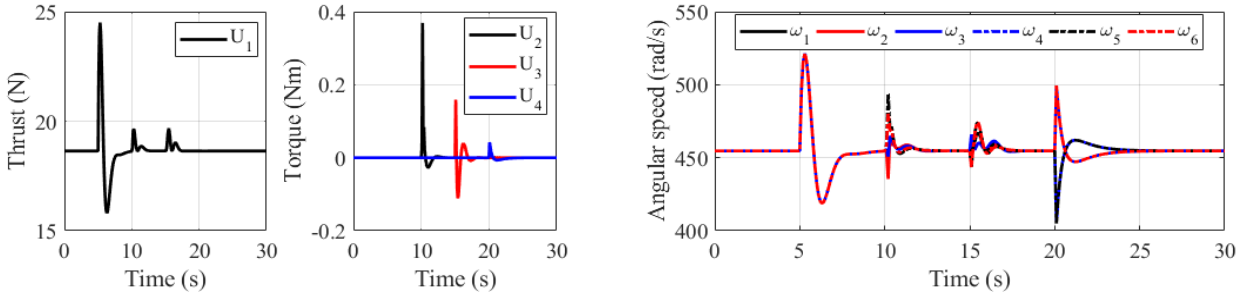

(a) (b)

Figure 3.15: (a) Control inputs. (b) Angular speed of BLDCMs.

3.4.2 Integration of Propulsion system in CCL

In order to analyze the effect of battery discharge on control loop and to establish the relationship between the maximum endurance and mission performance, the propulsion system (battery and BLDCM) is integrated in the CCL. Considering the reference control inputs $\bar{U}_i$ (computed by PID controllers) and the matrix relationship established in (3.30) the reference angular speed $\bar{\omega}_i$ is computed to generate the real control inputs U_i. Then considering the relationship established between the angular speed and BLDCM duty cycle:

$$Dc_i = f(\omega^2_{ref_i}), \tag{3.32}$$

the reference angular speed allows to define the link between the BLDCM dynamics and CCL to generate the thrust force and torques actuating in the hexarotor dynamics. In addition, by considering that current generated by each BLDCM is proportional to duty cycle, i.e.

$$\begin{aligned} \bar{v}_{batt_i} &= V_{batt} \cdot Dc_i \\ I_{BLDCM_i} &= \bar{i}_{batt_i} \cdot Dc_i, \end{aligned} \tag{3.33}$$

the dependence between reference control signals and battery discharge is established and integrated in the CCL. In Figures (3.16) - (3.20) the result of CCL with propulsion system is shown considering the same reference position than Figure (3.14). As it can be seen in Figure (3.16) there is no change in the position and orientation dynamics considering the effect of propulsion system and battery discharge. However, the reference control inputs $\bar{U}_i$ (black line) has a variation in comparison with the real control inputs $\bar{U}_i$ (red line), particularly the thrust force. This is due to reference control inputs generating the thrust force $\bar{U}_i$ increase to compensate the effect of battery discharge. Such phenomena is also presented in reference angular speed $\bar{\omega}_i$ (black line) in comparison with the angular speed generated by each BLDCM ω_i (red line) to produce the real control inputs U_i.

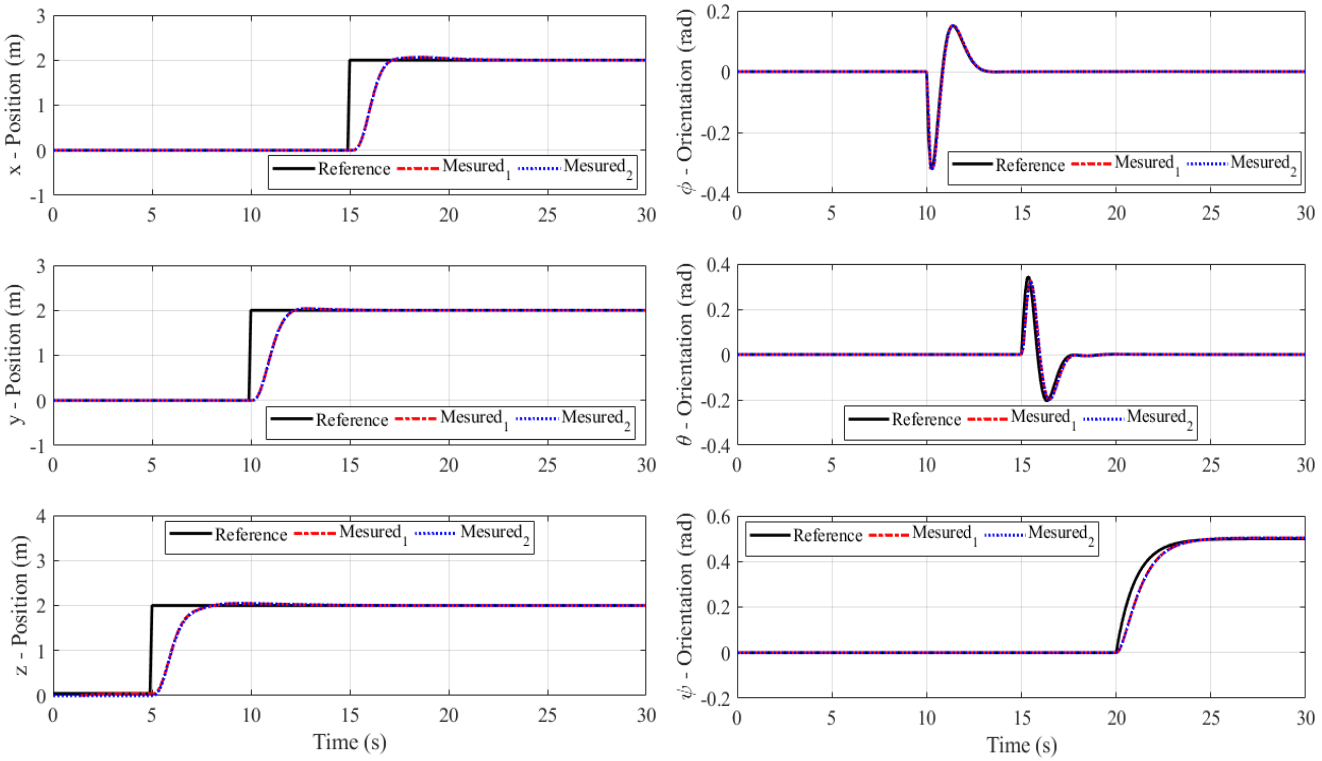

(a) (b)

Figure 3.16: (a) Hexarotor position $x-y-z$ axis. (b) Hexarotor orientation $\phi-\theta-\psi$ angles.

The evolution of BLDCM duty cycle and current generated according to position changes is shown in Figures (3.19) (a)-(b). Considering the position change in x-y-z axis and orientation in yaw angle the CCL adjusts the reference angular speed of BLDCM and consequently such changes modify the duty cycle and increase or decrease the current demanded for each BLDCM to the battery. In addition, as it can be noted in (3.19)-(b), the initial current for all BLDCM has an initial value of 2.48 A. This is due to the propulsion system considering the hovering condition which establishes that the BLDCM needs to produce the enough angular speed to generate the nominal thrust force necessary to compensate the gravity effect which is always actuating on hexarotor.

On the other hand, the current demanded by all BLDCMs presents different variations due to position changes as it can be seen in Figure (3.20). In hovering conditions, the total current is approximate 16 A and during the take off, the current increase to reach a value close to 21 A. In addition such variations causes that battery to discharge and the SoC be decreased in a small range.

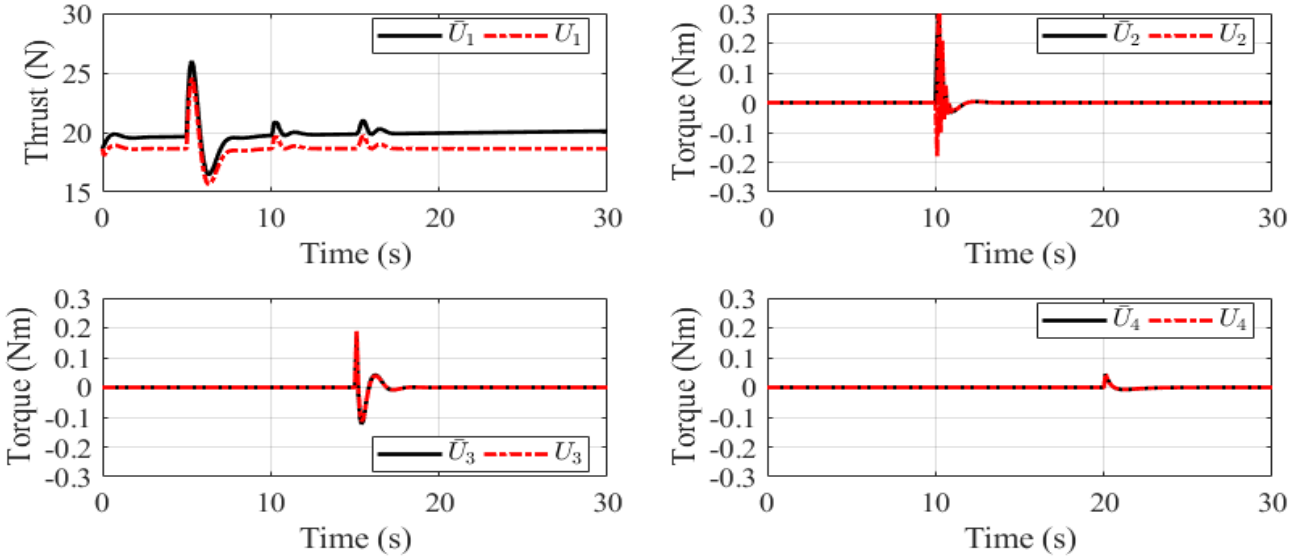

Figure 3.17: Control inputs.

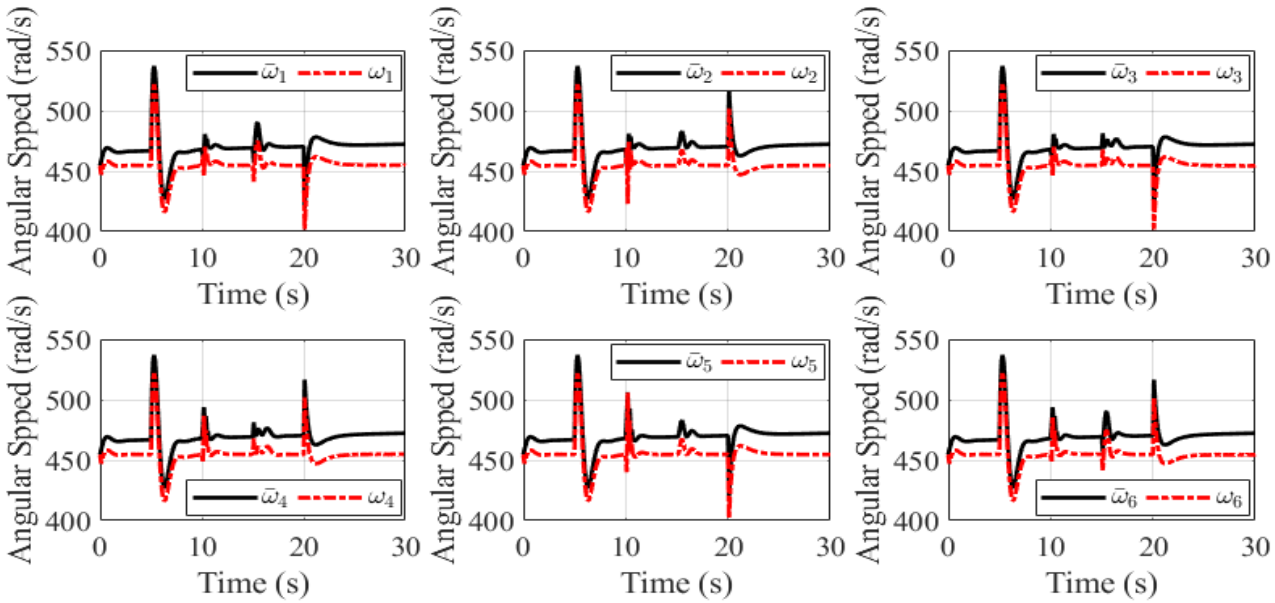

Figure 3.18: Angular speed of BLDCMs.

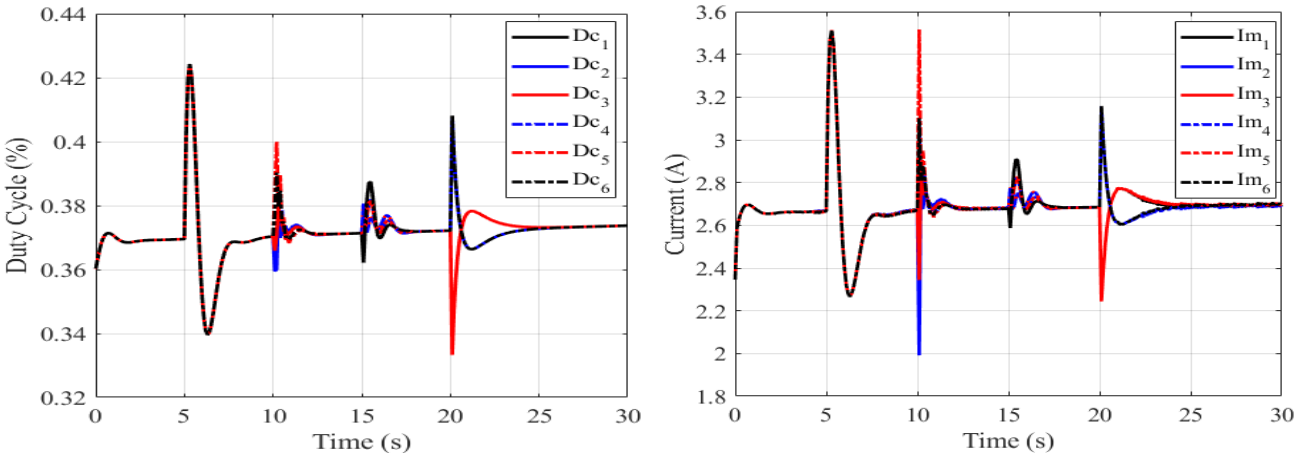

(a) (b)

Figure 3.19: (a) Duty Cycle per BLDCM. (b) Demanded current per BLDCM.

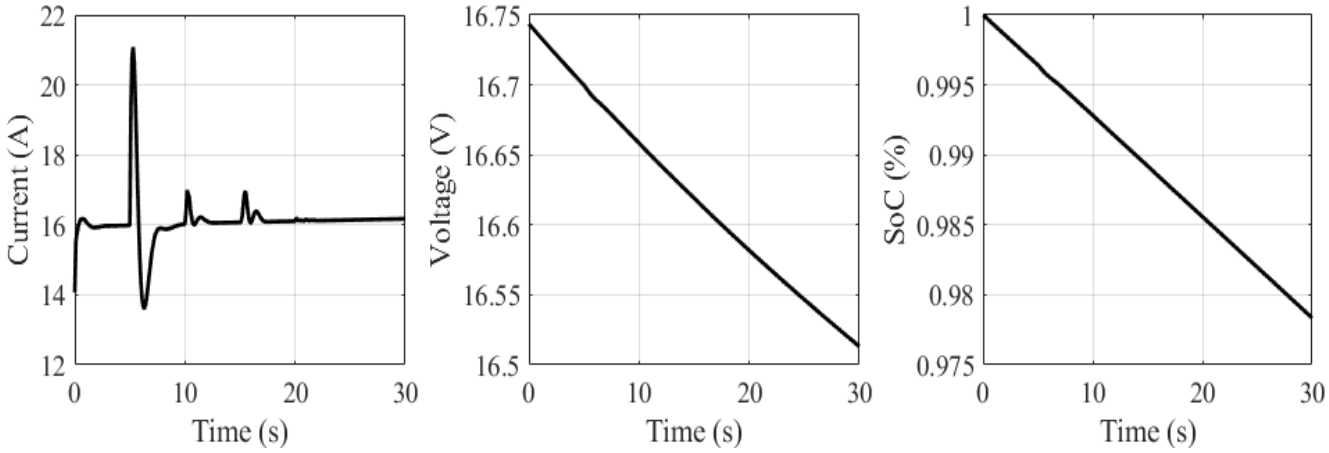

Figure 3.20: Battery response: current, voltage and State of Charge.

In order to analyze the battery discharge in a wide range of State of Charge, the hexarotor is required to follow a trajectory of longer duration as it can bee seen in Figures 3.21- 3.22. The height during the flight is kept constant and the position around x-y axis change according to reference position. The position change is directly reflected in hexarotor orientation around roll and pitch angles and the reference of yaw angle is kept at 0 rad. The thrust force and torques generated by the BLDCMs are plotted in Figure 3.23 where it can be observed that as the time passes and the battery is discharged the reference thrust force $\bar{U}_1$ (black line) tends to increase in order to compensate the battery discharge and to maintain the hexarotor lift during the flight. Such effect is also present in the evolution of BLDCM angular speed in Figure 3.24, where the reference angular speed $\bar{\omega}_i$ (black line) increase according to battery discharge. In addition, by considering the relationship between the reference angular speed, Duty Cycle and battery current defined in (3.26) and (3.25) the effect of battery discharge produces that Duty Cycle of each BLDCM increase which also increases the demanded current per BLDCM as it can bee seen in Figure 3.25. Finally, the battery response is plotted in Figure 3.26 where the current tends to increase according the discharge effect and it tends to exhibits different picks due to the position changes of hexarotor and the voltage decreases until reach a value around $\approx$ 14.87 V from its initial value of 16.74 V and reaching a final SoC value of

0.5 which means that the battery was discharged of 50 % of total charge.

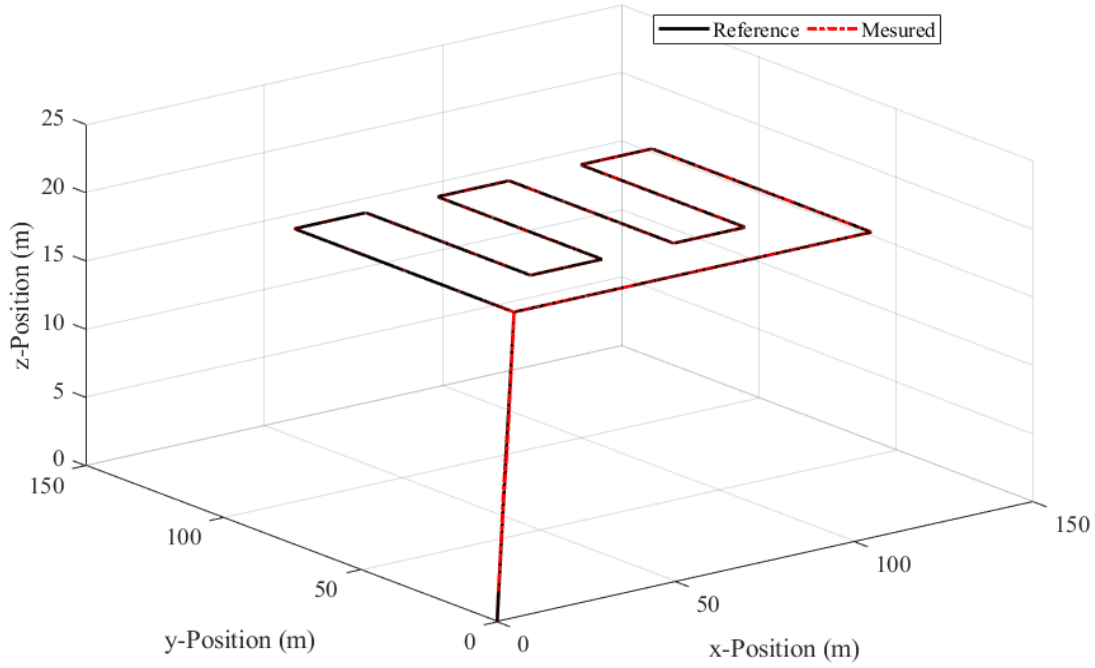

Figure 3.21: Hexarotor position in 3D view for a complete path.

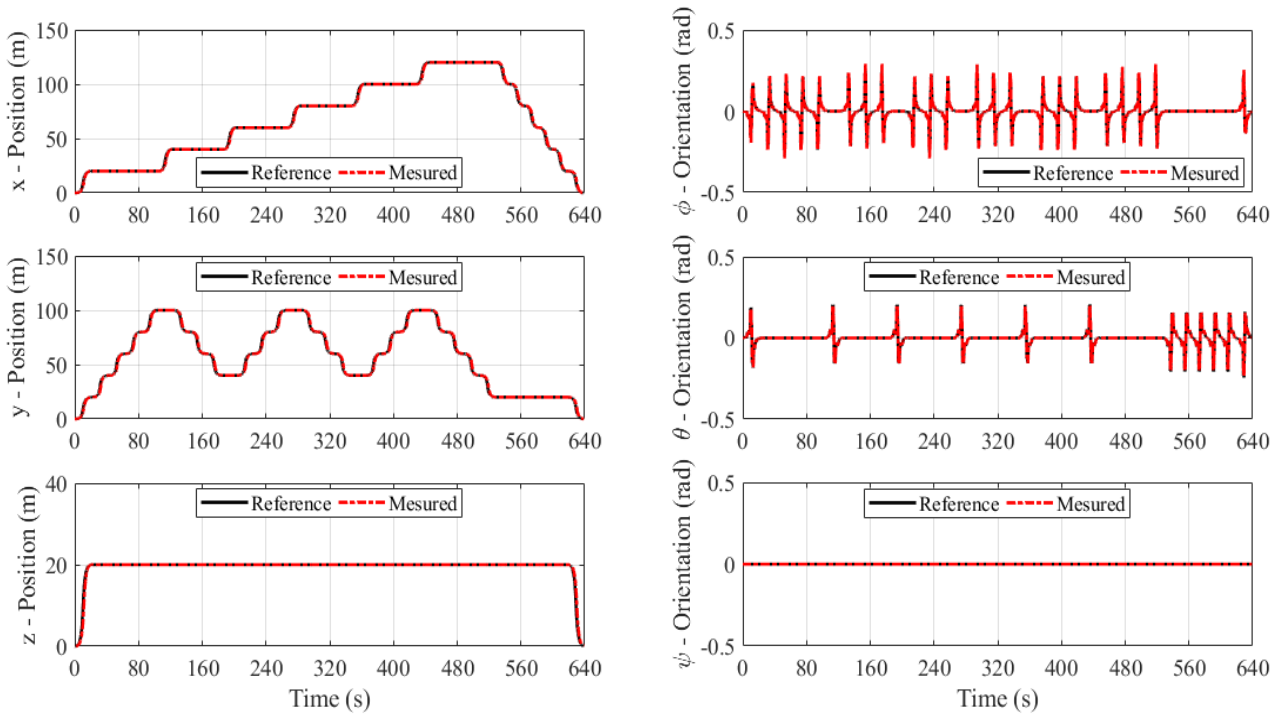

(a) (b)

Figure 3.22: (a) Hexarotor position $x - y - z$ axis. (b) Hexarotor orientation $\phi - \theta - \psi$ angles.

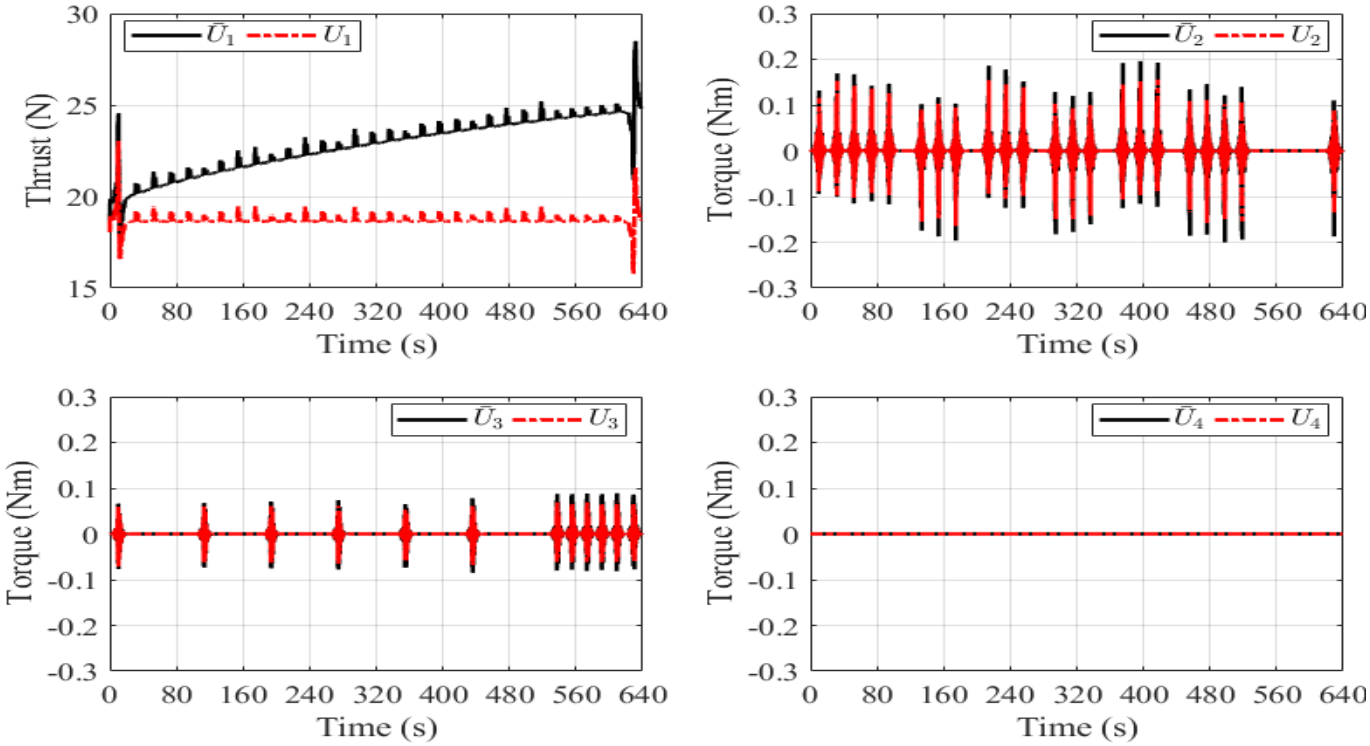

Figure 3.23: Control inputs.

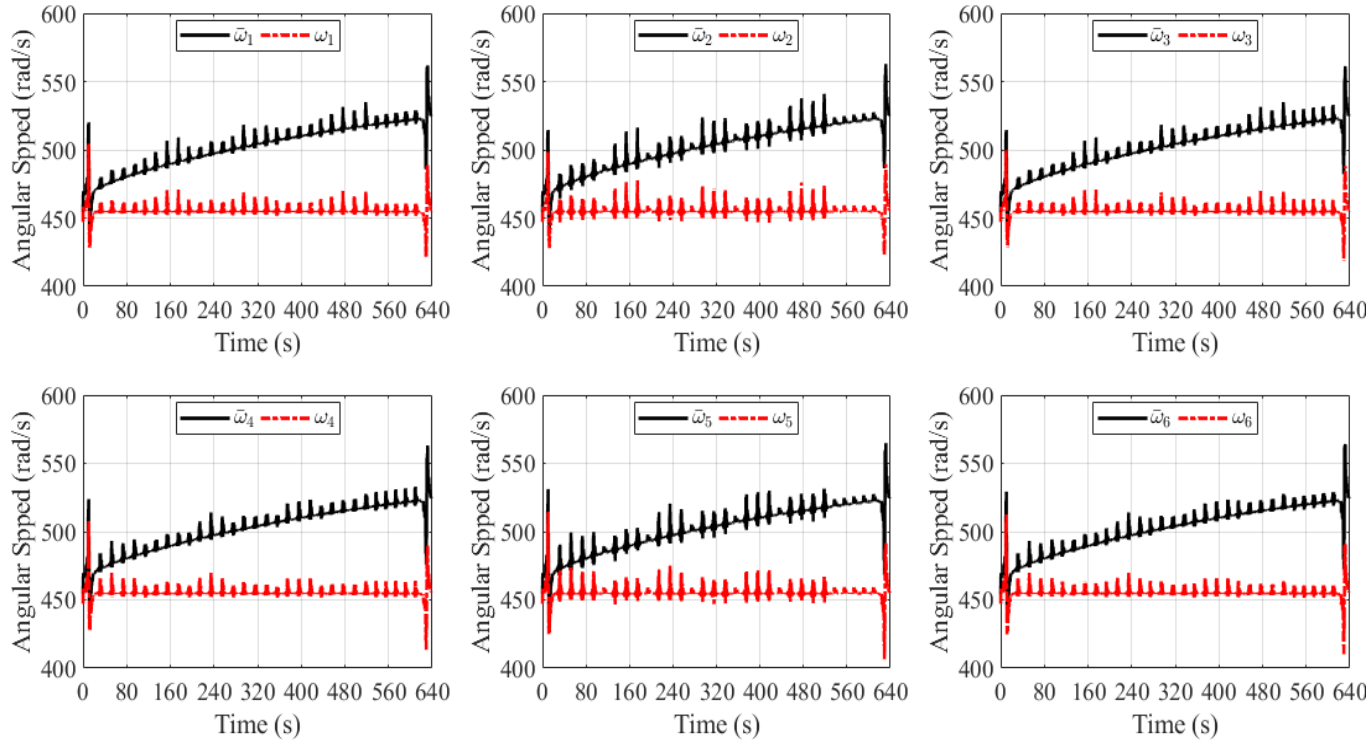

Figure 3.24: Angular speed of BLDCMs.

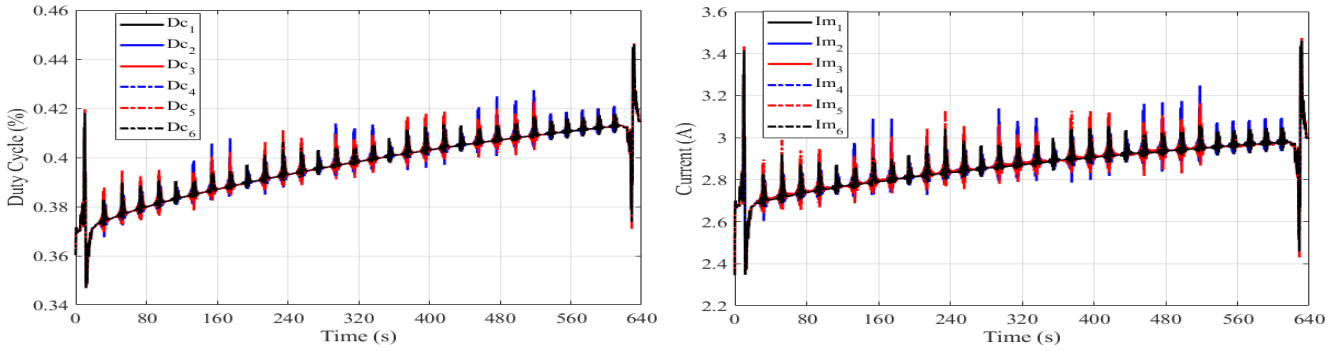

(a) (b)

Figure 3.25: (a) Duty cycle per BLDCM. (b) Demanded current per BLDCM.

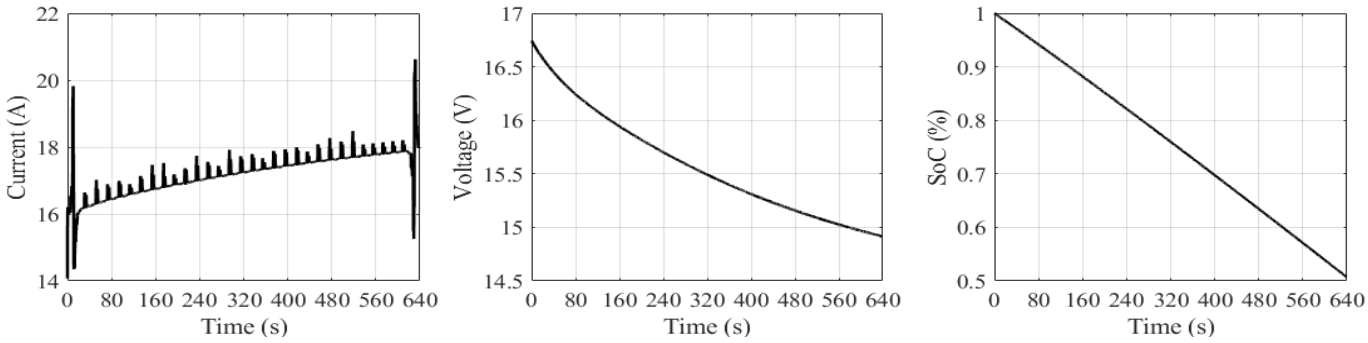

Figure 3.26: Battery response: current, voltage and State of Charge.

3.5 Conclusion

In this Chapter, the nonlinear mathematical model of hexarotor and propulsion system were presented. The position and orientation of hexarotor is mainly constrained to battery characteristics due to the effect of battery discharge on angular speed in each BLDCM. In order to compensate such effect and at the same time to stabilize the hexarotor orientation a Cascade Control Loop (CCL) based on classical PID controllers was proposed. The CCL allowed the interaction between the hexarotor dynamics and propulsion system by generating a dependency on control inputs generated by PID controllers with the angular speed of BLDCMs and its duty cycle. The CCL was initially designed around the linear model of hexarotor dynamics which was obtained by assuming hovering conditions and small angular changes. Such considerations leads to canceled different nonlinear terms, however the simulation results showed that the CCL is able to follow a reference trajectory and at the same time to compensate the effect of battery discharge take into account the minimum End of Discharge. In the next Chapter, the development of Prognosis and Health Management System will be presented considering the elements related to CCL described in this Chapter.

Chapter 4

Prognosis and Health Management of multirotor UAV

In this Chapter, the main elements integrating the Prognosis and Health Management module designed for the UAV hexarotor are presented. Such elements are summarized in Figure 4.1. In the top level the implementation of cascade control loop and its interaction with the propulsion system and multirotor dynamics is presented. On low level the Prognosis module and reference path link is shown. The Prognosis module takes information from battery as current (I_{batt}) and voltage (V_{batt}) in order to the mission time (t_m) be defined and the Remaining Useful Life (RUL) of battery be determined. The mission time is obtained through of the Flight Endurance (FE) prediction by considering the estimation of battery State of Charge (SoC). The FE predicted is evaluated by comparing the result with an empirical endurance model proposed in this research. This endurance model is determined according to battery characteristics as nominal voltage and capacity. Once the FE is obtained, the Remaining Mission Time (RMT) can be computed during mission execution. On the other hand, the battery RUL is computed by considering the battery State of Health (SoH) and evaluated through degradation models able to model the aging phenomena in the battery according to the number of charge/discharge cycles (n_{cycles}). In the following sections, the methodology used to develop such tasks will be explained.

4.1 Prognosis module

According to Figure 4.1, several characteristics of the system could be predicted, such as:

1. Battery SoC at a given time.
2. Fulfillment of a mission before to reach the EoD.
3. Flight endurance of multirotor and Remaining Mission Time (RMT).
4. SoH level and RUL for any degradation stage.

Depending on the accuracy level of the prediction and the complexity of the system behavior, different approaches have been used to perform prognosis ([34, 62]). The Model-based Prognosis or Condition-based Prediction assess the behavior of individual components of a system as well as the entire system based on a mathematical model that describe the evolution of some system variables (i.e. temperature, voltage, position, speed) over time. If such mathematical model exists, the future behavior of the system can be determined by propagating the mathematical model in the future time. However, to determinate a mathematical model of the interested system in order to perform a prediction of its future behavior is not a trivial task. First, it is necessary to define which system variables are necessary to evaluate the entire system behavior, and determine if such variables are directly measured or not. If such variables are

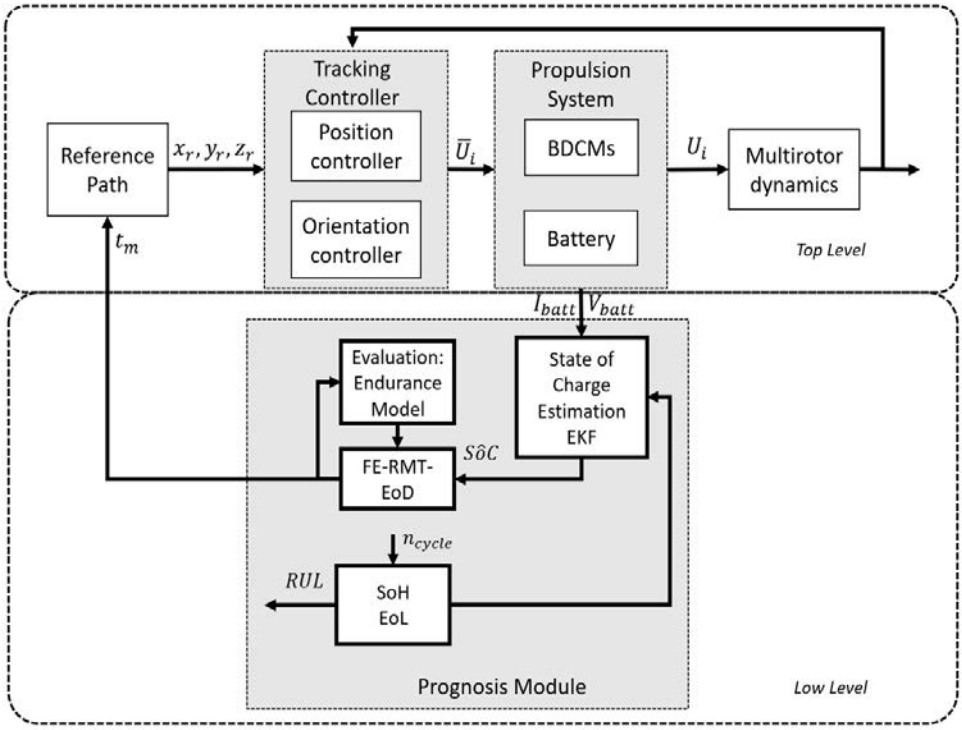

Figure 4.1: Prognosis and Health Management scheme in multirotor UAV.

measured, a mathematical model can be defined and used to perform the prediction in the future time. Otherwise, if such variables are unmeasured, they must be estimated. In that sense, this work presents in Figure 4.2 a Model-based Prognosis methodology based on an estimation of the battery SoC in order to predict the flight endurance of the UAV. The prediction is developed in three sequential steps: 1) estimation of unmeasured states of the system, 2) propagation and prediction of the estimated states, and 3) update of the prediction.

4.1.1 State Estimation

In several dynamic systems, not all state variables can be measured. For such cases, an observer needs to be designed in order to estimate the unmeasured states considering the system model and the available input-output signals. In this work, an Extended Kalman Filter (EKF) is used to estimate the battery SoC. The EKF has demonstrated to be an adequately tool to estimate the battery states as well as parameters in battery systems ([69, 136]). In this work, the EKF is developed considering a simplified mathematical model of system under study, where the unique nonlinear term is the Open Circuit Voltage. The EKF addressed the general problem of state estimation of a nonlinear system, expressed in discrete time as:

$$\begin{aligned} x_{k+1} &= f(x_k, u_k) + w_k \\ y_k &= g(x_k, u_k) + v_k, \end{aligned} \tag{4.1}$$

where $f(x_k, u_k)$ and $g(x_k, u_k)$ are the nonlinear state transition function and nonlinear measurement function, respectively, and they are assumed to be differentiable at each operating point. The random variables $w(t)$ and $v(t)$ are the process and measurement noise. They are assumed to be independent, white, and with normal probability distributions:

$$\begin{aligned} p(w) &\sim \quad N(0, Q) \\ p(v) &\sim \quad N(0, R). \end{aligned} \tag{4.2}$$

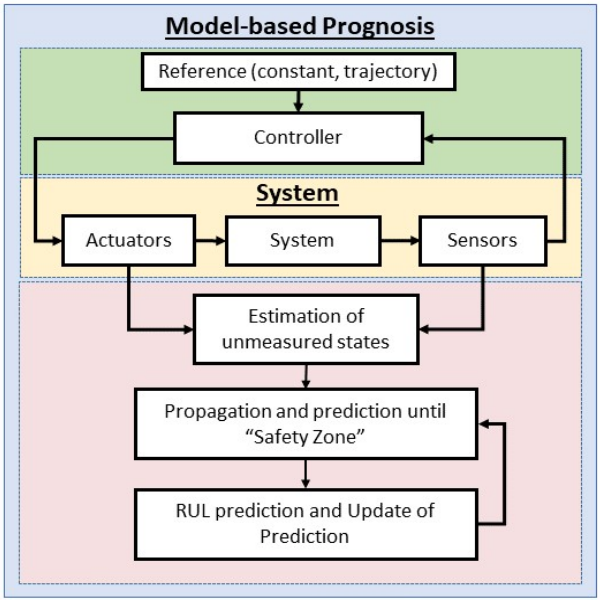

Figure 4.2: Model-based Prognosis methodology.

The matrices Q and R are the process noise covariance and measurement noise covariance, respectively. At each sample time, $f(x_k, u_k)$ and $g(x_k, u_k)$ are linearized through a first-order Taylor-series developed as

$$A = \left.\frac{\partial f(x_k, u_k)}{\partial x_{k-1}}\right|_{x_{k-1}=\hat{x}_{k-1}^-} \tag{4.3}$$

$$C = \left.\frac{\partial g(x_k, u_k)}{\partial x_k}\right|_{x_k=\hat{x}_k^-} \tag{4.4}$$

The completed equations of the EKF are resumed in Algorithm 1.

4.1.2 Propagation and Prediction of estimated states

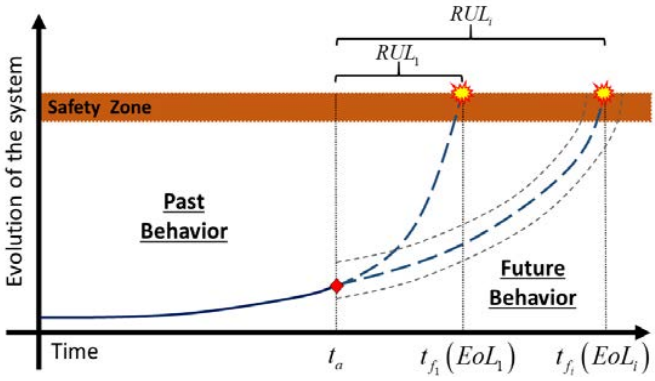

Figure 4.3: Evolution of the system behavior.

As mentioned previously, if a mathematical model that describes the evolution of system behavior as a function of the time exists, the prediction of future behavior can be determined by propagating the model

Algorithm 1 Extended Kalman Filter algorithm [136].

1. Initial values of $\hat{x}_{k-1}^{-}$ and P_{k-1}

2. To compute:
$$A_k = \left.\frac{\partial f(x_k, u_k)}{\partial x_{k-1}}\right|_{x_{k-1}=\hat{x}_{k-1}^{-}}$$
$$C_k = \left.\frac{\partial g(x_k, u_k)}{\partial x_k}\right|_{x_k=\hat{x}_k^{-}}$$

3. State estimate update:
$$\hat{x}_k^{-} = f(\hat{x}_{k-1}, u_{k-1}),$$

4. Error covariance matrix:
$$P_k^{-} = A_k P_k A_k^{\mathsf{T}} + Q,$$

5. Kalman gain:
$$K_k = P_k^{-} C_k^{\mathsf{T}} (C_k P_k^{-} C_k^{\mathsf{T}} + R)^{-1},$$

6. State estimate measurement update:
$$\hat{x}_k = \hat{x}_k^{-} + K_k(y_k - g(x_k^{-}, u_k)),$$

7. Error covariance matrix update:
$$P_k = (I - K_k C_k) P_k^{-}.$$

in the future time. However if the system involves unmeasured variables, they must be estimated first, and the prediction of their future behavior is based on the propagation of the estimated variables in the future. In order to illustrate how the propagation and prediction are performed, let us consider Figure 4.3 where the trend of the past evolution of system behavior at time t_a is known. It is possible to define a function that approximate the trend with the time, and propagate the function in the future until reaches the STZ. This function is called *prediction function*, and the accuracy of the prediction will depend on the amount of past data measure. On the other hand, the prediction function can be updated by using new data of the system. Due to the fact that there are no abrupt changes or discontinuities in the evolution of estimation SoC, the prediction function is defined as a polynomial function of the time, such as [162]:

$$\eta\,(t, \alpha) = \sum_{j=0}^{m} \alpha_j . t^j = \alpha_0 + \alpha_1 \cdot t + \cdots + \alpha_m \cdot t^m, \tag{4.5}$$

where $\eta(t)$ represents the predicted variable, t is the time, α_i are identified parameters associated to measured data trend and m is the order of the polynomial function. The method of *Weighted Least Squares (WLS)* is considered to estimate the parameters (α_i) of function (4.5). The WLS is defined as:

$$\begin{aligned} \mathrm{H} &= \begin{bmatrix} 1 & t & \cdots & t^m \end{bmatrix}, \\ \hat{\alpha} &= [\mathrm{H}^{\mathrm{T}}\mathrm{R}^{-1}\mathrm{H}]^{-1}\mathrm{H}^{\mathrm{T}}\mathrm{R}^{-1}\mathrm{Y}, \end{aligned} \tag{4.6}$$

where H contains the information of the relationship between the time and the polynomial order, $\hat{\alpha}$ is the vector with the estimated parameters α_i, R is the measurement covariance matrix, and Y is the vector of

the measured data (variable to be identified). The approximation is evaluated according to the coefficient of determination R^2, which is limited as $R^2 \in \left[\begin{array}{cc} 0.9 & 1 \end{array}\right]$ in this study, and the polynomial order depends on the accuracy between the data and the identified function. The iterative sequence of propagation and prediction is given in the Algorithm 2, where t_p is the so-called prediction time and it is larger than sampling time for SoC estimation.

Algorithm 2 Propagation and prediction algorithm.

1. Delay (t_p)
2. Recollect data until $\hat{SoC}(t_a)$
3. Define H and m for
$$\mathrm{H} = \left[\begin{array}{cccc} 1 & t & \cdots & t^m \end{array}\right]$$
and
$$\eta(t, \alpha) = \sum_{j=0}^{m} \alpha_j . t^j = \alpha_0 + \alpha_1 \cdot t + \cdots + \alpha_m \cdot t^m$$
4. Estimate $\hat{\alpha}$ with $Y = \hat{SoC}(t_0 : t_a)$
$$\hat{\alpha} = [\mathrm{H^T R^{-1} H}]^{-1} \mathrm{H^T R^{-1} Y}$$
5. Verify $\mathbf{R}^2$ to $Y = \hat{SoC}(t_0 : t_a)$ with $\eta(t_0 : t_a, \hat{\alpha})$
6. Propagate $\eta(t_0 : t_a, \hat{\alpha})$ until $t(SVT)$
7. Compute *Remaining mission Time (RMT)*
$$RMT = t(SVT) - t_a$$

4.2 Multirotor Flight Endurance

4.2.1 Endurance model

The flight endurance is directly related to energy and power capabilities of the battery. One way to determine the time when the battery is fully discharge is by mean the C-rate discharge properties ([119]), and it is expressed as

$$C_{rate} = \frac{I_{c/d}}{C_0}, \tag{4.7}$$

where C_0 is the nominal battery capacity and $I_{c/d}$ is charge/discharge current. $C_{rate} = 1$ means that a charge/discharge current similar to nominal capacity is applied to the battery, it will be charged or discharged in approximately one hour. Then considering such effect, the relationship between the current magnitude and time is described in Figure 4.4.

From Figure 4.4 it is possible to obtain a model able to compute maximum Flight Endurance as ([163]):

$$FE_{max} = a \cdot \exp^{b \cdot C_{rate}} + c \cdot C_{rate}^2 + d. \tag{4.8}$$

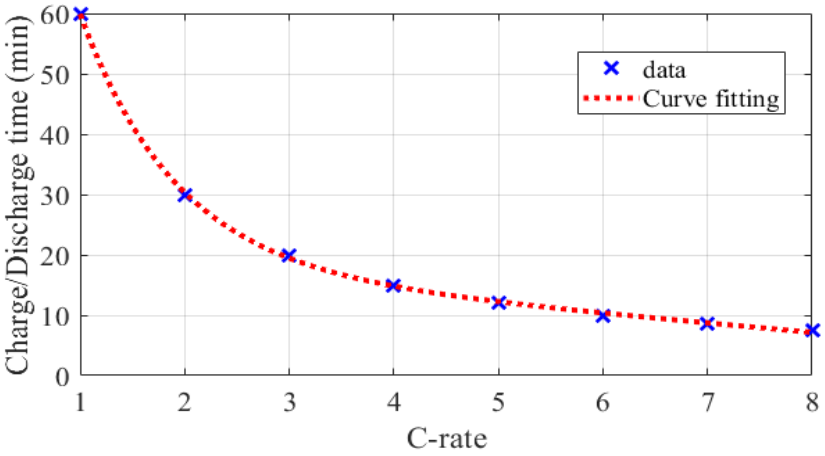

Figure 4.4: Relationship of C-rate and time.

The C-rate is computed from the total current as a function of the angular speed of the BLDCM and generated thrust. In that sense, the total thrust force to keep the vehicle lift in hover conditions according to (3.29) is represented as:

$$T = m\,g = \sum_{i=1}^{N_m} b\omega_i^2. \tag{4.9}$$

From (4.9), the angular speed of each BLDCM can be computed as:

$$\omega_i = \sqrt{\frac{T}{bN_m}}, \tag{4.10}$$

by considering the mechanical model of BLDCM (3.24) and the relationship between current and duty cycle (3.25), the total current demanded by all BLDCMs is computed as:

$$I_i = \left(d\omega_i^2 - D_f\omega_i - T_{fric}\right)\frac{Dc_i}{K_E}, \tag{4.11}$$

Finally, considering the existing relationship between the battery C-rate (4.7) and the total current, the flight endurance in hover condition is computed as with the equation (4.8). Such flight endurance allows to determine the maximum time between path and adjust the Prognosis Module to compute the flight endurance during the mission development.

4.2.2 Flight Endurance Prediction

During the development of a mission of some UAV, the End of Discharge (EoD) must be taking into account to ensure the safety of the UAV, the fulfillment of the mission, and the maximization of . In that sense, the *Flight Endurance* is considered as the time between the beginning of the mission until reaches a *Safety Voltage Threshold* before EoD value. In other words, the Flight endurance can be defined as the period of time that the battery is discharged from the maximum level of SoC, until the minimum level allowed. On the other hand, the *Remaining Mission Time* is established as the period of time that elapses between waypoints during vehicle navigation. Several factors are implied in the flight endurance of the UAV, such as the total current demanded by the number of the BLDCM ($I_{batt}(t)$), and C-Rate, the rate discharge (C), the initial State of Charge $SoC(t_0)$, and the State of Health SoH. Then, assuming a new and fully charged battery, the EoD is directly associated with the battery voltage. The time when EoD is reached can be computed considering the demanded current ($I_{batt}(t)$) through relation of C-Rate

discharge. However according to the number of charge/discharge, the capacity of the battery decreases and the discharge rate is modified as the aging of the battery increases. In that sense, the computing of EoD time should consider the effect of the aging to obtain the total flight endurance according to the battery SoH. Taking into account that the total current demanded by the set of BLDCM is known or measure, the SoC of the battery during the mission can be computed using equation (3.20) or estimated through EKF, and its future trajectory can be propagated and predicted in the future until reaching the EoD, leading to prediction of the flight endurance. The development of each step in the PHM architecture shown in Figure 4.2 to predict the flight endurance of the UAV is explained in the following subsection.

4.2.3 SoC estimation

The prediction of the FE is based on the evolution of battery SoC during the UAV mission. The SoC, as it was mentioned in Chapter 3 cannot be measured directly on the battery, in that sense, it needs to be computed or estimated. In this work two methods are considered to determine the battery SoC: 1) the direct computation of the SoC using the Ampere Counting method or Coulomb Counting method and 2) the estimation of the SoC using an EKF. In addition the Coulomb Counting method will be used to determine the *Real SoC* and it will be compared to SoC estimated with EKF.

Coulomb Counting method. This method takes into account the evolution of demanded current and its relationship with the nominal battery capacity:

$$SoC = SoC_0 - \frac{1}{C_0}\int_{t_0}^{tf} |I_{batt}|dt, \tag{4.12}$$

where SoC_0 is the initial SoC conditions at any time, C_0 is nominal battery capacity in Amperes per sec and I_{batt} is the battery charge/discharge current. As it can be noted, this method just depends on the battery current. However, this method accumulates errors in measurements and may lead to large SoC errors in real-world applications ([61]). In that sense, the estimation of SoC is considered based on the design of an Extended Kalman Filter applied on battery model (3.21).

EKF of Li-Po battery. The estimation of battery SoC using EKF method is developed according to Algorithm 1. Then, by considering the battery model

$$\begin{aligned}
\dot{V}_{SoC} &= -\frac{I_{batt}}{3600 \cdot C_T} \\
\dot{V}_d &= -\frac{V_d}{R_d \cdot C_d} + \frac{I_{batt}}{C_d} \\
V_{Batt} &= V_{OCV}(V_{SoC}) - V_d - R_{int}\, I_{batt} \\
V_{OCV}(V_{SoC}) &= \sum_{i=0}^{n} \lambda_i V_{SoC}^i + \ln(V_{SoC}) V_{SoC},
\end{aligned} \tag{4.13}$$

which is discretized through forward Euler method, and rewritten in state space form as

$$\begin{aligned}
x_{k+1} &= \begin{bmatrix} 1 & 0 \\ 0 & 1 - \frac{T_s}{R_d C_d} \end{bmatrix} x_k + \begin{bmatrix} -\frac{T_s}{C_T(N_{cycle})} \\ \frac{T_s}{C_d} \end{bmatrix} u_k + w_k \\
y_k &= \begin{bmatrix} \frac{\partial V_{OCV}(V_{SoC})}{\partial V_{SoC}^-} & -1 \end{bmatrix} x_k + R_{int}(N_{cycle}) u_k + v_k,
\end{aligned} \tag{4.14}$$

where the discrete state space vector is $x = \begin{bmatrix} V_{SoC} & V_d \end{bmatrix}^{\mathrm{T}}$, the input $u = I_{batt}$, the output $y = V_{batt}$, and T_s is the sampling time. The nonlinear term is the OCV shown in equation (4.13), which is in the

matrix C. The variation in the measurement noise is established at $\pm 0.1\,V$, according to experimental data, and the variation of process noise is $\pm 0.01\,V$ according to the registered current data. The process and measurement covariance matrices are defined as:

$$\begin{aligned} Q &= \begin{bmatrix} 1 \times 10^{-2} & 0 \\ 0 & 1 \times 10^{-2} \end{bmatrix} \\ R &= \begin{bmatrix} 0.1 \end{bmatrix}. \end{aligned} \tag{4.15}$$

The propagation and prediction of the estimated SoC is developed according to Algorithm 2. It is important to mention that the methodology shown in Figure 4.2, considers two types of sampling time during its implementation, i.e. whiles the state estimation stage is subject to the sampling time of the system (e.i. the sampling time will depend on the discretization stage) in order of millisec, the propagation and evaluation could be performed in a sampling time in the order of sec, or even minutes. In addition, the choice of sampling time for flight endurance prediction depends on both maximum endurance provided by battery characteristics and how often it is necessary to display the remaining mission time. In this work the remaining mission time is used to define the mission planning and re-planning strategy which will be explained in the following chapter.

4.3 Battery Health prediction

The battery State of Health describes the actual physical conditions of the battery in comparison with its nominal condition ([144]), and it is established in a range between 0 and 1 $SoH \in \begin{bmatrix} 0 & 1 \end{bmatrix}$, i.e. if $SoH = 1$ the battery is considered as new and $0 \leq SoH < 1$ the battery exhibits an aging behavior. The decrease of the battery SoH is mainly due to two aging processes: 1) the battery degradation associated to cyclic charge/discharge, and 2) the damage due to deep discharges (under EoD limit). These two aging processes lead to an energy loss, which is directly reflected in the battery voltage. As it can be seen in Figure 4.5 (a), the voltage range is $\approx 4.2 - 2.5$ V. The red line represent the voltage before to reach the concentration zone (around 3.22 V). In addition, event thought the battery SoH decreases proportionally to the number of charges/discharges, the initial SoC does not present changes due to *memory effect* which causes the battery to store only the charge associated with the actual capacity C_T value. Additionally, the memory effect inhibits the visualization of the energy loss provoked by the aging ([158]). On the other hand, the energy loss is the result of active materials transformation in inactive phases and leading to a reduction of battery capacity (*capacity loss*) at any discharge rate, and the increase of the battery impedance (*power fade*). Both capacity loss and power fade are related to the internal parameters of the battery. The capacity loss is evidenced by the reduction of the capacity C_T, and the power fade by the increase of the internal resistance R_{int} ([36]), and both phenomenas are proportional to the number of battery charge/discharge (N_{cycle}), as it can be seen in Fig. 4.5 (b)-(c). Furthermore, the variation of capacity and internal resistance make possible to quantify the aging level and consequently the battery End-of-Life (EoL).

Remark 1. The EoL determines when the battery has reached its useful life, and it could be associated to a specific SoH value, e.g. in ([68]) it is reported that the life of a battery cell is ended when the maximum power of the cell decreases to 60% compared to its initial maximum power at the same operational conditions. In that sense, it can be assumed that a decrease of total capacity C_T and an increase of the internal resistance R_{int} of 0.6 (interpreted as 60%) determines the EoL of a cell. This EoL definition is established for a single battery cell, however it is possible to extend it for a battery made of several individual cells by assuming that the operational conditions and the aging behavior caused by the use are similar for all cells.

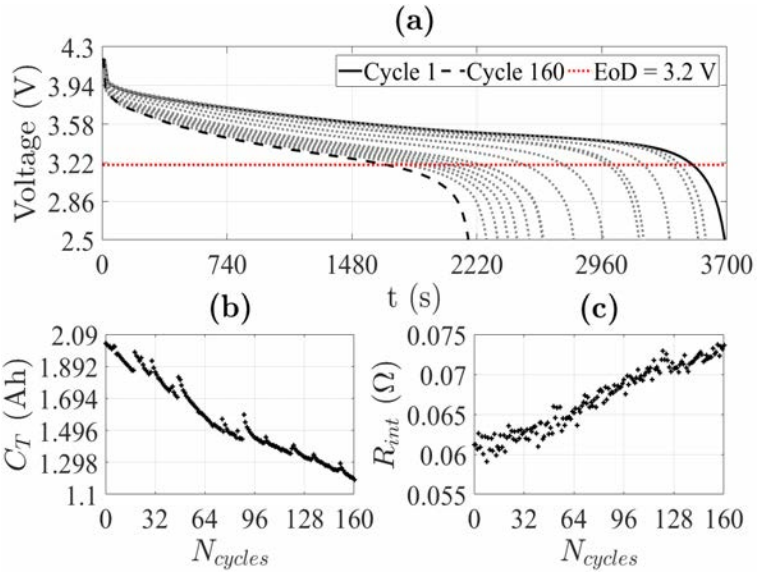

Figure 4.5: (a) Voltage variation of a cell subjected to discharge cycles. (b) Evolution of capacity C_T and (c) Internal resistance R_{int} ([153]).

In this work, the energy loss is modeled by considering the capacity loss and the power fade using experimental data. Both phenomena are related to number of charge/discharge cycles and modify the battery parameters described in (4.13).

Capacity loss model. The Capacity loss model denoted as C_{loss} is defined by considering that the battery capacity (C_T) varies inversely proportionally according with the number of charges/discharges (N_{cycle}), and it is expressed as:

$$C_{loss}(N_{cycle}) = 1 - \frac{C_0 - C_T(N_{cycle})}{C_0}, \tag{4.16}$$

where C_0 is the initial capacity when the battery is new, $C_T(N_{cycle})$ is the capacity after each discharge cycle, $C_{loss}(N_{cycle}) \in \left[\ C_{loss}(EoL) \quad 1\ \right]$, i.e. when $C_{loss} = 1$ the battery is new and when $C_{loss}(EoL) \leq C_{loss} \leq 1$ the battery is in a degraded state. The result of (4.16) applied to experimental data presented in ([153]) is shown in Figure 4.7 (a). As it can be noted, the capacity loss has a decrease of 0.4 (which can be also interpreted as a decrease of 40%) after 160 charge/discharge cycles, and it is occurs before it reaches the EoL, i.e. a SoH of 0.6 (60%) according to **Remark 1**. Then, using experimental data of capacity loss, a model able to characterize the trend of capacity loss is identified using polynomial functions as it be seen in Figure 4.6.

In Figure 4.6, three polynomial functions are compared using Prediction Bounds (PB) of 90% in order to determines which adjust the capacity loss trend. As it can be noted a polynomial fourth-order equation allows to capture the capacity loss trend within of PB without without overdetermining the model as:

$$IM_{C_{loss}}(N_{cycle}) = \sum_{i=0}^{4} \alpha_i \cdot N_{cycle}^i \tag{4.17}$$

where α denote the polynomial coefficients. The comparison between the identified model (4.17) and the

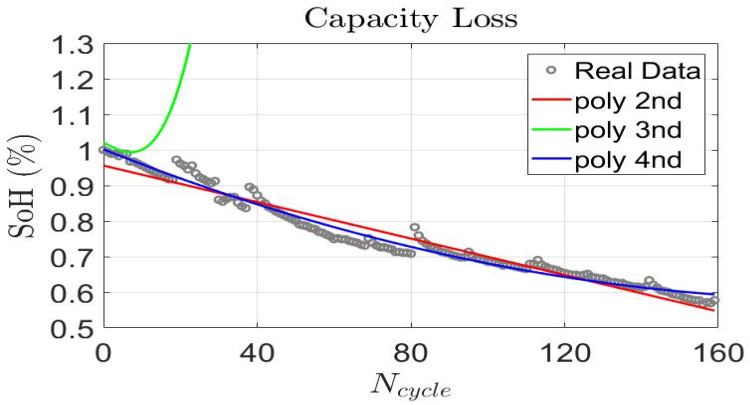

Figure 4.6: Fitting of capacity loss with polynomial functions.

experimental data are shown in Figure 4.7 (b), where IM denotes the Identified Model and PB are the Prediction Boundaries.

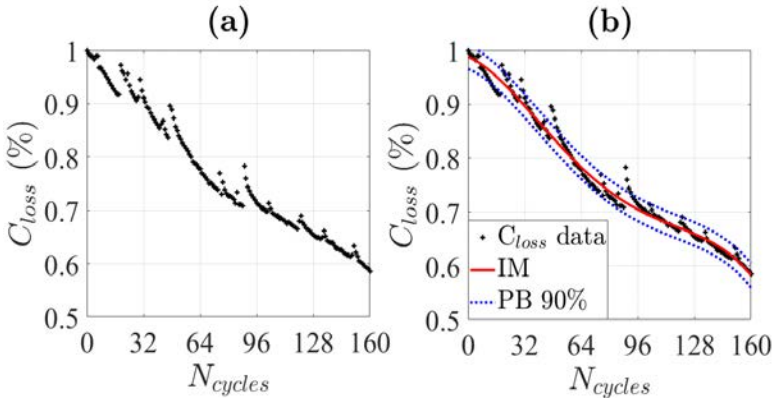

Figure 4.7: (a) Evolution of Capacity loss C_T. (b) Identification of Capacity loss model.

Power fade model. The power fade model is denoted as R_{inc}. Considering that the battery internal resistance R_{int} varies proportionally to the number of charges/discharges (N_{cycle}), R_{int} is expressed as:

$$R_{inc}(N_{cycle}) = 1 - \frac{R_f - R_{int}(N_{cycle})}{R_f - R_0}, \tag{4.18}$$

where R_0 is the initial internal resistance when the battery is at the Begin of Life, $R_{int}(N_{cycle})$ is the internal resistance value according to each discharge cycle, R_f is the value of the internal resistance when the battery has reached its End of Life (EoL). $R_{inc}(N_{cycle}) \in [\ 0 \quad R_{inc}(EoL)\ ]$. In Figure 4.8 (a), the increase of the internal resistance computed by (4.18) is shown. As it can be noted, the internal resistance has an increase of 0.4 (interpreted as an increase of 40%) after 160 charge/discharge cycles, and it is occurs before it reaches the EoL. Furthermore, R_f is established at 0.6 (60%) according to **Remark 1**. For the degraded behavior computed by (4.18), a model is identified using a polynomial second-order equation:

$$IM_{R_{inc}}(N_{cycle}) = \sum_{i=0}^{2} \beta_i \cdot N_{cycle}^i \tag{4.19}$$

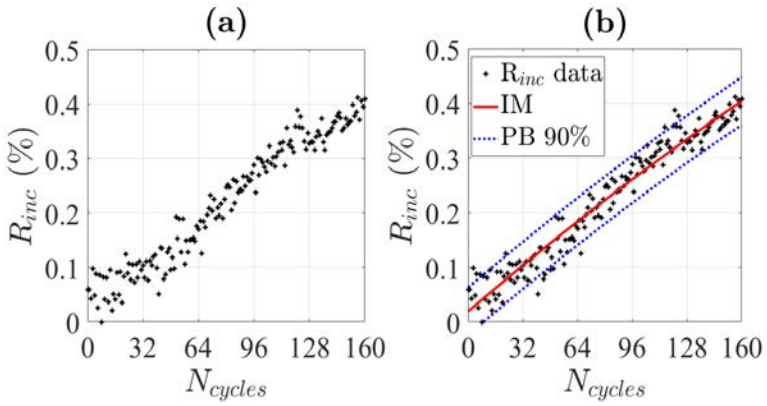

Figure 4.8: (a) Evolution of internal resistance R_{int} according to N_{cycle}. (b) Identification of power fade model.

where β_i denote the polynomial coefficients. The comparison between the identified model (4.19) and the experimental data are shown in Figure 4.8 (b). Finally, the total capacity C_T and the internal resistance R_{int} in system (3.19) are rewritten as:

$$\begin{aligned} C_T &= C_T(N_{cycle}) \cdot IM_{C_{loss}}(N_{cycle}) \\ R_{int} &= R_{int}(N_{cycle}) \cdot IM_{R_{inc}}(N_{cycle}). \end{aligned} \tag{4.20}$$

Remark 2. Models (4.17) and (4.19) are computed considering only the degraded behavior of a single battery cell, and both models are dependent on the number of charges/discharges cycles N_{cycle}. In that sense, for other batteries with different capacity C_T and internal resistance R_{int} values, it is possible to obtain similar degraded models, and the order of the polynomials was determined to best fit the experimental data (Table 4.1).

Table 4.1: Coefficients of identified models

Capacity loss model $\mathbf{C_{loss}}$					
α_0	α_1	α_2	α_3	α_4	$\mathbf{R^2}$
0.988	-1.406×10^{-3}	-6.713×10^{-5}	7.651×10^{-7}	-2.435×10^{-9}	0.98
Power loss model $\mathbf{R_{inc}}$					
β_0	β_1	β_2	-	-	$\mathbf{R^2}$
2.9×10^{-2}	4.027×10^{-3}	-2.604×10^{-6}			0.95

The algorithm proposed to predict the Flight Endurance and Remaining Mission Time is tested at simulation level considering the mathematical model of hexarotor and propulsion system. The Li-Po battery considered in the propulsion system is composed by four cells with a capacity of 6.2 Ah. Considering the relationship between the battery voltage and the SoC, a voltage limit defined as Safety Voltage Threshold (SVT) is defined according to Figure 4.9. As it can be observed, before the voltage reaches the EoD, there is an abrupt exponential fall of voltage. Taking into account this phenomena, the SVT is defined before the voltage reaches the EoD.

The UAV was subjected to a mission which consisted in following circular trajectory with an area of 785400 m^2 around $x - y$ axis and an altitude of 20 m (Figure 4.10). Such trajectory was developed considering

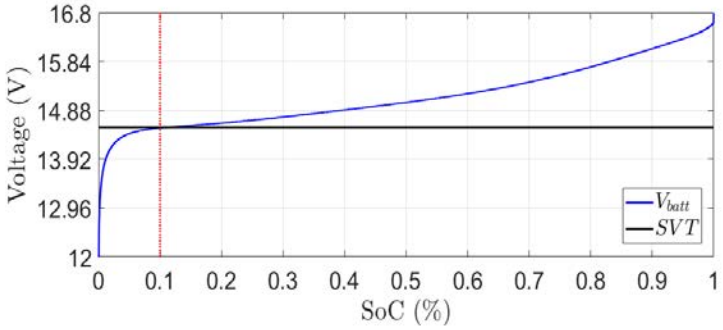

Figure 4.9: Safety Voltage Threshold of the Li-Po battery.

the mathematical model of UAV presented in Chapter 3. Considering that the battery is fully charged and new, the initial SoC and SoH were established at 1 respectively.

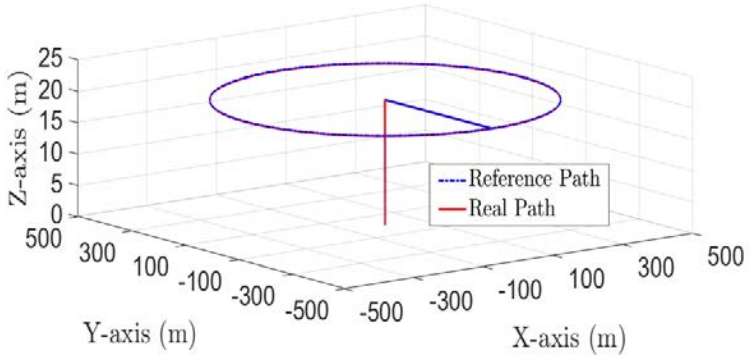

Figure 4.10: 3D Path of hexarotor UAV.

The current generated by the six motors is shown in Figure 4.11-(a). The variations in the current are due to velocity changes of the motors caused by the UAV movement. The comparison between the voltage battery and its estimation is observed in Figure 4.11-(b). As it can be seen, the mission is fulfilled in 20 minutes before to reach the SVT,and this avoided an overdischarge in the battery.

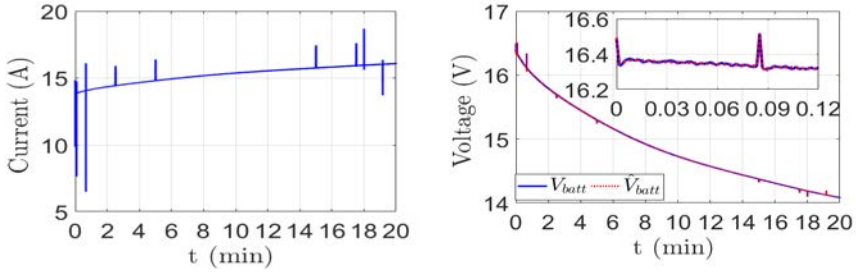

(a) (b)

Figure 4.11: (a) Demanded current I_{batt} and (b) comparison between battery voltage and $\hat{V}_{batt}$.

The comparison between the estimated SoC through the EKF and the computed SoC by Coulomb Counted is shown in Figure 4.12. As it can be noted, the SoC estimation through the EKF relates the SoC with the dynamic of the battery discharge. This relationship allows to predict the flight endurance from the

estimated SoC.

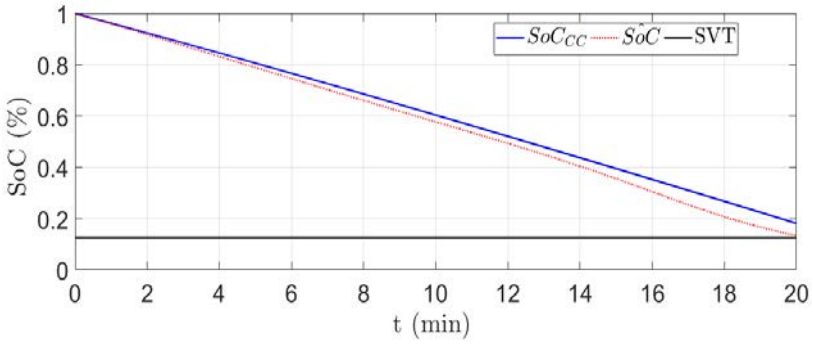

Figure 4.12: Comparison between SoC_{CC} and $\hat{SoC}$.

The propagation and prediction was developed over sampling time of 1 minute, and the SoC estimation each 10 millisec to collect enough data to estimate the parameters of the prediction function (4.5). Two 1^{st} and 2^{nd} order polynomials were considered for the prediction function. The predictions of the total flight endurance for both prediction functions are plotted in Figure 4.13. The blue marks correspond to the predicted flight endurance with the 1^{st} order polynomial, and the red marks with the 2^{nd} order polynomial. As it can be observed, the first predictions ($1-4$ min) with the 1^{st} order polynomial are closer to the real flight endurance, whilst an approximation of the real flight endurance is displayed from 6 minute onwards with the 2^{nd} order polynomial. However the closest prediction of real flight endurance is obtained at time 8 min with the 2^{nd} order polynomial.

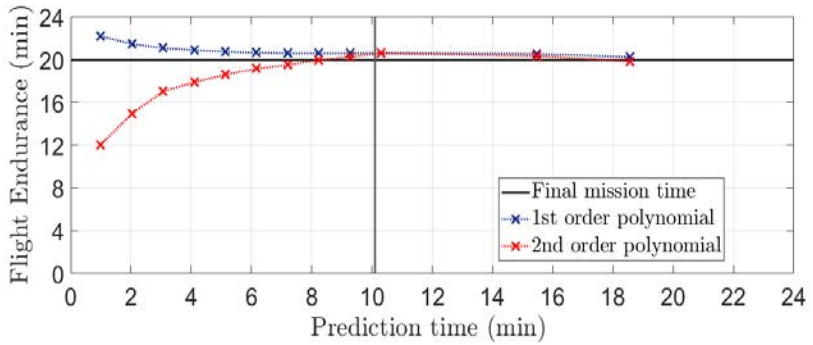

Figure 4.13: Comparison between the predictions of both prediction functions.

In Figure 4.14 and Figure 4.15 the results of the prediction for the 1^{st} and 2^{nd} order polynomial at time 1, 6 and 8 min, and their comparison with the estimated SoC are shown. A *Decision Threshold (DT)* at the 0.6% (at time 10 min of the total flight endurance) of estimated SoC was defined to determine an operation range where the predictions will be useful to take decisions on the progress of the mission. The computation of Remaining Mission Time (RMS) was made from the first prediction, and the results are shown in Figure 4.16. As it can be seen, it is possible to predict the total flight endurance and the RMS from the beginning of the mission considering the defined DT.

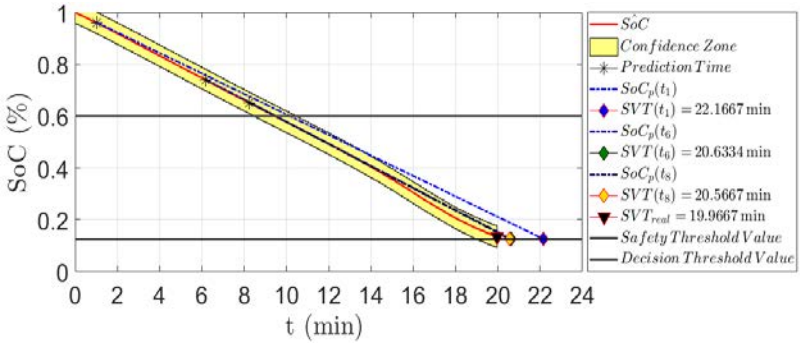

Figure 4.14: Prediction of flight endurance with 1^{st} order polynomial.

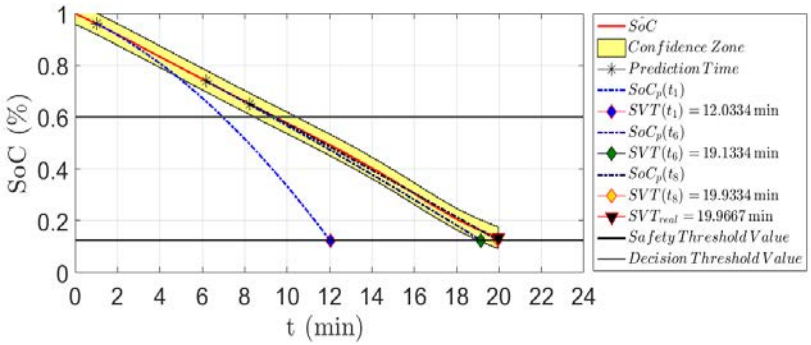

Figure 4.15: Prediction of flight endurance with 2^{st} order polynomial.

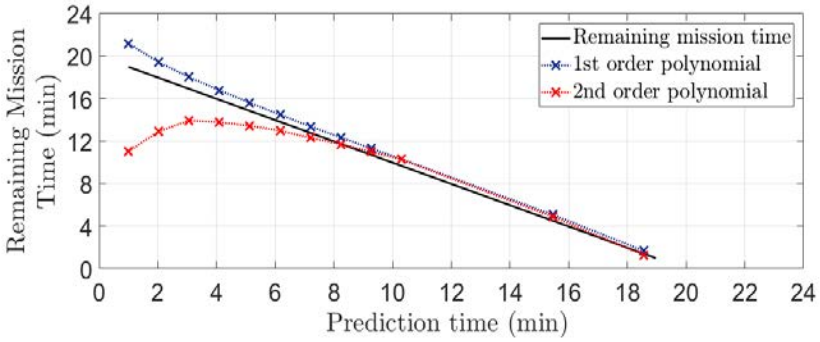

Figure 4.16: RMT staring from the first prediction.

4.4 Conclusions

In this Chapter the Prognosis and Health Management around hexarotor was developed which is focused on battery dynamics. The Prognosis Module executes different tasks in order to determines the actual battery conditions. The FE prediction as a function of SoC estimation allows to determines the maximum endurance according to endurance model. In addition by taking into account the effect of aging into the FE prediction it is possible to determines the mission fulfillment for all range of battery SoH. In the next chapter, the link between the Prognosis Module and Mission Planning methodology will be presented as well as the simulation results.

Chapter 5

Energy aware mission planning

In this Chapter, the main elements around the proposed mission planning strategy are defined considering the link between the Prognosis Module developed in the previous Chapter and the path planning task methodology. The path planning is performed considering the energy consumption during the mission. In Section 5.1 the mission planning strategy will be explained by describing the necessary elements to carry out the mission as mission requirements, way-point definition, path generation and flight endurance prediction. In Section 5.1.2 the path planning based on energy consumption will be developed considering two approaches: polynomial approach generation and optimal path planning. Finally the simulation results integrating the prognosis module are presented in Section 5.2.

5.1 Mission planning strategy

According to ([168]), the mission planning includes all those items related to *operation modes* during the vehicle flight and how them allows to increase the flight efficiency. Such operation modes demand more versatility in the face of changing mission objectives and environment specifications, as well as adaptability to uncertain events in the immediate and broader environments, good performance and robustness. The main requirement is to have an autonomous vehicle able to execute a *task-selection* and a *decision-making* to performed a motion for a given objective and executed them. During the task selection, the UAV must make plans taking into account the available information about the course of the mission and consequently takes decisions. *Decision-making* determines the main important requirements as the choice of the way-points, energy available and flight endurance, and it evaluates possible environment uncertainties. In sequential, during decision-making, the UAV seeks to choose the best actions based on its observations of the world.

On the other hand, path planning deals with the trajectory algorithmic development based on the available information of the mission ([168]). Depending on mission requirements, it is possible to contain slow or fast speed paths, short or long distance between way-points, and in special cases, the UAV should stay in a particular position for a certain period of time. A multirotor UAV must be able to performance mission considering:

- Perceive its environment and consequently update its activity and response to changes in its own state,
- Control the actuators and keep as close as possible to the planned path despite un-modeled dynamics, parametric uncertainties and sensor noise,
- Regulate its motion with respect to the local environment,

- Be able to avoid obstacles and other UAV and assess the information from the multi-sensor environment,

- Be able to assess its *current condition* and determine if it meets the requirements of the mission on course.

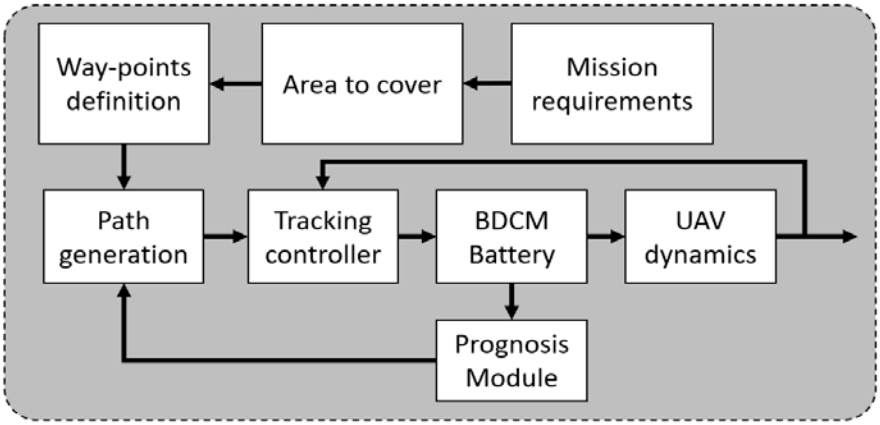

Figure 5.1: Structure of mission planning based on Prognosis module for flight Endurance estimation.

In Figure 5.1, the proposed mission planning strategy is shown. At top level, the main elements necessary for roadmap generation according to mission requirements are established. The *mission requirements* define the flight characteristics according to application e.g. the maximum and minimum flight height, the distance to cover, the minimum energy and the flight speed. *Area to cover* encompass the limits of the region to overfly, and usually it must match with the maximum distance defined in mission requirements. Likewise, the area to cover allows to establish a safe flying area which limits the flight distance and guarantee that the mission will be performed inside of initial requirements. The *Way-points definition* stage establishes the reference points inside of area to cover. They are also necessary to generates the different paths that describe the complete trajectory of the mission.

At the middle level in Figure 5.1, the *Path generation* determines the routs around $x - y - z$ axis that vehicle has to track by means a position and orientation controller. In addition, other references can be defined as the orientation around the yaw angle. Finally, at the bottom level the *Prognosis Module* estimates during the mission the flight endurance by estimate the battery State of Charge considering the current and voltage measurement. In following sections the interactions of the different stages integrating the mission strategy will be explained.

Remark. In this work, the mission planning strategy is focused into execute missions where the hexarotor has to follows long time and distance paths along x-y-z position without aggressive movements. In that sense, the mission requirements are mainly constrained to stop-and-go motion, i.e. the initial and final speed and acceleration of the vehicle could be equal to zero between initial and final way-points. Such mission are mainly associated to agricultural applications (to see Figure 5.2) where the multirotor performs crop management tasks, e.g. irrigation, pesticide application, regular monitoring of farms as crop growth, preparation of yield maps and soil fertility based on aerial photos and GPS guidance.

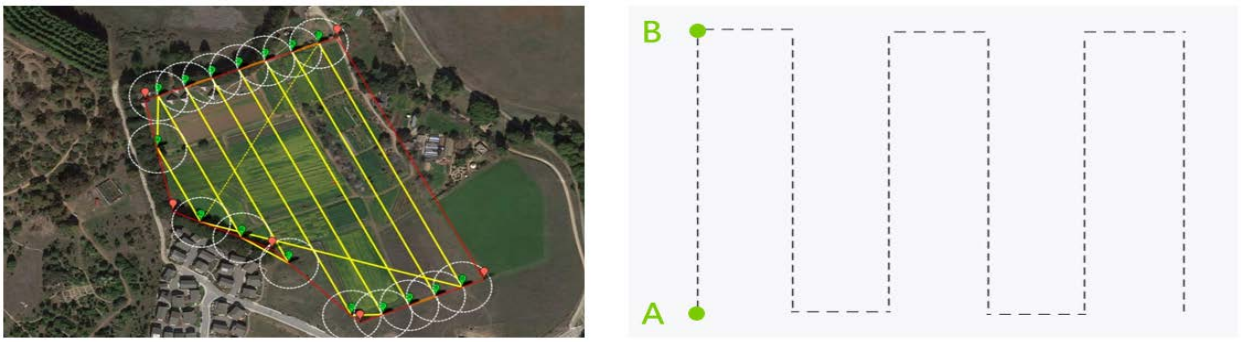

Figure 5.2: Example of crop irrigation path for multirotors.

5.1.1 Energy consumption of hexarotor

Such as was introduced in Chapter 3, the hexarotor is a multirotor vehicle powered by Li-Po battery. The Li-Po battery supplies the enough energy to take-off, flight around a path described by n way-points and finally landing to fulfill a particular mission. The flight capabilities such as movement around x-y plane whiles keeping a constant altitude as well as the flight endurance (FE) depends on the energy that battery is able to supply to BLDCMs to generate the desired thrust and torques. In that sense, is it necessary to define the energy that the battery can supply and the energy that hexarotor requires to launch a mission.

Battery energy

Long time-distance flights require that battery possess high storage capabilities and large C-rate to ensure the fulfillment of a mission and powered the BLDCMs according to demanded current. According to ([137, 138]), the energy (in Wh) that a Li-Po battery can supply is computed as

$$E_b \approx n_s \cdot n_p \cdot C_0 \cdot V_{nom}, \tag{5.1}$$

where C_0 is the nominal battery capacity at its Begin-of-Life (BoL) and V_{nom} is the nominal battery cell voltage, n_s and n_p represent the number of cells in parallel and series connection of the battery. When the battery is fully charged or discharged, the maximum and minimum energy that battery can supply is easily deducted, e.g. considering the operational voltage range of Li-Po battery described in Chapter 3 (subsection 3.3.1), is $\approx$ 16.8 V (4.2 V per cell) as maximum and $\approx$ 10.8 V (2.7 V per cell) as minimum (considering that the battery is composed by four cells in series connection) and the nominal capacity is 6.2 Ah. Then the energy range is defined as $E_b \in [67\ , 105]$ Wh. In addition, note that battery total energy is not a function of discharge range. However equation is useful to determines the maximum energy consumption according to battery characteristics before to launch the mission.

Energy consumption by hexarotor

The energy provided by the battery is consumed entirely by the BrushLess DC motor and ESC. In that sense, the total energy consumption from initial time t_0 to final time t_f can be computed as ([114, 180]):

$$E_c = \int_{t_0}^{t_f} [V_{batt} \cdot I_{batt}]dt = \int_{t_0}^{t_f} \sum_{m=1}^{N_m} [V_m \cdot I_m]dt, \tag{5.2}$$

where V_{batt} and I_{batt} are the battery voltage and the total current demanded by the BLDCMs. V_m and I_m are the voltage and current of each the BLDCM where $m \in [1, \cdots, N_m]$. N_m is the number of mth BLDCM in the hexarotor. Then, by considering the mathematical model of BLDCM

$$\begin{aligned} \bar{v}_{batt_i} &= R\bar{i}_{batt_i} + K_E\omega_i, \\ \dot{\omega}_i &= \frac{1}{J_m}(K_E\bar{i}_{batt_i} - d\omega^2 - D_f\omega_i - T_{fric}) \\ \bar{v}_{batt_i} &= V_{batt} \cdot Dc_i \\ I_{BLDCM_i} &= \bar{i}_{batt_i} \cdot Dc_i, \end{aligned} \tag{5.3}$$

and substituting equation (5.3) in (5.2), the relationship between the energy consumption and angular speed of the BLDCMs can be established as:

$$E_c = \int_{t_0}^{t_f} \sum_{m=1}^{N_m} [\kappa_1 + \kappa_2\omega_m + \kappa_3\omega_m^2 + \kappa_4\omega_m^3 + \kappa_5\omega_m^4 + \kappa_6\dot{\omega}_m + \kappa_7\dot{\omega}_m^2 + \kappa_8\omega_m\dot{\omega}_m + \kappa_9\omega_m^2\dot{\omega}_m]dt, \tag{5.4}$$

where the constants $\kappa_1, \cdots, \kappa_9$ are combinations of the BLDCMs parameters defined as

$$\begin{aligned} \kappa_1 &= \frac{RT_f^2}{K_E^2} & \kappa_2 &= \frac{T_{fric}}{K_E}\left(\frac{2RD_f}{K_E} + K_E\right) \\ \kappa_3 &= \frac{D_f}{K_E}\left(\frac{RD_f}{K_E} + K_E\right) + \frac{2RT_{fric}d}{K_E^2} & \kappa_4 &= \frac{d}{K_E}\left(\frac{2RD_f}{K_E} + K_E\right) \\ \kappa_5 &= \frac{Rd^2}{K_E^2} & \kappa_6 &= \frac{2RJ_mT_{fric}}{K_E^2} \\ \kappa_7 &= \frac{RJ_m^2}{K_E^2} & \kappa_8 &= \left(\frac{2RJ_m^3d}{K_E^2} + J_m\right) \\ \kappa_9 &= \frac{2RJ_m^2d}{K_E^2} \end{aligned} \tag{5.5}$$

and ω_m and $\dot{\omega}_m$ are the speed and angular acceleration of the mth BLDCM. In addition, by considering that the initial and final speed are equals i.e. $\omega_0 = \omega_f$, (5.4) can be simplified as:

$$E_c = \int_{t_0}^{t_f} \sum_{m=1}^{N_m} [\kappa_1 + \kappa_2\omega_m + \kappa_3\omega_m^2 + \kappa_4\omega_m^3 + \kappa_5\omega_m^4 + \kappa_6\dot{\omega}_m^2]dt. \tag{5.6}$$

Remark. Note that, the energy consumption by hexarotor (E_c) must match with battery energy (E_b) in order to ensure the mission fulfillment. However E_b is given in Wh whiles E_c is given in Joules, in that sense, it is necessary to express E_c in Wh.

In addition (5.6) describes the energy consumption for stop-and-go motion during the flight whiles (5.4) describes continuous motion. Such flight characteristics will be explained in the following subsections.

5.1.2 Path generation based on energy consumption

The core of the proposed mission planning strategy is the path generation considering the energy consumption during the flight. In that sense, it is necessary to establish a methodology able to establish a relationship between the hexarotor motion and the consumed energy in order to meet the mission requirements and guarantee the fulfillment of the mission.

The path generation is defined considering two important aspects: (i) to guarantee the generation of smooth paths, i.e. the position and orientation vary smoothly with the time avoiding aggressive maneuvers ([37]), and (ii) the maximization of flight endurance, i.e. the increase of the final flight time t_f. A

smooth path could be associated to the system control inputs e.g. a smooth evolution of the angular motor speed, and on the other hand, the maximization of flight endurance can be achieved by minimize the energy consumption during the flight. In addition, the minimization of energy consumption leads to extend the time and distance that vehicle can navigate during the mission execution.

In this work, two methods for path generation are considered: 1) path planning based on polynomial approach and 2) optimal path planning based on a minimization energy criteria. Such path generation methods lead to produce smooth and minimum energy paths, however the path definition via polynomial functions does not take into account the dynamics of hexarotor whiles the path definition by minimization of energy criteria considers the hexarotor dynamics and constraints associated to vehicle motion. In the following subsections, the main characteristics and properties of both methods will be explained.

Path definition based on polynomial approach

Polynomial functions are suitable for generating paths due to their properties such as smoothness and boundary conditions ([37, 86]). A polynomial function of order n is defined as:

$$p(t) = \sum_{i=0}^{n} \gamma_i t^i = \gamma_0 + \gamma_1 t + \cdots + \gamma_n t^n, \tag{5.7}$$

where γ_i are the coefficients of polynomial and t is the time. The order determines the number of derivatives that must be resolved, i.e. for $n = 3$ leads to minimum position and velocity path, and for $n = 5$ leads to smoother and minimum energy paths ([86]). Then, by considering a quintic (fifth-order) polynomial function as

$$p(t) = \gamma_0 + \gamma_1 t + \gamma_2 t^2 + \gamma_3 t^3 + \gamma_4 t^4 + \gamma_5 t^5, \tag{5.8}$$

where time $t \in [0, T]$. The first and second derivatives are also smooth polynomials

$$\begin{aligned} \dot{p}(t) &= \gamma_1 + 2\gamma_2 t + 3\gamma_3 t^2 + 4\gamma_4 t^3 + 5\gamma_5 t^4 \\ \ddot{p}(t) &= 2\gamma_2 + 6\gamma_3 t + 12\gamma_4 t^2 + 20\gamma_5 t^3. \end{aligned} \tag{5.9}$$

The trajectory p has defined boundary conditions for position, velocity and acceleration according to Table 5.1 and commonly the velocity and acceleration boundary conditions are all zero.

Time	p	$\dot{p}$	$\ddot{p}$
$t = 0$	p_0	$\dot{p}_0$	$\ddot{p}_0$
$t = T$	p_T	$\dot{p}_T$	$\ddot{p}_T$

Table 5.1: Boundary conditions of trajectory

Then, by writing (5.8) and (5.9) for the boundary $t = 0$ and $t = T$ gives six equations which can be written in matrix form as

$$\begin{bmatrix} p_0 \\ p_T \\ \dot{p}_0 \\ \dot{p}_T \\ \ddot{p}_0 \\ \ddot{p}_T \end{bmatrix} = \begin{bmatrix} 1 & 0 & 0 & 0 & 0 & 0 \\ 1 & T & T^2 & T^3 & T^4 & T^5 \\ 0 & 1 & 0 & 0 & 0 & 0 \\ 0 & 1 & 2T & 3T^2 & 4T^3 & 5T^4 \\ 0 & 0 & 2 & 0 & 0 & 0 \\ 0 & 0 & 2 & 6T & 12T^2 & 20T^3 \end{bmatrix} \begin{bmatrix} \gamma_0 \\ \gamma_1 \\ \gamma_2 \\ \gamma_3 \\ \gamma_4 \\ \gamma_5 \end{bmatrix}. \tag{5.10}$$

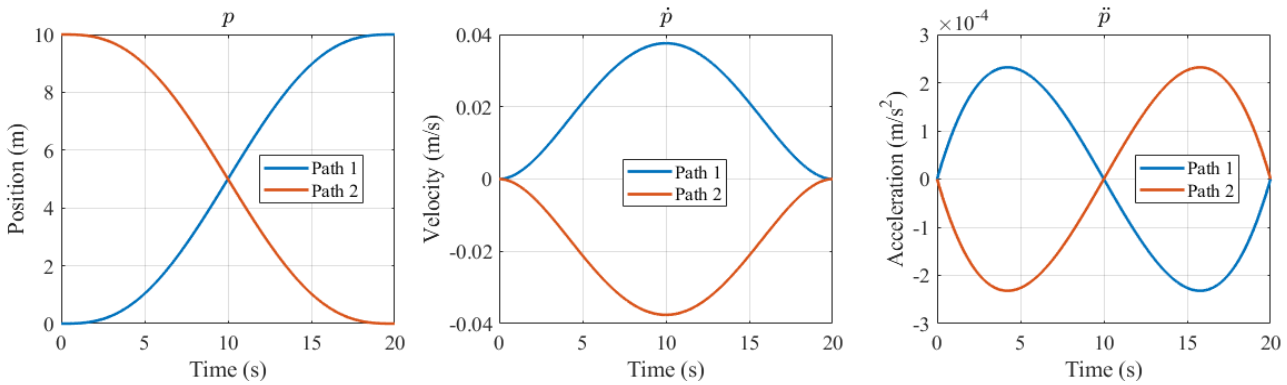

Figure 5.3: Example of path generation with polynomial function.

In Figure 5.3, the example of a path generated by a polynomial function is shown. As it can be observed, the path exhibits a smooth behavior from initial point to final point and the maximum velocity is reached at middle of the path considering a initial and final velocity equals to zero. In addition, the previous solution is able to generate smooth one-dimensional paths. In the case of multirotors, they have more than one axis of motion or freedom degrees. In that sense, the motion can be written in vector form as $p \in \mathbb{R}^N$, where N is the number of freedom degrees. An hexarotor has a position (x, y, z) and orientation (ϕ, θ, ψ). In this work the orientation is generated by position change, i.e. roll angle depends on any change in the position on the x y-axis $\psi(y)$ and pitch angle depends on any change in the position on the x-axis $\theta(x)$ (such relationship was established in Chapter 4 in subsection 3.4.1).

In this work, the mission that hexarotor must develop requires the vehicle to move smoothly along a path through one or more intermediate way-points considering two cases: 1) stop-and-go motion or 2) continuous motion. In that sense, hexarotor has to track a piecewise continuous path. Such problem is formalized considering that the path is defined by $\mathbb{M}$ positions p_k (also called way-points), $k \in [1, \mathbb{M}]$ and there are $\mathbb{M}$-1 motion segments. $p_k \in \mathbb{R}^N$ is a vector representing the position.

The hexarotor starts in p_1 at rest and finishes at p_M at rest, but it also moves through (or close to) intermediate configurations without stopping. The problem is over constrained and to attain continuous velocity we surrender the ability to reach each intermediate position. In 1-dimensional cases described in Figure 5.4, the motion comprises linear motion segments with polynomial blends where a 5^{th} order polynomial is considered because it is able to match boundary conditions on position, velocity and acceleration for starting and final points.
In Figure 5.4, the first segment of the path accelerates from the initial position p_1 with zero initial velocity, and it joins to the line heading toward the second configuration p_2. The blend time is set to be a constant denoted by the acceleration time t_{acc} and $t_{acc}/2$ before reaching p_2 the path executes a polynomial blend with a duration of t_{acc} onto the line from p_2 to p_3 and the process repeats. The constant velocity $\dot{p}_k$ can be specified for each segment. The average acceleration during the blend is defined as

$$\ddot{p}(t) = \frac{\dot{p}_{k+1} - \dot{p}_k}{t_{acc}}. \tag{5.11}$$

If the maximum acceleration capability of the axis is known then the minimum blend time can be computed. According to ([37]), in a particular motion segment each axis will have a different distance to travel and traveling at its maximum velocity, there will be a minimum time before it can reach its goal. The first step in planning a path is to determine which axis will be the slowest to compute the segment, based on the distance that each axis needs to travel for the segment and its maximum achievable velocity. For this, the

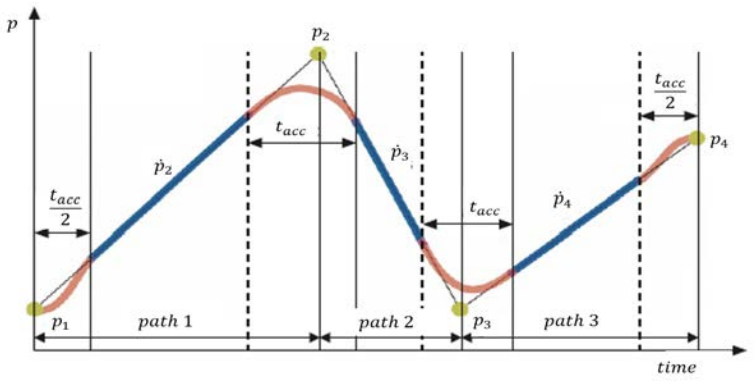

Figure 5.4: Example of multi-segment path ([37])

.

duration of each segment can be computed and then the required velocity of each x-y-z axis position. This ensures that all axes reach the next position at the same time. The comparison between an stop-and-go and continuous motion is presented in Figure 5.5 with a path considering different way-points.

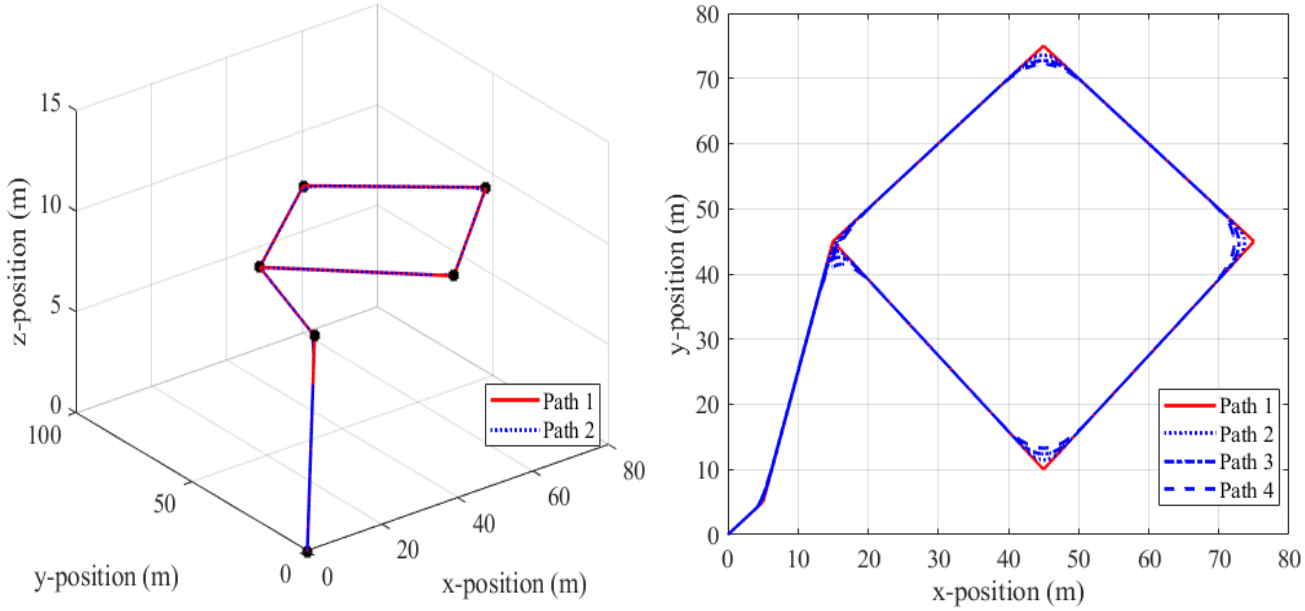

(a) (b)

Figure 5.5: (a) Example of path in 3D. (b) Path in x-y plane.

Remark. As it can be noted in this method, the path generation does not take into account the hexarotor dynamics. In addition, the main assumption considered in this method is that both hexarotor position and orientation are properly controlled and the polynomial function provides the reference for x-y-z axis. In addition, the minimization of energy consumption will depend on the flight velocity between way-points as well as the time and distance from initial to final point considering in the mission as well as the battery health.

The paths shown in Figure 5.5 are applied to hexarotor considering both stop-and-go and continuous motion, in order to demonstrate the capabilities of this method to generate smooth and minimum energy

paths according to mission requirements. The paths shown in Figure 5.5 are used as reference that hexarotor has to track for x-y-z position and the yaw angle is kept constant at 0 rad. The energy consumption for both stop-and-go and continuous motion is computed considering the equations (5.4) and (5.6). The battery response and energy consumed are shown in Figure 5.6 and 5.7 for both cases. As it can be observed in Figure 5.6, the Stop-and-go motion (Path 1 black line) has "abrupt" changes during the take-off as well as during position change in comparison with continuous motion (Path 2 red line). However, for both cases, the energy consumption for hexarotor is 160 kJ or 45 Wh. This is due to two factors:

1. during the position change in Path 1, the hexarotor has a decrease in the current generated for all BLDCM after take-off and during the landing and the final time is constrained at 10 minutes, and

2. although the acceleration time (t_{acc}) was established at different values in each path, the continuous paths are not able to pass through each way-point.

From here, it is possible to focus only in stop-and-go motion paths for mission planning strategy considering to generate smooth and minimum energy paths as well as to ensure that vehicle flies through each way-point according to roadmap definition.

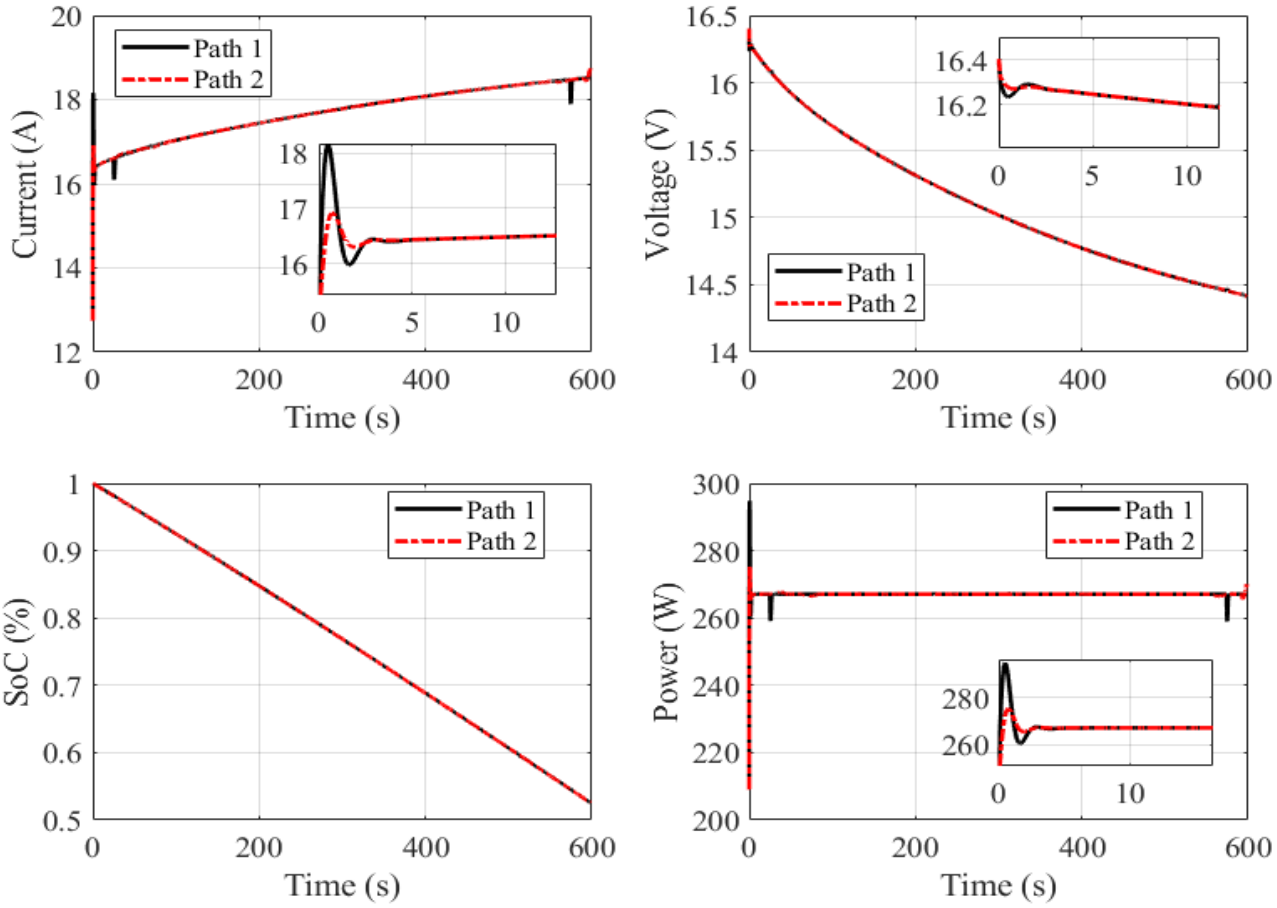

Figure 5.6: Compassion of battery response between Stop-and-go and Continuous motion.

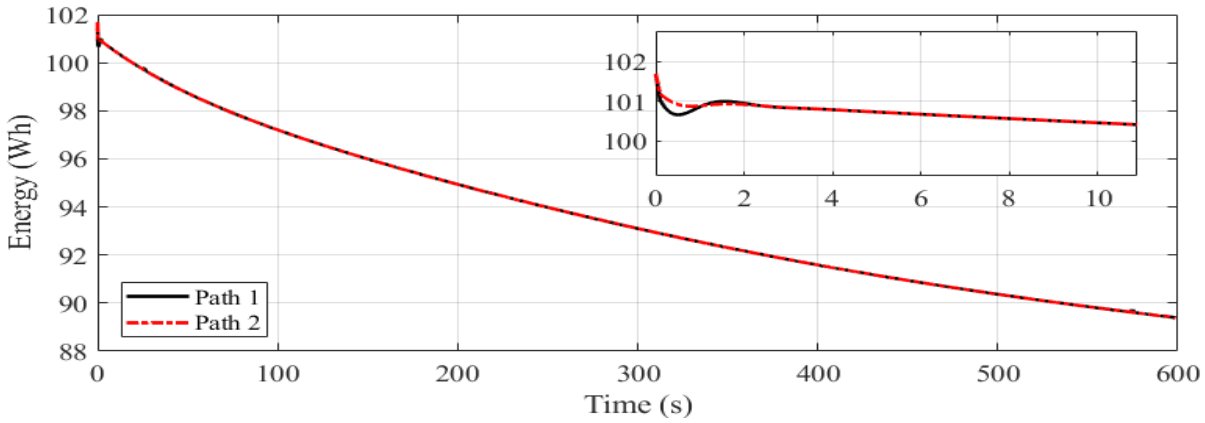

Figure 5.7: Energy battery

.

Path definition based on minimization energy criteria

Such as was mentioned in previous section, the path definition based on polynomial functions does not take into account the hexarotor dynamics nor the battery health during its formulation. In addition, the main assumption in this method is that the generated path is characterized by being smooth and minimum energy path. However, it is necessary to established the relationship between the minimization of energy consumption associated to angular speed of each BLDCM and position around x-y-z axis. The minimization of the energy consumption (5.6) is realized by defining a multi-objective constrained minimization problem taking into account the hexarotor dynamics and the constraints associated with the battery performance. In order to explain how is defined the minimization problem, let us consider Figure 5.8-(a), where the interaction of the different elements that integrate the dynamics of the hexarotor is shown. The control signals are functions of control inputs generated by CCL described in Chapter 3 and reference angular speeds of each BLDCM. Then, in order to established the relationship between energy consumption and control effort, an additional control input (ω_o^2) is introduced as a reference control input in the CCL as it can be seen in Figure 5.8-(b).

Considering the approach proposed in ([114]), the path planning definition is formulated as a minimization problem of the total energy consumed from initial and final times $[t_0\ t_f]$. Then, taking into account the dynamic of the hexarotor and the propulsion system, the following nonlinear state space system is defined:

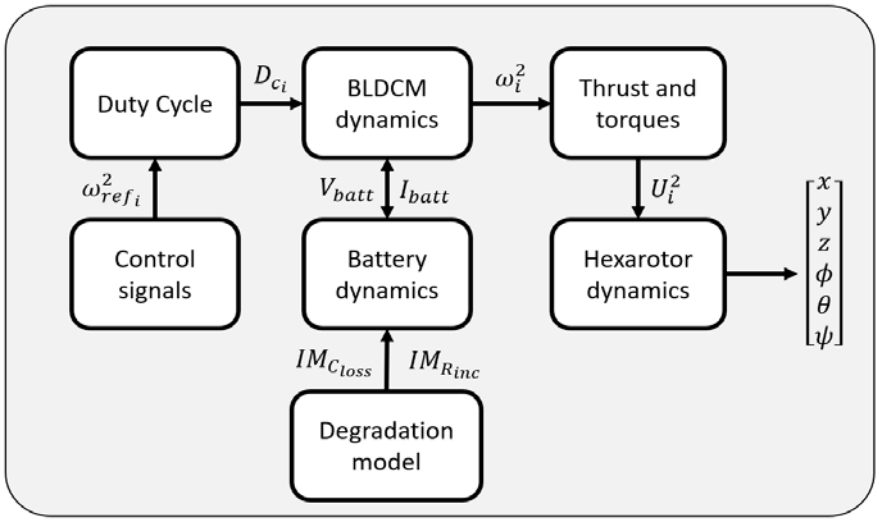

(a)

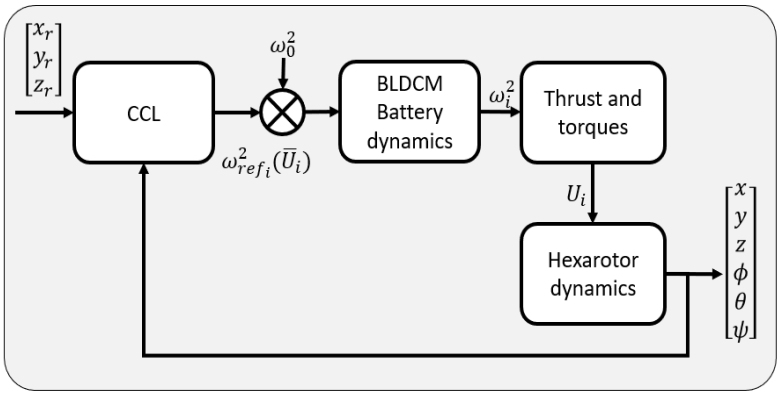

(b)

Figure 5.8: (a) Interaction of different dynamics in hexarotor. (b) Control system with reference angular speed

$$
\begin{aligned}
\dot{x}_1 &= x_2 \\
\dot{x}_2 &= \left(\mathbf{c}x_7\mathbf{s}x_9\mathbf{c}x_{11} + \mathbf{s}x_7\mathbf{s}x_{11}\right)\frac{U_1}{m} \\
\dot{x}_3 &= x_4 \\
\dot{x}_4 &= \left(\mathbf{c}x_7\mathbf{s}x_9\mathbf{s}x_{11} + \mathbf{s}x_7\mathbf{c}x_{11}\right)\frac{U_1}{m} \\
\dot{x}_5 &= x_6 \\
\dot{x}_6 &= -g + \left(\mathbf{c}x_7\mathbf{c}x_9\theta\right)\frac{U_1}{m} \\
\dot{x}_7 &= x_8 \\
\dot{x}_8 &= \frac{I_y - I_z}{I_x}x_{10}x_{12} + \frac{J_m}{I_x}\omega_T x_{10} + \frac{U_2}{I_x} \\
\dot{x}_9 &= x_{10} \\
\dot{x}_{10} &= \frac{I_z - I_x}{I_y}x_8x_{12} - \frac{J_m}{I_y}\omega_T x_8\frac{U_3}{I_y} \\
\dot{x}_{11} &= x_{12} \\
\dot{x}_{12} &= \frac{I_x - I_y}{}x_8x_{10} + \frac{U_4}{}
\end{aligned}
$$

where $x = [x\,\dot{x}\,z\,y\,\dot{y}\,z\,\dot{z}\,\phi\,\dot{\phi}\,\theta\,\dot{\theta}\,\psi\,\dot{\psi}\,\omega_{i_{1\times 6}}\,V_{SoC}\,V_d\,\omega_{i_{ref\,1\times 6}}]^\top$ is the state vector, $\dot{\omega}_{i_{ref}}$ is de control input and it corresponds to the angular acceleration of *ith*-BLDCM. Considering the control input, the *ith* duty cycle Dc_i is computed as

$$Dc_i = \gamma_1 x_j^2 + \gamma_2 x_j + \gamma_3 \tag{5.13}$$

where $i = 1, \cdots, 6$ and $j = 21, \cdots, 26$. The demanded current I_i of *ith*-BLDCM is computed as:

$$I_i = \frac{Dc_i}{K_E}\left(J_m \dot{\omega}_{i_{ref}} + dx_j^2 + D_f x_j + T_{fric}\right) \tag{5.14}$$

where $i = 1, \cdots, 6$ and $j = 21, \cdots, 26$. Finally the total demanded current I_{batt} and battery voltage V_{batt} are computed as:

$$\begin{aligned} I_{batt} &= \sum_{i=1}^{6} I_i \\ V_{batt} &= V_{OCV}(x_{19}) - x_{20} - R_{int} I_{batt}. \end{aligned} \tag{5.15}$$

Considering the dynamic system (5.12) and the equations (5.13)-(5.15), the minimization problem of energy consumption is defined as:

$$\begin{aligned} \underset{\dot{\omega}_{i_{ref}}}{\textbf{min}} \quad & E_c(t_f) \\ \textbf{s.t.} \quad & \text{dynamic system (3.13)}, \\ & x(t_0) = x_{t_0},\, x(t_f) = x_{t_f}, \\ & x_{min} \le x \le x_{max}, \\ & 0 \le x_j \le \omega_{max},\ j = 21, \cdots, 26 \\ & V_{batt}(EoD) \le V_{batt} \le V_{batt}(t_0), \\ & SoC(t_f) \le SoC \le SoC(t_0), \end{aligned} \tag{5.16}$$

where the reference angular velocity and the battery voltage are bounded considering realistic operational limits, and the constraint in the battery voltage avoids to discharge the battery under Safety Voltage Threshold (SVT).

Remark. As it can be noted in this method, the path generation is reached by solving the minimization problem (5.16). The boundary conditions around the states of hexarotor dynamics, mainly position (x,y,z) lead to generate the path which has the characteristic to be a minimum energy path due that the solution is constrained to minimize the control effort associated to angular speed of BLDCM.

In order to show and compare the differences between the path definition based on polynomial functions and multi-objective constrained minimization problem, the hexarotor is required to follow a single path from initial point to final point considering Stop and go motion. The multi-objective constrained minimization problem (5.16) was solved using an optimal control software called GPOPS II which is a general-control software implemented in MATLAB®. It is dedicated to solve nonlinear optimal control problems using variable-order adaptive orthogonal collocation methods together with sparse nonlinear programming ([132]). In order to test the capability of the path planning algorithm to minimize the energy consumption E_c, two cases with the following boundary conditions were considered:

$$
\begin{aligned}
X_a(t_0) &= [0_{1\times 12},\ 454.7_{1\times 6},\ 1,\ 0,\ 25]\,, \\
X_a(t_f) &= [x_f,\ 0,\ y_f,\ 0,\ z_f,\ 0_{1\times 5},\ \psi_f,\ 0,\ 454.7_{1\times 6},\ free,\ free,\ free]\,.
\end{aligned}
\tag{5.17}
$$

The BLDCM speed was established as $\omega_i(t_0) = \omega_r(t_f) = 454.7\,\text{rad/s}$ due to such value corresponds to equilibrium conditions for hexarotor hover position. Moreover, that initial speed makes it possible to generate the thrust force to take-off and remain lifted up during the flight. On the other hand, the multi-objective constrained minimization problem was also solved allowing to choose the final time according to minimum energy. In order to do that, a time window was established, where the minimum time is 5 sec and maximum time was 15 sec.

Case 1. In the first case, the multi-objective constrained minimization problem (5.16) was solved considering a new ($SoH = 1$) and fully charged ($SoC = 1$) battery, $EoD = 12.8$ V. In Figure 5.9 and Figure 5.10 the comparison between the minimum energy path generated by solving the minimization problem and the path generated by the polynomial approach is shown. As it can be seen, both methods generate similar smooth paths without aggressive maneuvers. However the difference between both methods can be observed in Figure 5.11, where the minimization problem generate a very smooth transition between the initial and final orientation.

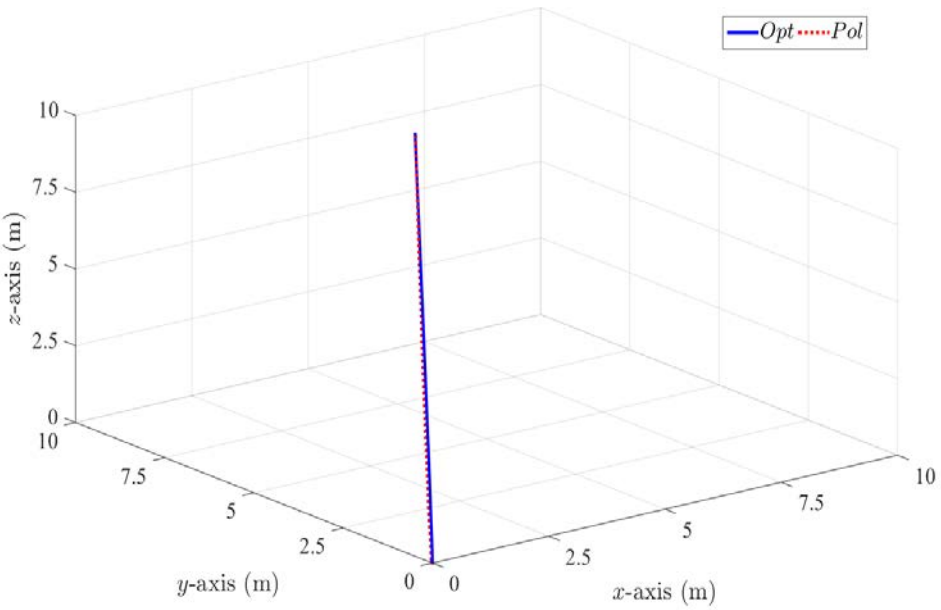

Figure 5.9: Case 1: 3D Position around $x - y - z$ axis.

The battery response is shown in Figure 5.12 and 5.13. As it can been seen the demanded current for the minimization problem has an increase due to take off in comparison with the polynomial approach. This increase generates a considerable drop in battery voltage during takeoff (Figure 5.12-b). The total consumed energy for the minimization problem and polynomial approach was 1.8657 kJ and 1.8772 kJ respectively. This result lets us to conclude that the minimization problem is capable of generating minimum energy paths considering the constraints associated to hexarotor and propulsion system dynamics. On the other hand, even though the polynomial approach does not consider the hexarotor dynamics during path generation it allows to generate smooth and minimum energy paths.

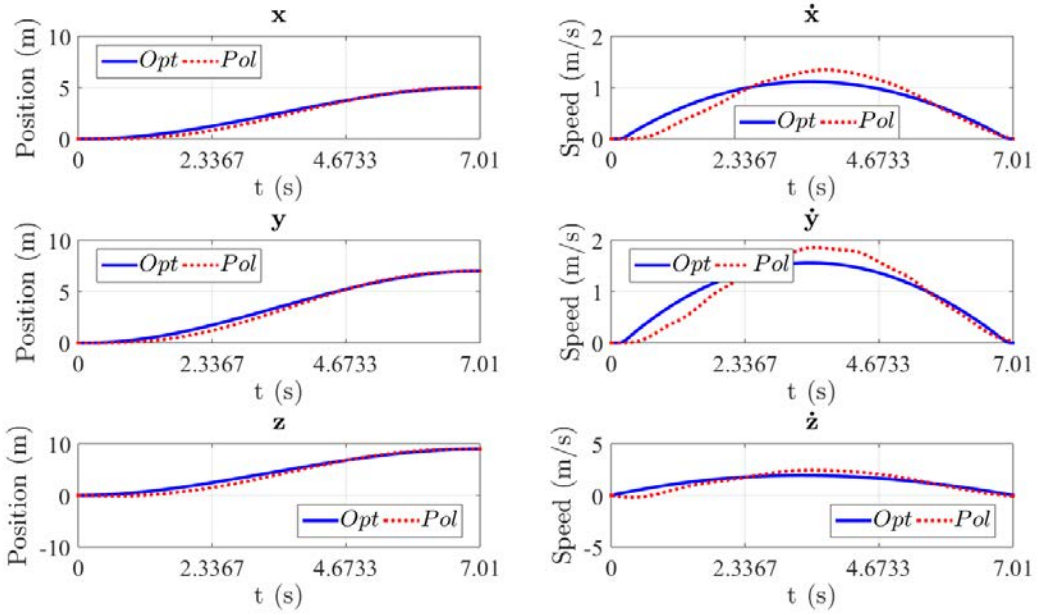

Figure 5.10: Case 1: Position and linear speed around $x - y - z$ axis.

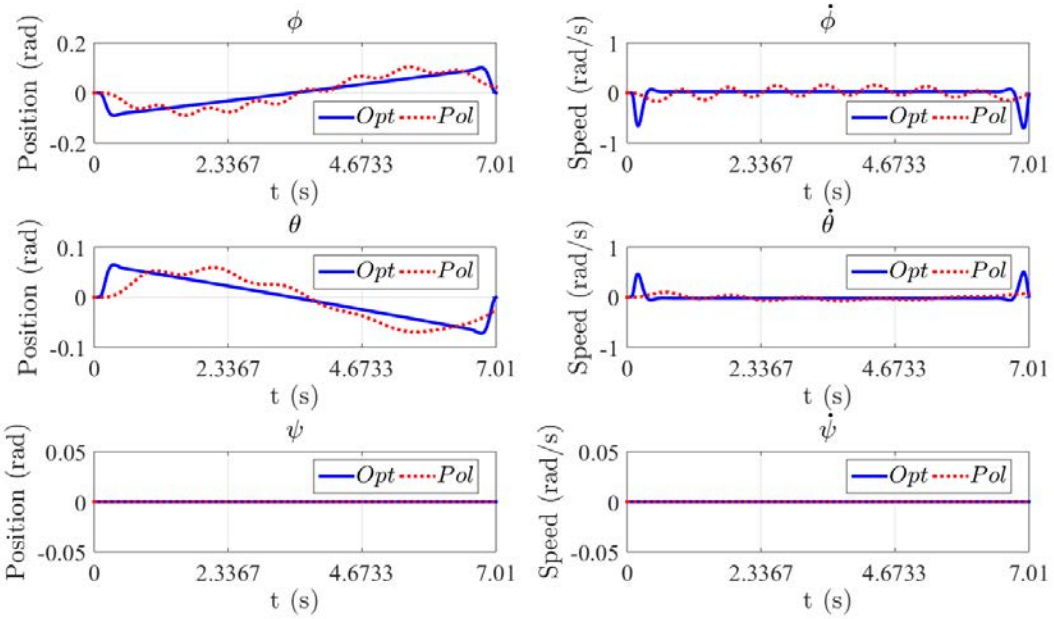

Figure 5.11: Case 1: Orientation and angular speed around Euler angles $[\phi\,\theta\,\psi]$.

Case 2. To evaluate the minimization problem (5.16) considering the effect of a degraded battery, two changes in the battery SoH were considered at the beginning of the flight taking into account the boundary conditions (5.17): $SoH = 0.8077$, i.e. a degradation of $\approx 20\%$ at $N_{cycle} = 60$, and $SoH = 0.5946$, i.e. a degradation of $\approx 40\%$ at $N_{cycle} = 160$. As it can be seen in Figure 5.14 and Figure 5.15, the variation

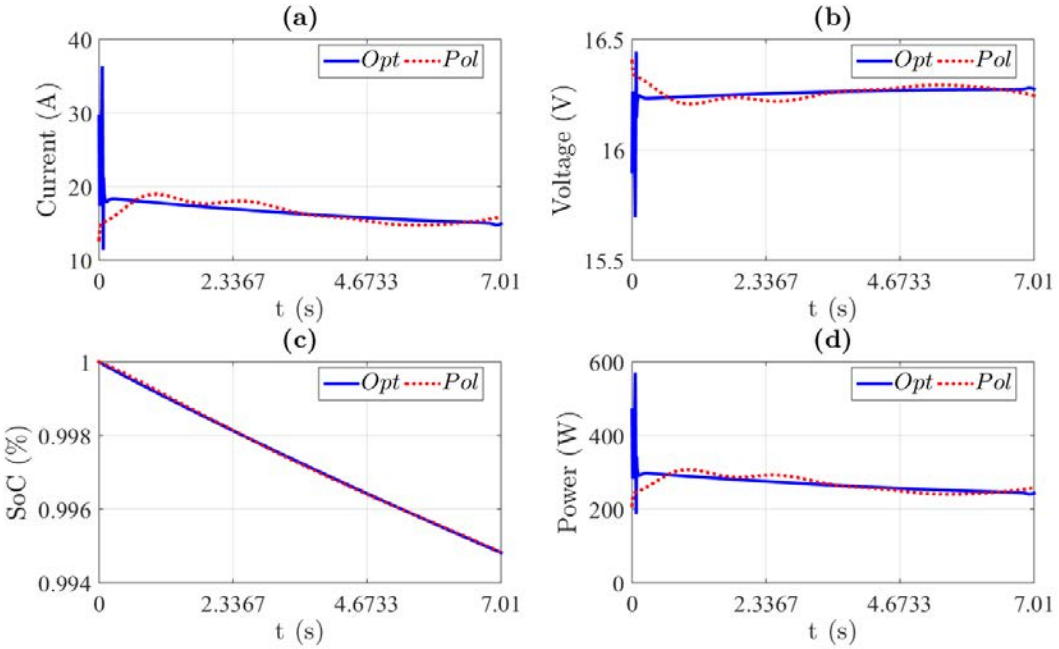

Figure 5.12: Case 1: Battery response.

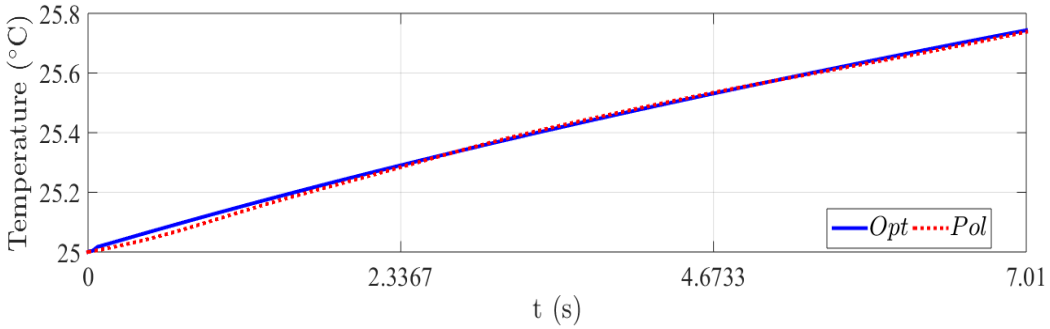

Figure 5.13: Case 1: Battery temperature.

of the SoH battery modifies the final time value associated with the hexarotor mission (to see Table 5.2). That means, the consideration of battery health in the minimization problem not only enables to manage the issues associated with battery performance, it also defines the limits of flight endurance in order to determine if the available energy is sufficient to continue developing the mission. It can also be noted that the SoH variations also affects the discharge dynamics. As it can be seen in Figure 5.16, to satisfy the requirement of minimum energy consumption and final time considering the performance index defined in (5.16), the discharge rate increase. On the other hand, it can be also notice that the initial SoC indicates that the battery is fully charged at the beginning of the flight, but due to capacity loss, final SoC tends to decrease rapidly.

Finally, the result of the minimization problem with SoH variation at 40% is compared with the response obtained by the polynomial approach in order to validate the result. As it is illustrated in Figure 5.17, the minimization problem is able to compensate for the effects generated by the variation in the battery SoH generating an energy consumption of 2.4035 kJ and 2.5341 kJ for the polynomial approach. In

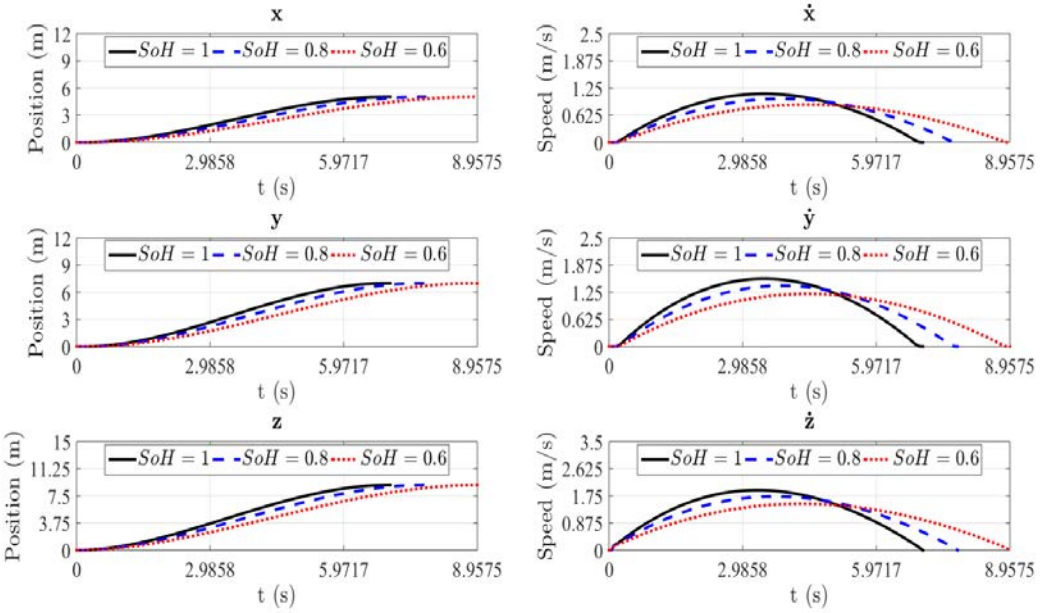

Figure 5.14: Case 2: Position and linear speed around $x - y - z$ axis.

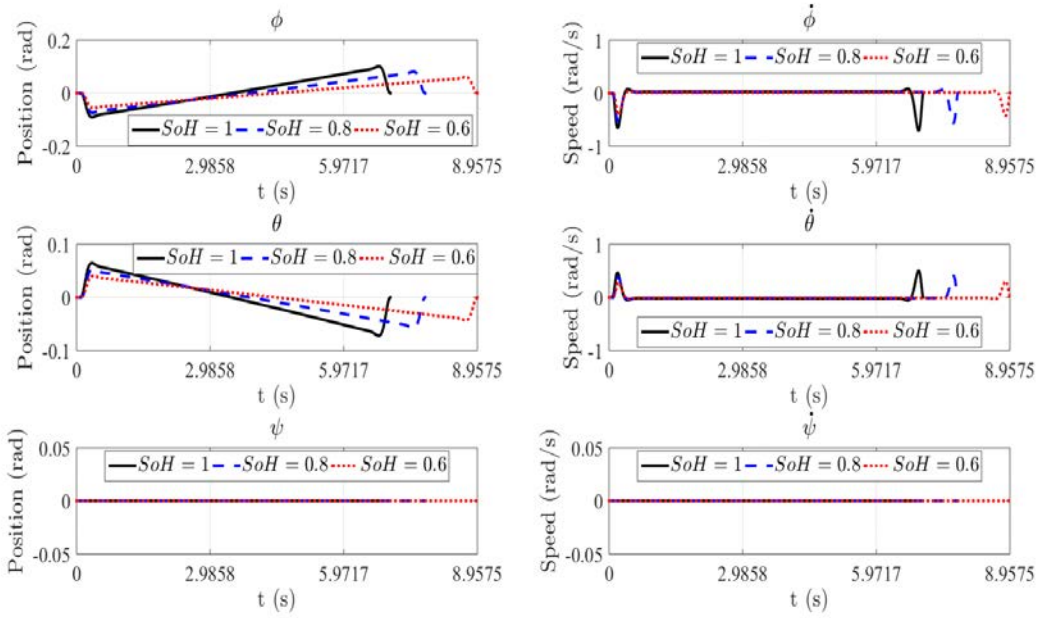

Figure 5.15: Case 2: Hexarotor position and linear speed around $x - y - z$ axis.

addition, it is possible to conclude that with this results, that the path generation by minimization of energy consumption is able to manage the effects of battery aging during the path generation, However it is important remark that the maximum time is established a priori considering the maximum energy that battery can supply. The polynomial approach on the other hand, requires to determine the maximum

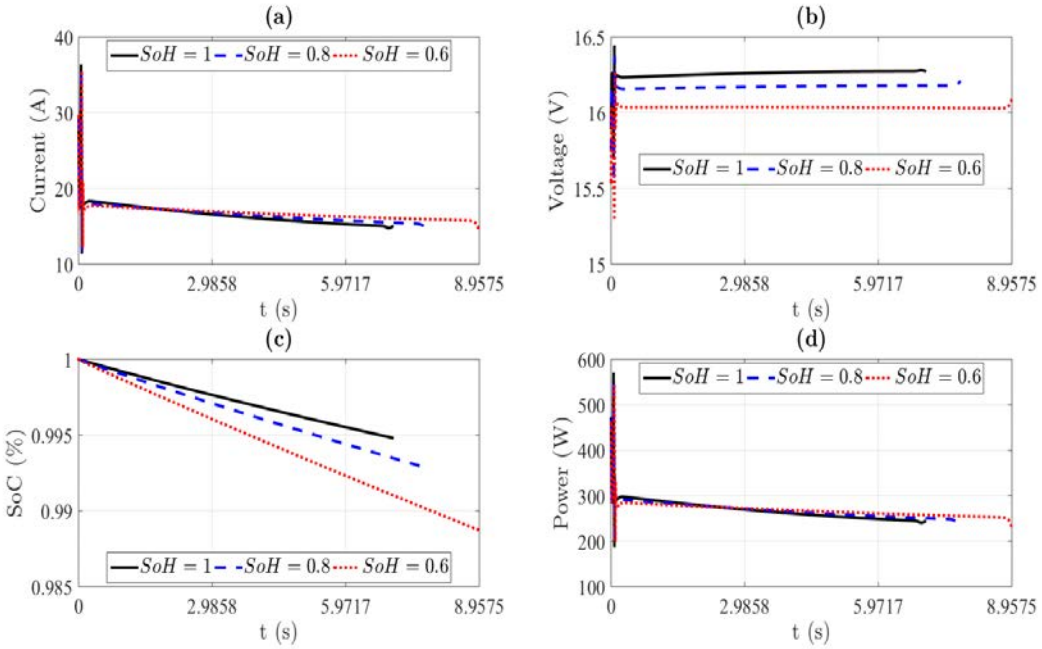

Figure 5.16: Case 2: Battery response.

Table 5.2: Results of multi-objective minimization problem with SoH variations.

t_f (s)	SoH (%)	N_{cycle}	$E_c(t_f)$ (kJ)
7.0147	100	0	1.8857
7.7908	80	60	2.0922
8.9575	60	160	2.4035

FE which is predicted by Prognosis algorithm proposed in Chapter 4. With such considerations, it is possible to fulfill the mission within the time window provided by Flight Endurance Model and battery characteristics.

5.2 Simulation results

Once the method to path definition and its relationship between path planing and Prognosis (through battery health or SoH) is defined, the following step is the integration of such elements in the mission planning strategy. Then considering the Figure 5.18, (already given in the introduction of this chapter), the mission requirements determines the flight characteristics, area to cover and way-points definition.
In order to illustrate how the mission planning strategy, an exploration task in an area of 12000 m^2 is established as mission target. Then the following mission characteristics are considering:

1. The initial (takeoff) and final point (landing) are the same.
2. The battery is new and fully charge (SoC and SoH are equals to 1).
3. A maximum time window for mission execution is considered at 15 minutes.

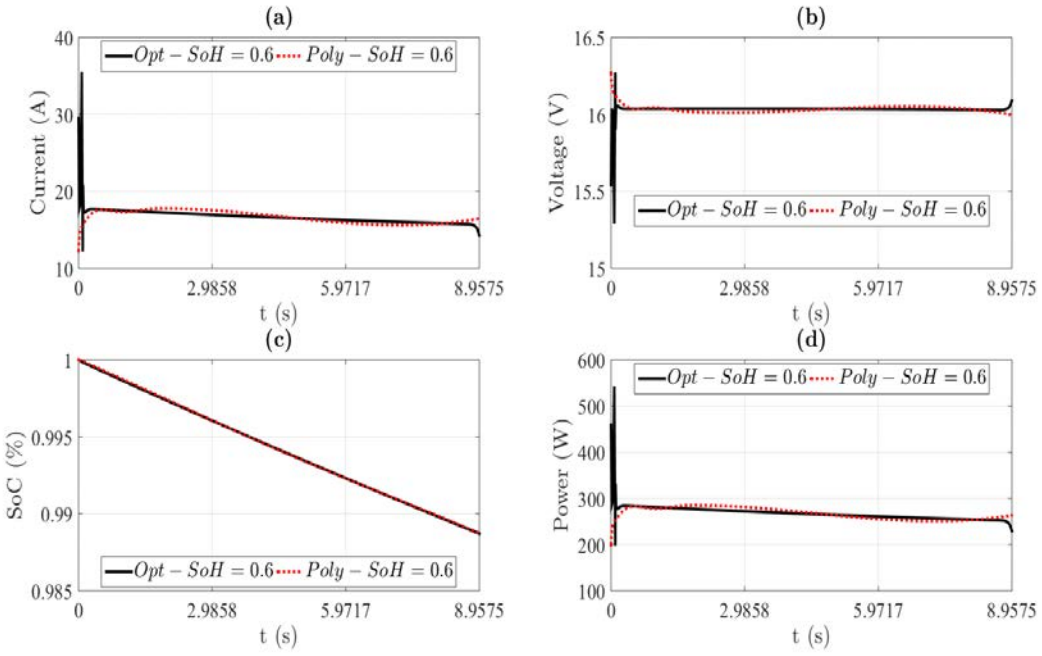

Figure 5.17: Comparison of battery response between minimization problem and polynomial approach.

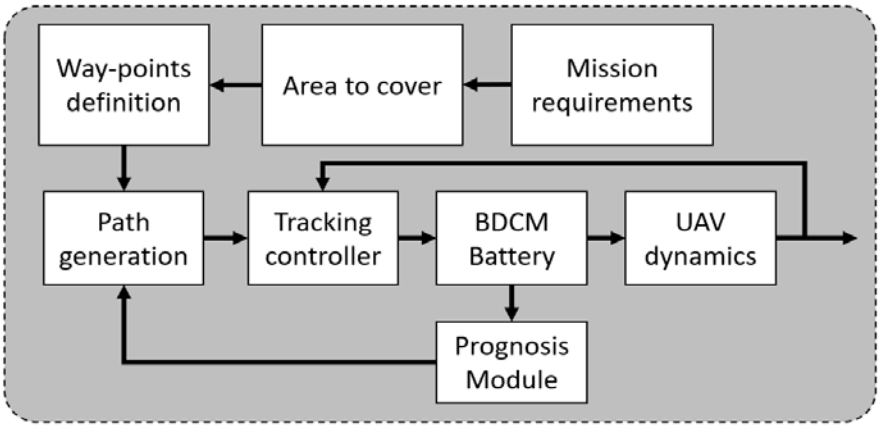

Figure 5.18: Structure of mission planning based on Prognosis module for flight Endurance estimation.

4. The area to cover comprise 8000 m^2 inside of a safety region which matching the total area of 12000 m^2.

5. The hexarotor motion is performed around x-y axis at constant altitude, i.e. there is not no variation around yaw angle.

6. The maximum flight speed is established at 10 m/s.

7. The EoD is defined at 20% of SoC according to Safety Voltage Threshold.

8. Without considering the initial and final way-points the hexarotor must move in 30 way-points around x-y position.

In Figure 5.19, the roadmap is shown were the blue point represents the take-off and landing way-point and the red ones are the reference way-points which defines the path that the hexarotor must track. The green arrows represent the direction of the path starting in the way-point (0,0,0).

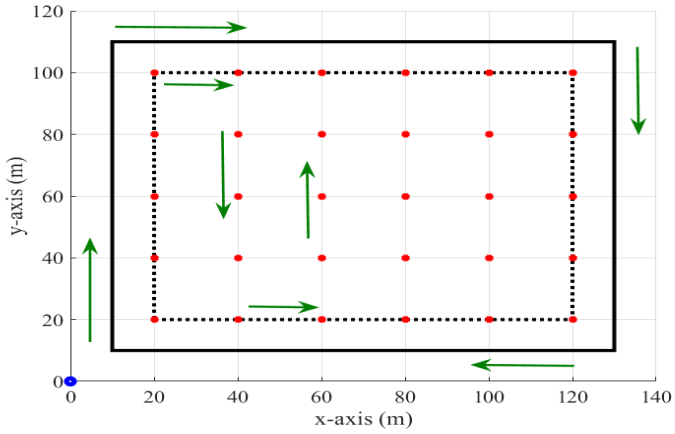

Figure 5.19: Area to cover and safety zone.

The maximum flight endurance is 23 min and 53 sec according to battery characteristics. The time interval between way-points is established at 20 sec. In that sense, by including the take-off and landing a final mission time of 640 sec or 10.65 minutes. In Figure 5.20 the entire path with the way-points in 3D view is shown.

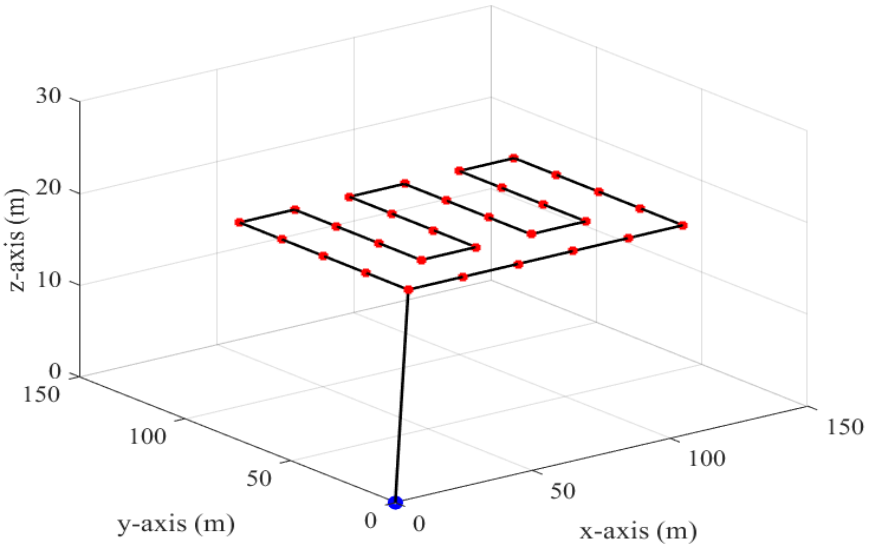

Figure 5.20: Minimum energy path and way-points.

In Figure 5.20 the result of the tracking controller in the hexarotor position is shown. As it can be observed the tracking controller keep the hexarotor position close to reference path to entire mission.
The battery response can be observed in Figure 5.22. The battery is considering new and fully charged and the maximum current picks are generated during the take-off and the landing. The rest of the picks

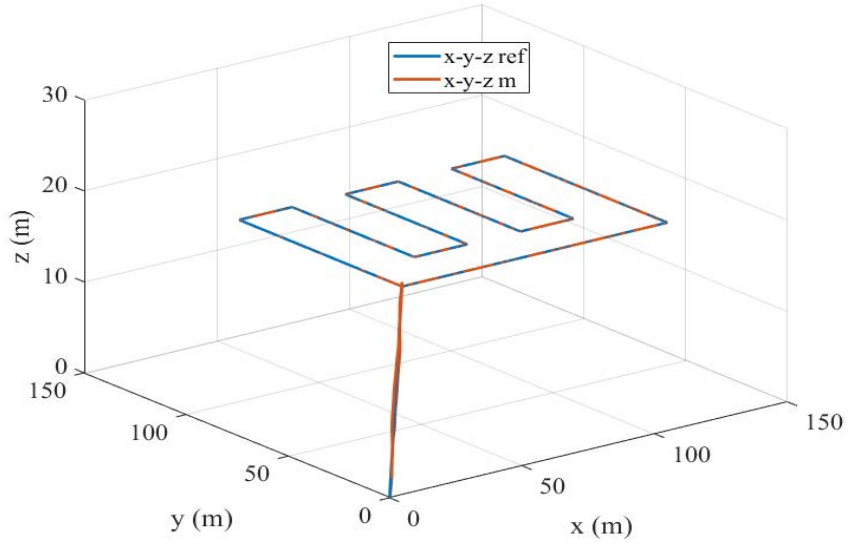

Figure 5.21: Results of the tracking controller.

just represents the position change between way-points due to the vehicle must move and stop. During the mission, the current tends to increase to compensate the effect of the voltage discharge and to generate the entire thrust force to keep the vehicle lift.

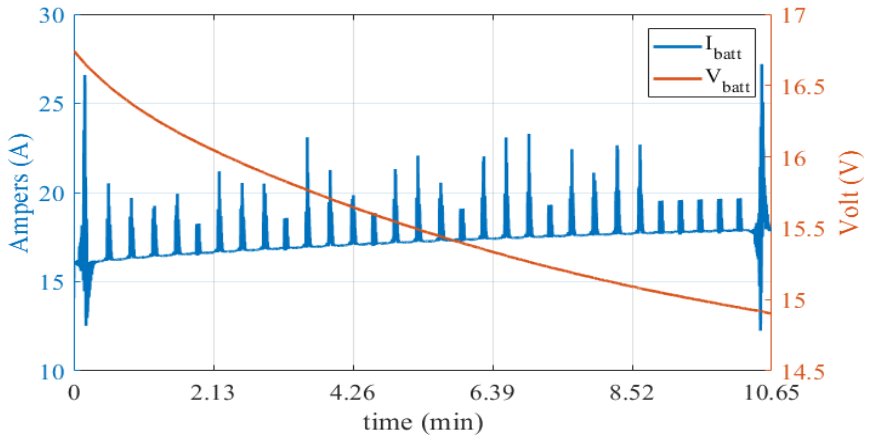

Figure 5.22: Battery response: current and voltage.

The current and voltage signal were contaminated with a noise level to evaluate the Prognosis Module. The result of the estimated SoC compared with the SoC generated by the battery model and scaled in 0-100 % is shown in Figure 5.23. As it can be noted, the estimated SoC relates the current and voltage (red line) reflecting the effective battery SoC in comparison with the SoC generates by the battery model (blue line) which just take into account the discharge current.
Finally, the computation of the Flight Endurance (FE) and Remaining Mission Time (RMT) is observed in Figure 5.24. First, the maximum FE was computed considering the model (4.8) and the parameters of the BLDCM and battery capacity. Then, using the Prognosis Module, the RMT is computed during the

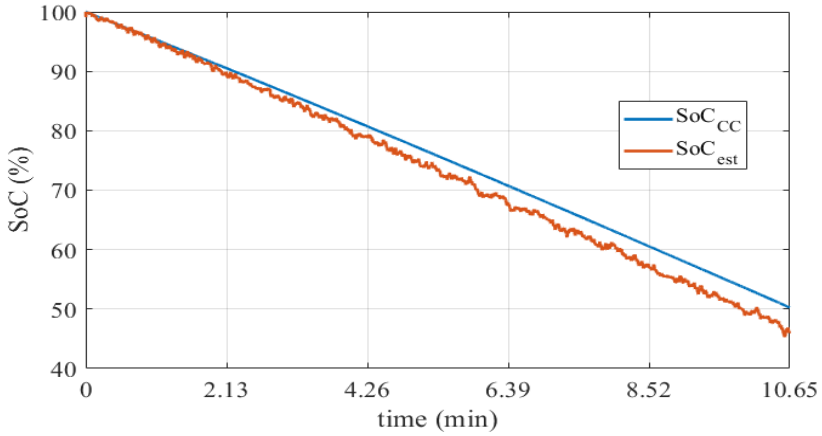

Figure 5.23: State of Charge estimation.

mission development. In addition, During take-off, the current increases, which causes a decrease during the first few minutes of RMT prediction. However, when the hexarotor reaches the desired altitude, and starts moving around the different way-points that characterize the mission, the RMT begins to decrease until it reaches the minimum value at the end of the mission.

As it can be also noted in Figure 5.24 the total mission time was 10.65 min with a final energy consumption of 172.5 kJ or 47.9167 Wh. Such result gives the possibility to extend the task within the mission by considering a more big area to cover and safety region or increase the flight time. However, is it necessary to take into account the constraints linked to maximum Flight Endurance in order to ensure the mission fulfillment.

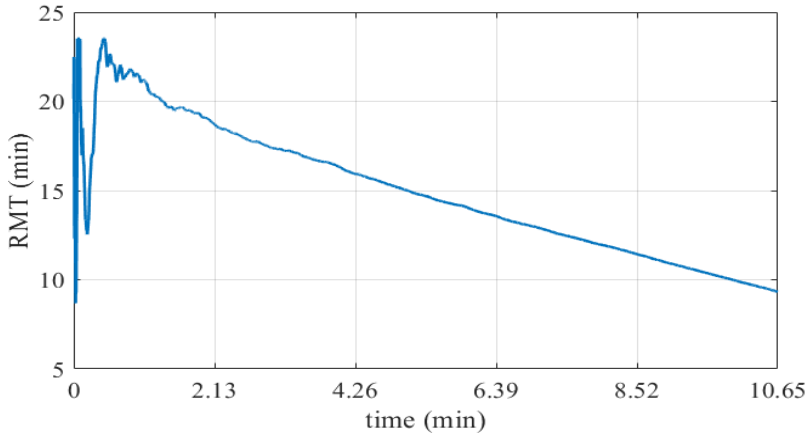

Figure 5.24: Remaining Mission Time and maximum Flight Endurance.

Mission planning based on fault actuator effect

In order to analyze capabilities of mission planning against faults in actuators and to determine when it is possible to re-planning the original path, the faulty situation was introduced. However, it is important to remark that:

- There is no a Fault Diagnosis methodology developed in the system, i.e. the tasks around fault detection, isolation and identification are ideally executed.
- A classic Fault Tolerant Control strategy based on control allocation is considered to illustrate the results.

In addition, the previous considerations are to emphasize that the analysis around faulty situation is not main objective of this work. However it is necessary to remark the effects of faults during mission development. According to ([152]), the control allocation and re-allocation method can be used to accommodate actuator faults. In addition, fault tolerant control can be achieved without the need to reconfigure/restructure the baseline controller due control signals are redistributed among faulty and healthy actuators ([51]). Control allocation method is usually applied on over-actuated systems where the amount of actuators is greater than the controlled variables. By introducing the fault matrix $F = diag([f_1, \cdots, f_n])^{\mathbb{T}}$ the actuator faults can be modeled as the effectiveness loss $0 \leq f_i < 1$, i.e. $f_i = 1$ represent the healthy (or 100 %) ith-actuator, $f_i < 1$ denotes the effectiveness loss of ith-actuator (or less than 100 %) and $f_i = 1$ denotes the complete loss effectiveness of ith-actuator. In addition, the fault severity is associated to the percentage of effectiveness loss in the actuator and the capability of CCL to keep the controllability without reconfigure the control effort ([51]). Then, in order to redistribute the effect of ith faulty actuator, considering the reconfiguration of control effort, the control allocation method is reached by Pseudo-Inverse approach ([165]) by solving

$$\bar{\omega} = \left(FB^{\mathbb{T}}(BFB^{\mathbb{T}})^{-1}\right)\bar{U}. \tag{5.18}$$

As it can be noted in (5.18), the reference control signals are distributed between faulty and healthy actuators according to fault severity. In fault-free case F is set as the identity matrix. However, the control allocation requires information about the fault occurrence as location, time and magnitude of fault. Such information can be provided by an actuator Fault Diagnosis (FD) module which executes the task to detect, isolate and identify the fault.

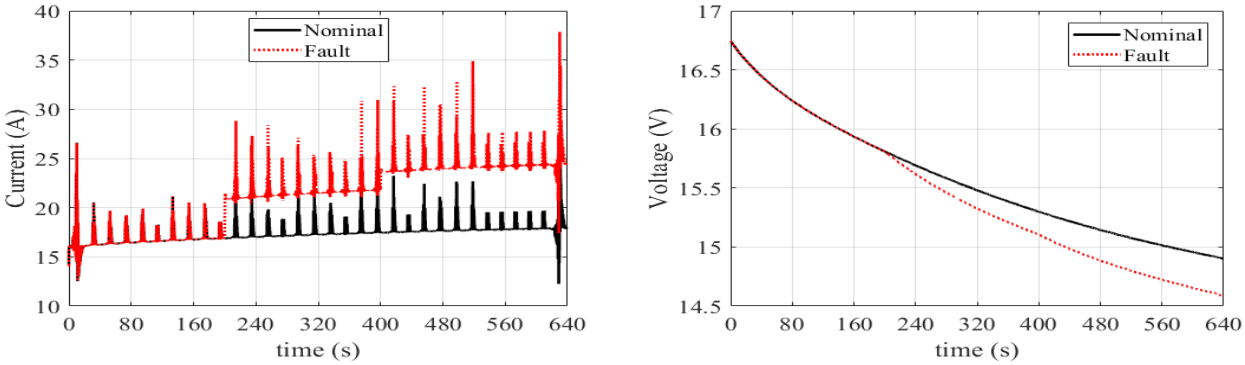

(a) (b)

Figure 5.25: Comparison between battery current (a) and voltage (b) in healthy and faulty situation.

Case 1: Fault effect without reconfiguration

The fault effect was simulated as a loss effectiveness of 70 % of BLDCM 1 at 200 sec and 30 % of BLDCM 5 at 400 sec (according to Figure 4.3). In Figure 5.25-(a) and 5.25-(b) the result of the battery current and battery voltage for nominal and faulty cases is shown. When the fault occurs the battery current increase due the CCL tries to compensate the fault effect. In that sense, the discharge rate increase as it can be observed. This rate increase is noted in the State of Charge in Figure 5.26-(a) where at the end of the mission, the minimum SoC in nominal case is 50.24 % and for the faulty case is 39.48 % with a final energy of 207.3 kJ or 57.58 Wh and maximum flight endurance of 18 min and 13 sec.

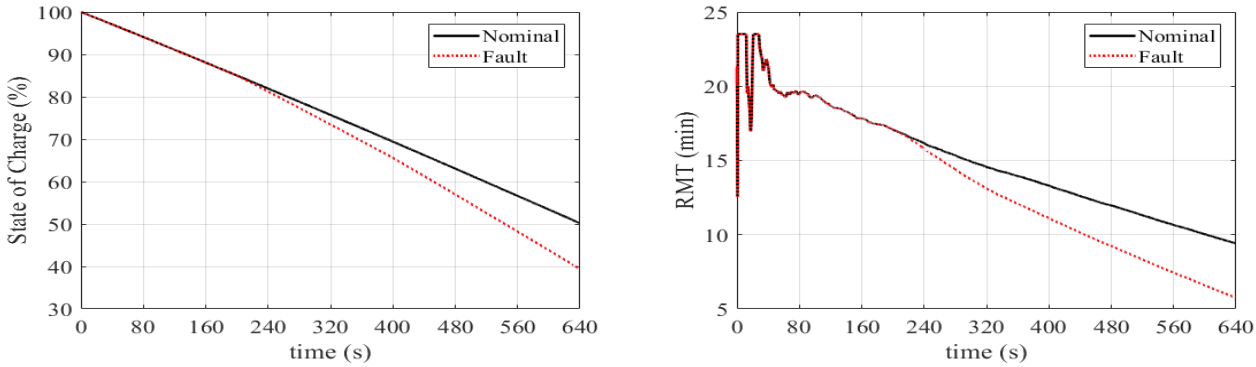

(a) (b)

Figure 5.26: Battery State of Charge at nominal and faulty case (a) and Remaining Mission Time (b).

Case 2: Fault effect with reconfiguration

The control signal efforts after fault occurrence are distributed between the faulty and healthy actuators, 2 sec after the fault is detected, isolated and its magnitude is identified. In the case of reconfiguration of fault in actuator 1 (in Figure 5.27)-(b)), the current tends to decrease in comparison with the faulty case, however when the fault in actuator 5 occurs, the final energy consumption is 192.8 kJ or 53.55 Wh with a maximum flight endurance of 16 min and 28 sec. In such case the reconfiguration of faulty actuator reduce the discharge rate of first fault allowing to fulfill the mission within the maximum flight endurance and energy. In Figure 5.29 the result of reconfiguration of fault in actuator 5 is shown. As it can be observed there is not a significant change in the current magnitude and SoC as well as maximum flight endurance are close to faulty case. In such case, the maximization of flight endurance and minimization of energy consumption after the occurrence of the fault cannot be achieved. This is mainly caused by effect of battery discharge which at certain values of SoC the battery voltage exhibits unpredictable discharge rate. In order to compensate such effect it is necessary to consider additional actions like to reduce the flight speed of vehicle or reconfigure the initial path by reducing the number of way-points. In addition, it is necessary to determines at which SoC levels it is possible to reconfigure the control efforts without to reconfigure the initial mission conditions.

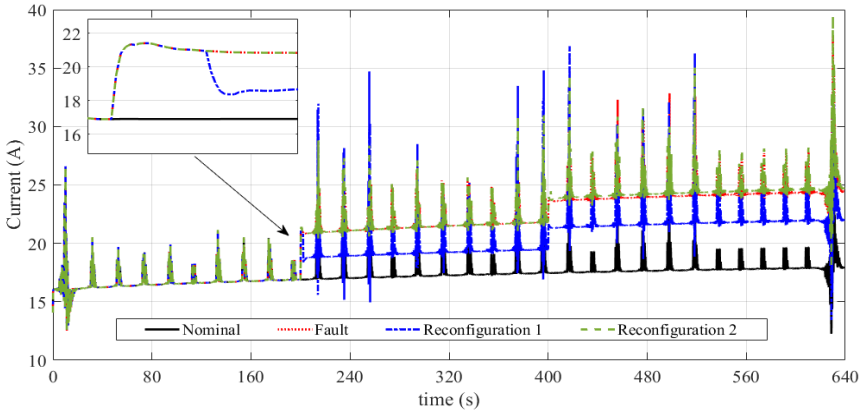

Figure 5.27: Battery battery current with reconfiguration of fault in actuator 1.

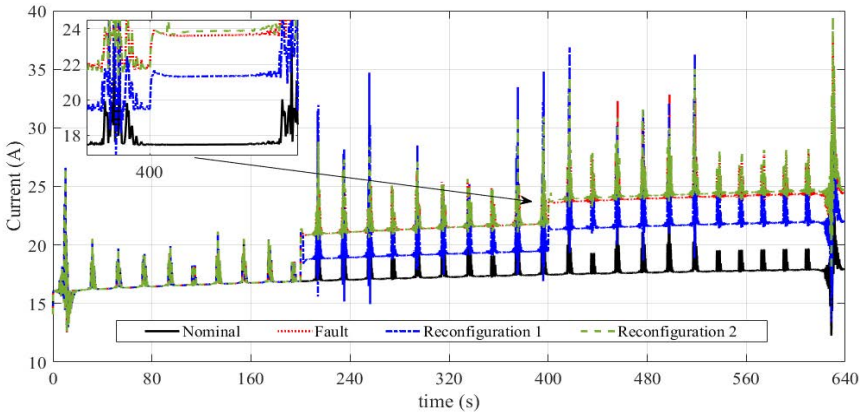

Figure 5.28: Battery battery current with reconfiguration of fault in actuator 2.

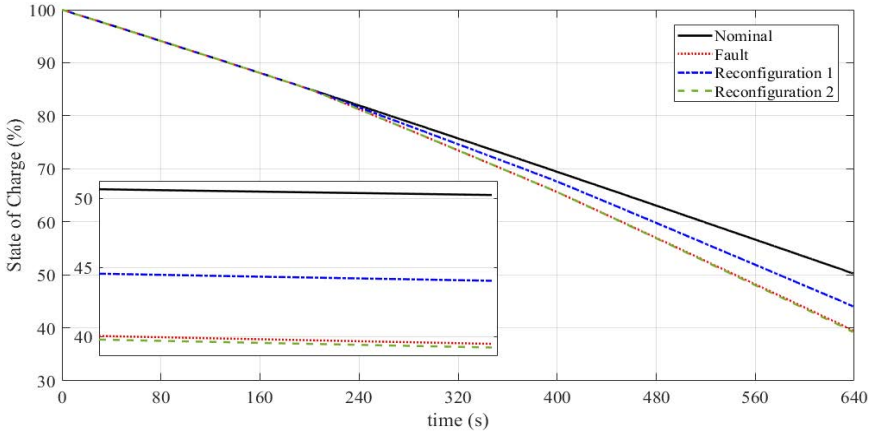

Figure 5.29: Battery SoC after reconfiguration.

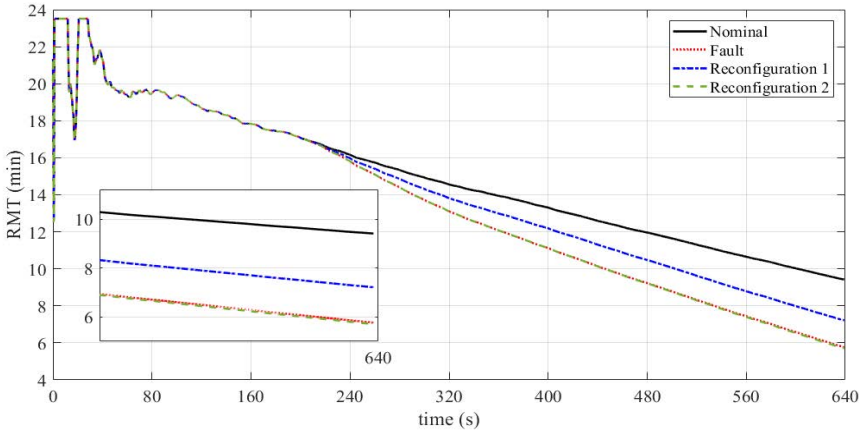

Figure 5.30: Remaining Mission Time after reconfiguration.

5.3 Conclusions

In this Chapter the main elements describing the mission planning methodology were presented. A method to generate minimum energy paths based on a minimization problem was implemented and compared against path generation method based on polynomial functions. The minimum energy paths generated demonstrated that it is possible to minimize the energy consumption during the mission execution taking into account the constraints associated to hexarotor dynamics and battery limitations as discharge effects or State of Health. The interaction between prognosis module with path planning allows to compute the mission time according to flight endurance prediction and to determine the maximum endurance before to launch the mission. On the other hand, the introduction of fault effects in hexarotor actuators allowed to evaluate the necessities to apply a re-planning of the original path in order to avoid the hexarotor crashes due that the energy is not enough to continue with the mission.

Chapter 6

Conclusions and perspectives

In this final Chapter, the conclusions and main results about the different elements integrating the mission planning strategy will be presented. In addition, the core of the contribution is composed by the development of *Prognosis Module* (to execute the SoC estimation, SoH prediction and mission time computation), *Path Definition* (based on multi-objective minimization problem) and *Mission Planning Strategy* (integrating all elements). In that sense, the following conclusions are presented in order to highlight the contributions of this thesis.

6.1 Prognosis and Health Management module

According to results presented in Chapter 4, the Prognosis and Health Management methodology was applied to propulsion system of hexarotor, particularly to battery. This is because the battery is the component within the UAV that requires more attention to develop a mission regardless of the application. On the other hand, However, due to the dynamics that describe the behavior of the battery, the main phenomenon that must be characterized is aging. Aging, as described in Chapter 4, is mainly characterized by the number of charge/discharge cycles and in turn is noticeable once a large number of cycles have been reached. When the problem of battery aging is considered within the development of a mission, it is considerable to introduce strategies or methodologies that take into account energy consumption. Then, taking into account the results presented in Chapter 4, the following conclusions are retaken and re-marked:

- Estimation of battery State of Charge (SoC). In order to ensure a proper and accurate calculation of the total charge of the battery during the development of the mission, it was chosen to use an Extended Kalman Filter (EKF) to estimate the State of Charge of the battery. The EKF in comparison with the classic Coulomb Counting (CC) method, proved to offer a better characterization of the battery charge during the development of the mission.

- Computation of battery SoH by using degradation models. The use of model-based Prognosis techniques allowed to define two models of degradation that characterize the aging of the battery: the capacity loss and the increase of the internal resistance. With such degradation models, it is possible to determine the current state of battery State of Health (SoH), determine energy limits and establish replacement times.

- Prediction of FE during mission development and computation of Remaining Mission Time (RMT). Within the main requirements of the mission, is the maximum flight time. As demonstrated in chapter 4, using battery information such as capacity (in Ah) and taking into account the dynamics of the actuators, it was possible to establish the maximum energy that the battery can supply and the maximum flight time according to the current demanded by the actuators. in addition, the main

contribution around this conclusion is the generated endurance model, which is able to determine the maximum endurance according to battery characteristics as Capacity and C-rate and demanded current per BLDCM.

In perspective, it is important to remark that the proposed method considers that the battery aging is mainly liking to battery cycling in that sense. It is necessary to ensure about the real aging of the battery by running degradation tests which take into account different operation conditions associated to C-rate and temperature. On the other hand, the Prediction of FE requires experimental validation considering outdoor mission with large flight time and long distance. However, the simulation results are representative of what might happen during a real mission.

6.2 Mission planning and path planning

On the other hand, the mission planning strategy and path planning based on energy consumption allowed to establish the relationship between Prognosis Module and energy consumption with hexarotor and propulsion system dynamics. As it was shown in Chapter 5, the use of polynomial functions is useful to meet the requirements of smooth and minimum energy trajectories. However, such assumption is based on the fact that the hexarotor has an adequate and robust position control and orientation capable of following a reference trajectory with a tracking error close to zero. In that sense, the use of optimization techniques based on the criteria of minimum energy, resulted in a better option because such techniques take into account the restrictions associated with the vehicle, such as the control inputs, the SoC and SoH of the battery. With this, it is possible a) to identify the energy limitations of multirotor UAV during mission development and b) Improve the multirotor flight capabilities by taking into account the energy consumption, and finally c) the maximization of Flight Endurance (FE) in order to have long-time mission for general applications (surveillance, exploring, mapping and photogrammetry) by taking into account the battery limitations.

In addition, it is possible to consider other methods as Model Predictive Control to generate optimal and minimum energy paths whiles the constraints associated to battery energy and vehicle dynamics are taking into account. In that sense, it will be possible to obtain a different control loop associated to position and orientation of hexarotor. Such consideration was not included during the development of the path and mission planning strategy, however it will be considered as future works to generate a validation of proposed method.

On the other hand, the method used to generate the Cascade Control Loop, such as the consideration of a linear model for hexarotor dynamics and the integration of propulsion system allowed to generate a more realistic representation of real behavior of a flight. However, the objective of this thesis was not create a control loop but due to the dynamics of hexarotor it was necessary to include that information during the thesis development. In addition, the analysis around fault effects was to demonstrate the capabilities of the proposed method to manage the faulty situation, in that sense, the analysis and obtained results were only to emphasize the need to include a Fault Tolerant Control system but such development is out of the vision of this work. However, it will be considered in future works.

As it was mentioned in Chapter 3, during description of Cascade Control Loop, the mission planning and path planning method introduced in this thesis are focus to execute mission with long time-distance path without aggressive maneuvers. In that sense, the prognosis of FE and RMT plays an important role to determine the maximum flight time and to define the constraints of energy supplied by battery.

Appendix

Appendix A. Parametrization of lithium battery

In order to obtain the parameters of the dynamic model of the battery voltage, a process of parameter identification is performed by using experimental data from a Li-Po battery. Such procedure is based on the methodology proposed by ([31]). In Table 6.1 the characteristics of the Li-Po battery are enlisted.

Table 6.1: Characteristics of the battery

Parameter	**Value**
Cells	4
Capacity	6200 mAh
C-Rate	25 C
Min voltage per cell	3.5 V
Max voltage per cell	4.2 V
Total minimum voltage	14 V
Total voltage max	16.8 V

In addition, the parameter estimation is based on the mathematical model of battery which is expressed as an equivalent circuit model (Figure (6.1)) as described in Chapter 3.

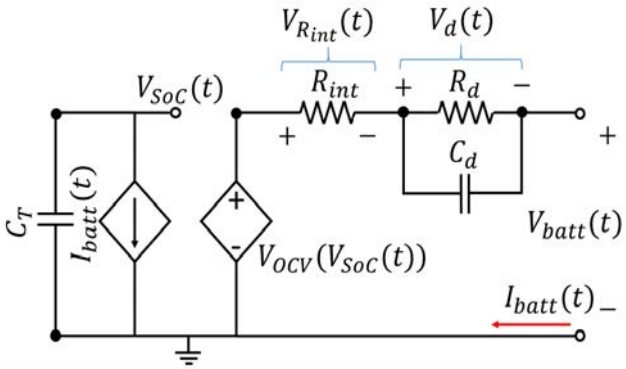

Figure 6.1: Equivalent Circuit Model of Li-Po battery.

$$\begin{aligned} \dot{V}_{SoC} &= -\frac{I_{batt}}{3600 \cdot C_T} \\ \dot{V}_d &= -\frac{V_d}{R_d \cdot C_d} + \frac{I_{batt}}{C_d} \\ V_{Batt} &= V_{OCV}(V_{SoC}) - V_d - R_{int}\, I_{batt}, \end{aligned} \tag{6.1}$$

where the $V_{OCV}(V_{SoC})$ is a function of State of Charge and mathematically could be expressed as:

$$V_{OCV}(V_{SoC}) = \sum_{i=0}^{n} \lambda_i V_{SoC}^i + \ln(V_{SoC}) V_{SoC}. \tag{6.2}$$

n determines the order of the polynomial, and λ_i are the polynomial coefficients. It can be noted that the nonlinear function (6.2) is not unique and its formulation is obtained through experimental tests.

A discharge current profile characterized by steps was applied to the battery through a rheostat. The test consisted in applying a current step for twenty-seven minutes followed by a rest period of the same time value in order to reach the Open Circuit Voltage (OCV). Each current step discharged the battery in steps of 10 %. In Figure 6.2 the demanded current profile and battery voltage are shown.

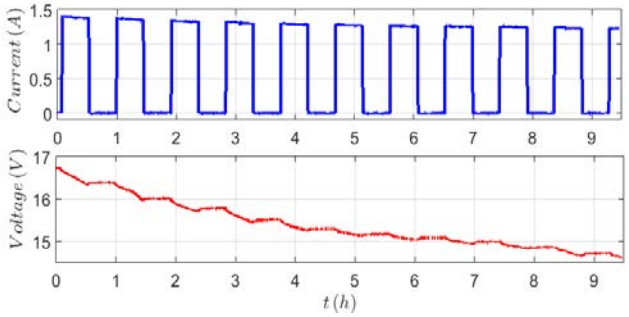

Figure 6.2: Discharge current profile and battery voltage.

The State of Charge (SoC) of a cell or a battery at a given time is the proportion of the charge available at that instant of time, compared to the total charge available when it is fully charged. It is expressed in percent from 100 % (or 1 %) when the battery is full charged and, 0% when it is empty. The SoC evaluation function is also known as the fuel gauge, especially in Electrical Vehicle's because of its analogy to a gas car's fuel gauge. Coulomb counting or Ampere-hour counting is the most commonly used method for SoC computation ([61]), such as

$$SoC\,(t) = SoC\,(t_o) - \frac{1}{3600 C_T} \int_{t_o}^{t} I_{batt}(t) dt, \tag{6.3}$$

where t_o represents the initial time. Figure 6.3 shows the SoC of the battery computed through Coulomb counting which corresponds to the demanding current applied to the battery. It is also observed that the battery reached the minimum total voltage of 14.5 V. The measurement of the SoC allows to know the final value of discharge of the battery.
The relationship between the SoC in each rest period and the open circuit voltage of the battery is shown in Figure 6.4. Note that, there is a nearly linear behavior from 50% to full charge, an exponential decay until reaching 0% of charge. This behavior was characterized by the following polynomial function:

$$V_{OCV}(SoC) = 13.55 SoC(t)^5 - 41.10 SoC(t)^4 + 46.49 SoC(t)^3 - 21.94 SoC(t)^2 + 5.22 SoC(t) + 14.52. \tag{6.4}$$

Identification through Least-Square

According to system (6.1), the total voltage battery is a difference between the open circuit voltage and two voltage drops: $V_{R_{int}}(t)$ and $V_d(t)$ as

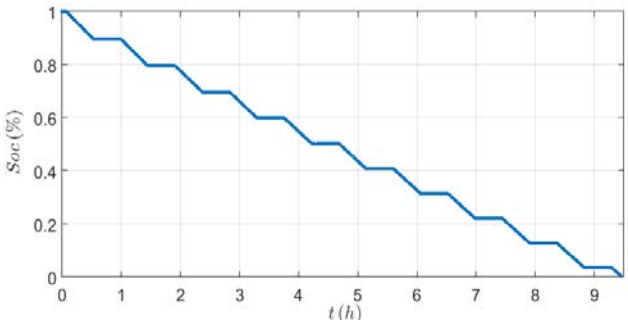

Figure 6.3: State of charge of the demanding current.

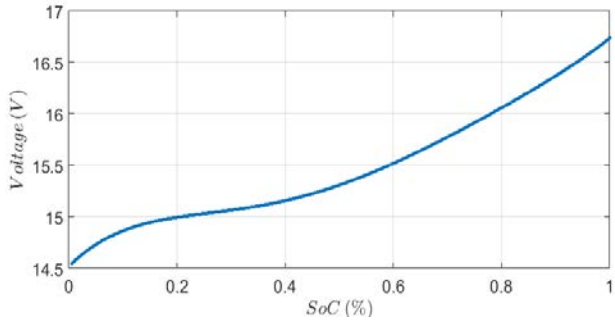

Figure 6.4: Relationship between the SoC and the open circuit voltage.

$$V_{batt}(t) = V_{OC}(SoC(t)) - V_{R_i}(t) - V_d(t), \tag{6.5}$$

The open circuit voltage as it was mentioned above is a function of the state of charge of battery, and it represents the static behavior of the battery voltage. In this sense, by means of subtracting this voltage from the battery total voltage $V_{batt}(t)$ of the experimental data, the transient behavior of the battery voltage denoted by $V_{trans}(t)$ is computed as follows (to see Fig. 6.5):

$$\begin{aligned} V_{trans}(t) &= V_{batt}(t) - V_{OC}(SoC(t)) \\ &= V_d(t) - V_{R_{int}}(t) \end{aligned} \tag{6.6}$$

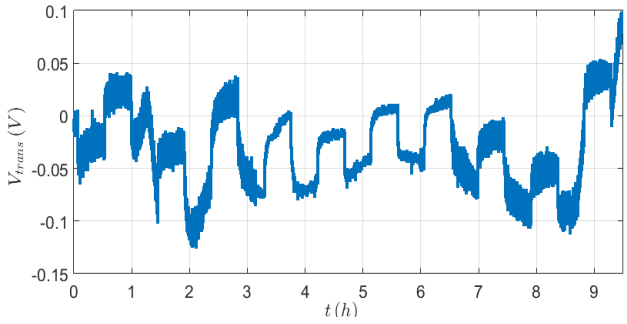

Figure 6.5: Relationship between the SoC and the open circuit voltage.

By considering the Laplace transformation of the $V_{trans}(t)$:

$$V_{trans}(s) = \left(\frac{\frac{1}{C_d}}{s + \frac{1}{R_d C_d}} + R_{int} \right) I_{batt}(s), \tag{6.7}$$

and a sampling time T_s, the above equation is discretized by the backward Euler method, considering $s = \frac{1-z^{-1}}{T_s}$, as follows:

$$V_{trans}(z) = \frac{b_0 + z^{-1}b_1}{1 + z^{-1}a_1} I_{batt(z)}, \tag{6.8}$$

where $b_0 = R_{int}$, $b_1 = T_s/C_d + T_s R_{int}/C_d R_d - R_{int}$, and $a_1 = T_s/C_d R_d - 1$. The above discrete transfer function can be written as difference equation:

$$\begin{aligned} V_{trans}(k) &= b_0 I_{batt}(k) + b_1 I_{batt}(k-1) \\ &\quad -a_1 V_{trans}(k-1). \end{aligned} \tag{6.9}$$

The parameters b_0, b_1, and a_1 can be determined by using the method of least-squares (LS), which is derived as follows:

$$V_{trans}(k) = \xi^{\mathsf{T}}(k)\gamma, \tag{6.10}$$

with the parameters vector

$$\gamma = [a_1,\, b_0,\, b_1]^{\mathsf{T}}, \tag{6.11}$$

and discrete-time data of the system

$$\xi(k) = [-V_{trans}(k-1),\, I_{batt}(k),\, I_{batt}(k-1)]^{\mathsf{T}}, \tag{6.12}$$

the least-square estimate is computed as:

$$\hat{\gamma}(k) = (\xi^{\mathsf{T}}\xi)^{-1}\xi^{\mathsf{T}} V_{trans}(k). \tag{6.13}$$

The obtained parameters are registered in Table 6.2. Note that the parameter b_0 corresponding to the internal resistance of the battery which can be used to determined the state of health of the battery and to predict the remaining useful life by considering prognosis techniques.

Table 6.2: Parameters of the battery model

Parameter	**Value**
R_d	$3.7307 \times 10^{-3}\ \Omega$
C_d	9.5730×10^{3} F
R_{int}	$0.0392\ \Omega$

A comparison between the mathematical model and experimental data is made in order to show the capacity of the model to characterize the dynamic behavior of the battery with the estimated parameters. The response of the mathematical model was compared with experimental voltage of the battery in Fig. 6.6 and the mean square error (MSR) was computed with a value of 9.5681×10^{-4}. Other comparison was made with experimental data obtained from the battery by applying a constant current of $5\,A$. In Fig. 6.7 the comparison between the model response and the experimental voltage is shown, with a MSR of 0.0061. As it can be observed in both comparisons the mathematical model reproduce adequately the dynamical behavior of the experimental voltage.

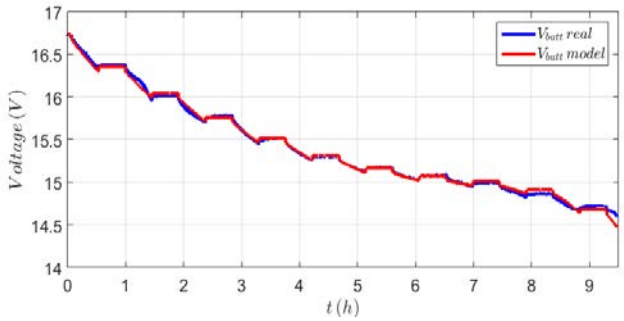

Figure 6.6: Comparison 1 between the mathematical model and experimental data.

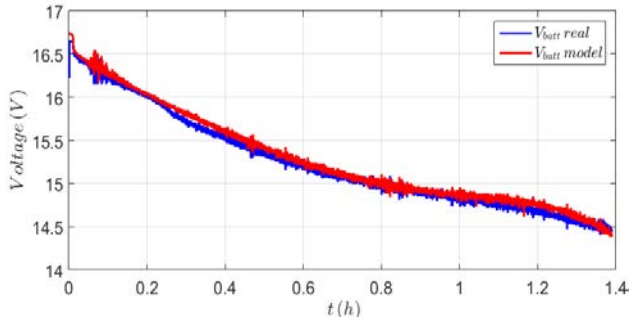

Figure 6.7: Comparison 2 between the mathematical model and experimental data.

Bibliography

[1] A. Abdilla, A. Richards, and S. Burrow. Endurance optimisation of battery-powered rotorcraft. In *Conference Towards Autonomous Robotic Systems*, pages 1–12. Springer, 2015.

[2] A. Abdilla, A. Richards, and S. Burrow. Power and endurance modelling of battery-powered rotorcraft. In *2015 IEEE/RSJ International Conference on Intelligent Robots and Systems (IROS)*, pages 675–680. IEEE, 2015.

[3] D. E. Acuña and M. E. Orchard. Particle-filtering-based failure prognosis via sigma-points: Application to lithium-ion battery state-of-charge monitoring. *Mechanical Systems and Signal Processing*, 85:827–848, 2017.

[4] Y. Al Younes, A. Drak, H. Noura, A. Rabhi, and A. El Hajjaji. Robust model-free control applied to a quadrotor uav. *Journal of Intelligent & Robotic Systems*, 84(1-4):37–52, 2016.

[5] A. Alaimo, V. Artale, C. L. R. Milazzo, and A. Ricciardello. Pid controller applied to hexacopter flight. *Journal of Intelligent & Robotic Systems*, 73(1-4):261–270, 2014.

[6] D. Aleksandrov and I. Penkov. Energy consumption of mini uav helicopters with different number of rotors. In *11th International Symposium" Topical Problems in the Field of Electrical and Power Engineering*, pages 259–262, 2012.

[7] A. Alkamachi and E. Erçelebi. Modelling and genetic algorithm based-pid control of h-shaped racing quadcopter. *Arabian Journal for Science and Engineering*, 42(7):2777–2786, 2017.

[8] Y. Alothman, M. Guo, and D. Gu. Using iterative lqr to control two quadrotors transporting a cable-suspended load. *IFAC-PapersOnLine*, 50(1):4324–4329, 2017.

[9] D. An, N. H. Kim, and J.-H. Choi. Practical options for selecting data-driven or physics-based prognostics algorithms with reviews. *Reliability Engineering & System Safety*, 133:223–236, 2015.

[10] D. Andre, A. Nuhic, T. Soczka-Guth, and D. U. Sauer. Comparative study of a structured neural network and an extended kalman filter for state of health determination of lithium-ion batteries in hybrid electricvehicles. *Engineering Applications of Artificial Intelligence*, 26(3):951–961, 2013.

[11] L. M. Argentim, W. C. Rezende, P. E. Santos, and R. A. Aguiar. Pid, lqr and lqr-pid on a quadcopter platform. In *2013 International Conference on Informatics, Electronics and Vision (ICIEV)*, pages 1–6. IEEE, 2013.

[12] G. Bai, P. Wang, C. Hu, and M. Pecht. A generic model-free approach for lithium-ion battery health management. *Applied Energy*, 135:247–260, 2014.

[13] M. Baptista, E. M. Henriques, I. P. de Medeiros, J. P. Malere, C. L. Nascimento Jr, and H. Prendinger. Remaining useful life estimation in aeronautics: Combining data-driven and kalman filtering. *Reliability Engineering & System Safety*, 184:228–239, 2019.

[14] J. Bellingham, M. Tillerson, A. Richards, and J. P. How. Multi-task allocation and path planning for cooperating uavs. In *Cooperative control: models, applications and algorithms*, pages 23–41. Springer, 2003.

[15] J. Betancourt-Vera, P. Castillo, R. Lozano, and B. Vidolov. Robust control scheme for trajectory generation and tracking for quadcopters vehicles: Experimental results. In *2018 International Conference on Unmanned Aircraft Systems (ICUAS)*, pages 1118–1124. IEEE, 2018.

[16] B. S. Bhangu, P. Bentley, D. A. Stone, and C. M. Bingham. Nonlinear observers for predicting state-of-charge and state-of-health of lead-acid batteries for hybrid-electric vehicles. *IEEE transactions on vehicular technology*, 54(3):783–794, 2005.

[17] A. Bircher, M. Kamel, K. Alexis, H. Oleynikova, and R. Siegwart. Receding horizon path planning for 3d exploration and surface inspection. *Autonomous Robots*, 42(2):291–306, 2018.

[18] L. A. Blas, M. Bonilla, S. Salazar, M. Malabre, and V. Azhmyakov. Synthesis of a robust linear structural feedback linearization scheme for an experimental quadrotor. In *ECC19 European Control Conference*, 2019.

[19] T. I. Bø and T. A. Johansen. Battery power smoothing control in a marine electric power plant using nonlinear model predictive control. *IEEE Transactions on Control Systems Technology*, 25(4):1449–1456, 2017.

[20] S. Bouabdallah, A. Noth, and R. Siegwart. Pid vs lq control techniques applied to an indoor micro quadrotor. In *2004 IEEE/RSJ International Conference on Intelligent Robots and Systems (IROS)(IEEE Cat. No. 04CH37566)*, volume 3, pages 2451–2456. IEEE, 2004.

[21] G. E. Box and G. C. Tiao. *Bayesian inference in statistical analysis*, volume 40. John Wiley & Sons, 2011.

[22] M. Broussely, P. Biensan, F. Bonhomme, P. Blanchard, S. Herreyre, K. Nechev, and R. Staniewicz. Main aging mechanisms in li ion batteries. *Journal of power sources*, 146(1-2):90–96, 2005.

[23] W. Caesarendra, A. Widodo, and B.-S. Yang. Application of relevance vector machine and logistic regression for machine degradation assessment. *Mechanical Systems and Signal Processing*, 24(4):1161–1171, 2010.

[24] L. R. G. Carrillo, A. E. D. López, R. Lozano, and C. Pégard. *Quad rotorcraft control: vision-based hovering and navigation*. Springer Science & Business Media, 2012.

[25] A. Chamseddine, Y. Zhang, C. A. Rabbath, C. Join, and D. Theilliol. Flatness-based trajectory planning/replanning for a quadrotor unmanned aerial vehicle. *IEEE Transactions on Aerospace and Electronic Systems*, 48(4):2832–2848, 2012.

[26] K. Chang, P. Rammos, S. Wilkerson, M. Bundy, and S. A. Gadsden. Lipo battery energy studies for improved flight performance of unmanned aerial systems. In *SPIE Defense+ Security*, pages 98370W–98370W. International Society for Optics and Photonics, 2016.

[27] K. Chen, S. Laghrouche, and A. Djerdir. Fuel cell health prognosis using unscented kalman filter: Postal fuel cell electric vehicles case study. *International Journal of Hydrogen Energy*, 44(3):1930–1939, 2019.

[28] M. Chen and G. A. Rincon-Mora. Accurate electrical battery model capable of predicting runtime and IV performance. *IEEE transactions on energy conversion*, 21(2):504–511, 2006.

[29] X. Chen, W. Shen, Z. Cao, and A. Kapoor. A novel approach for state of charge estimation based on adaptive switching gain sliding mode observer in electric vehicles. *Journal of Power Sources*, 246:667–678, 2014.

[30] X. Chen, J. Yu, D. Tang, and Y. Wang. Probabilistic residual life prediction for lithium-ion batteries based on bayesian ls-svr. *Acta Aeronautica et Astronautica Sinica*, 34(9):2219–2229, 2013.

[31] Z. Chen, Y. Fu, and C. C. Mi. State of charge estimation of lithium-ion batteries in electric drive vehicles using extended kalman filtering. *IEEE Transactions on Vehicular Technology*, 62(3):1020–1030, 2013.

[32] Z. Chen, X. Tu, F. Jian, L. Rogelio, and B. Ren. Sliding mode control for systems with state constraints: Application to a quadrotor mav. In *2018 37th Chinese Control Conference (CCC)*, pages 2977–2981. IEEE, 2018.

[33] F. Cheng, W. Hua, and C. Pin. Rotorcraft flight endurance estimation based on a new battery discharge model. *Chinese Journal of Aeronautics*, 30(4):1561–1569, 2017.

[34] J. B. Coble. Mergin data sources to predict remaining useful life - an automated method to identify prognostic parameters, 2010.

[35] B. N. Coelho. Uavs and their role in future cities and industries. In *Smart and Digital Cities*, pages 275–285. Springer, 2019.

[36] A. Cordoba-Arenas, S. Onori, G. Rizzoni, and G. Fan. Aging propagation in advanced battery systems: Preliminary results. *IFAC Proceedings Volumes*, 46(21):313–318, 2013.

[37] P. Corke. *Robotics, Vision and Control: Fundamental Algorithms In MATLAB® Second, Completely Revised*, volume 118. Springer, 2017.

[38] M. J. Daigle and C. S. Kulkarni. Electrochemistry-based battery modeling for prognostics. 2013.

[39] X. Dang, L. Yan, K. Xu, X. Wu, H. Jiang, and H. Sun. Open-circuit voltage-based state of charge estimation of lithium-ion battery using dual neural network fusion battery model. *Electrochimica Acta*, 188:356–366, 2016.

[40] J. Das, G. Cross, C. Qu, A. Makineni, P. Tokekar, Y. Mulgaonkar, and V. Kumar. Devices, systems, and methods for automated monitoring enabling precision agriculture. In *2015 IEEE International Conference on Automation Science and Engineering (CASE)*, pages 462–469. IEEE, 2015.

[41] A. Dasgupta. Physics-of-failure methods and prognostic and health management of electronic components. In *Risk Based Technologies*, pages 15–23. Springer, 2019.

[42] A. De Souza Cândido, R. K. H. Galvão, and T. Yoneyama. Control and energy management for quadrotor. In *Control (CONTROL), 2014 UKACC International Conference on*, pages 343–348. IEEE, 2014.

[43] F. Di Maio, K. L. Tsui, and E. Zio. Combining relevance vector machines and exponential regression for bearing residual life estimation. *Mechanical Systems and Signal Processing*, 31:405–427, 2012.

[44] T. Dietrich, S. Krug, and A. Zimmermann. An empirical study on generic multicopter energy consumption profiles. In *Systems Conference (SysCon), 2017 Annual IEEE International*, pages 1–6. IEEE, 2017.

[45] DJI. Flamewheel 550 user manual v2.0.

[46] T. Donateo, A. Ficarella, L. Spedicato, A. Arista, and M. Ferraro. A new approach to calculating endurance in electric flight and comparing fuel cells and batteries. *Applied Energy*, 187:807–819, 2017.

[47] M. Dong and D. He. Hidden semi-markov model-based methodology for multi-sensor equipment health diagnosis and prognosis. *European Journal of Operational Research*, 178(3):858–878, 2007.

[48] C. G. Downes. Astraea t7—an architectural outline for system health management on civil uavs. In *2007 Institution of Engineering and Technology Conference on Autonomous Systems*, pages 1–4. IET, 2007.

[49] S. Driessens and P. E. Pounds. Towards a more efficient quadrotor configuration. In *Intelligent Robots and Systems (IROS), 2013 IEEE/RSJ International Conference on*, pages 1386–1392. IEEE, 2013.

[50] G. R. Drozeski. *A fault-tolerant control architecture for unmanned aerial vehicles*. PhD thesis, Georgia Institute of Technology, 2005.

[51] G.-X. Du, Q. Quan, B. Yang, and K.-Y. Cai. Controllability analysis for multirotor helicopter rotor degradation and failure. *Journal of Guidance, Control, and Dynamics*, 38(5):978–985, 2015.

[52] A. A. El-samahy and M. A. Shamseldin. Brushless dc motor tracking control using self-tuning fuzzy pid control and model reference adaptive control. *Ain Shams Engineering Journal*, 2016.

[53] J. Escareño, S. Salazar, H. Romero, and R. Lozano. Trajectory control of a quadrotor subject to 2d wind disturbances. *Journal of Intelligent & Robotic Systems*, 70(1-4):51–63, 2013.

[54] J. Fan, K.-C. Yung, and M. Pecht. Predicting long-term lumen maintenance life of led light sources using a particle filter-based prognostic approach. *Expert systems with applications*, 42(5):2411–2420, 2015.

[55] D. Galar, U. Kumar, R. Villarejo, and C.-A. Johansson. Hybrid prognosis for railway health assessment: an information fusion approach for phm deployment. *Chemical Engineering*, 33, 2013.

[56] D. Galar, A. Thaduri, M. Catelani, and L. Ciani. Context awareness for maintenance decision making: A diagnosis and prognosis approach. *Measurement*, 67:137–150, 2015.

[57] D. A. Gandhi and M. Ghosal. Novel low cost quadcopter for surveillance application. In *2018 International Conference on Inventive Research in Computing Applications (ICIRCA)*, pages 412–414. IEEE, 2018.

[58] A. Gargioli, F. Rinaldi, and F. Quagliotti. Proportional integral derivative and linear quadratic regulation of a multirotor attitude: mathematical modelling, simulations and experimental results. In *2013 International Conference on Unmanned Aircraft Systems (ICUAS)*, pages 433–442. IEEE, 2013.

[59] M. Gatti, F. Giulietti, and M. Turci. Maximum endurance for battery-powered rotary-wing aircraft. *Aerospace Science and Technology*, 45:174–179, 2015.

[60] J. Ge, M. Roemer, and G. Vachtsevanos. An automated contingency management simulation environment for integrated health management and control. In *2004 IEEE Aerospace Conference Proceedings (IEEE Cat. No. 04TH8720)*, volume 6, pages 3725–3732. IEEE, 2004.

[61] M. Gholizadeh and F. R. Salmasi. Estimation of state of charge, unknown nonlinearities, and state of health of a lithium-ion battery based on a comprehensive unobservable model. *IEEE Transactions on Industrial Electronics*, 61(3):1335–1344, 2014.

[62] K. Goebel, M. Dagle, A. Saxena, S. Sankararama, I. Roychoudhury, and J. R. Celaya. *PROGNOSTICS The Science of Prediction*. 2017.

[63] K. Goebel, B. Saha, and A. Saxena. A comparison of three data-driven techniques for prognostics. In *62nd meeting of the society for machinery failure prevention technology (mfpt)*, pages 119–131, 2008.

[64] E. Grall-Maes, P. Beauseroy, and A. Grall. Degradation prognosis based on a model of gamma process mixture. In *Second European Conference of the Prognostics and Health Management Society*, pages 194–201, 2014.

[65] D. R. Green, J. J. Hagon, and C. Gomez. Using low cost uavs for environmental monitoring, mapping and modelling: Examples from the coastal zone. In *Coastal Management: Global Challenges and Innovations*. Elsevier, 2018.

[66] R. Guardeño, M. J. López, and V. M. Sánchez. Mimo pid controller tuning method for quadrotor based on lqr/lqg theory. *Robotics*, 8(2):36, 2019.

[67] S. Gupte, P. I. T. Mohandas, and J. M. Conrad. A survey of quadrotor unmanned aerial vehicles. In *2012 Proceedings of IEEE Southeastcon*, pages 1–6. IEEE, 2012.

[68] D. Haifeng, W. Xuezhe, and S. Zechang. A new soh prediction concept for the power lithium-ion battery used on hevs. In *Vehicle Power and Propulsion Conference, 2009. VPPC'09. IEEE*, pages 1649–1653. IEEE, 2009.

[69] H. He, R. Xiong, X. Zhang, F. Sun, and J. Fan. State-of-charge estimation of the lithium-ion battery using an adaptive extended kalman filter based on an improved thevenin model. *IEEE Transactions on vehicular technology*, 60(4):1461–1469, 2011.

[70] W. He, N. Williard, C. Chen, and M. Pecht. State of charge estimation for electric vehicle batteries using unscented kalman filtering. *Microelectronics Reliability*, 53(6):840–847, 2013.

[71] W. He, N. Williard, M. Osterman, and M. Pecht. Prognostics of lithium-ion batteries based on dempster–shafer theory and the bayesian monte carlo method. *Journal of Power Sources*, 196(23):10314–10321, 2011.

[72] R. Heidary, S. A. Gabriel, M. Modarres, K. M. Groth, and N. Vahdati. A review of data-driven oil and gas pipeline pitting corrosion growth models applicable for prognostic and health management. *Int. J. Progn. Health Manag*, 9(1), 2018.

[73] C. Hu, B. D. Youn, and P. Wang. Time-dependent reliability analysis in operation: Prognostics and health management. In *Engineering Design under Uncertainty and Health Prognostics*, pages 233–301. Springer, 2019.

[74] C. Hu, B. D. Youn, P. Wang, et al. *Engineering Design Under Uncertainty and Health Prognostics*. Springer, 2019.

[75] X. Hu, F. Sun, and Y. Zou. Estimation of state of charge of a lithium-ion battery pack for electric vehicles using an adaptive luenberger observer. *Energies*, 3(9):1586–1603, 2010.

[76] S. Islam, P. Liu, and A. El Saddik. Nonlinear adaptive control for quadrotor flying vehicle. *Nonlinear Dynamics*, 78(1):117–133, 2014.

[77] H. A. Izadi, Y. Zhang, and B. W. Gordon. Fault tolerant model predictive control of quad-rotor helicopters with actuator fault estimation. *IFAC Proceedings Volumes*, 44(1):6343–6348, 2011.

[78] A. A. Jaoude, K. El-Tawil, S. Kadry, H. Noura, and M. Ouladsine. Analytic prognostic model for a dynamic system. *International Review of Automatic Control*, 3(6):568–577, 2010.

[79] T. Jiřinec. Stabilization and control of unmanned quadcopter, 2011.

[80] C. Julien, A. Mauger, A. Vijh, and K. Zaghib. Lithium batteries. In *Lithium Batteries*, pages 29–68. Springer, 2016.

[81] E. Kayacan and R. Maslim. Type-2 fuzzy logic trajectory tracking control of quadrotor vtol aircraft with elliptic membership functions. *IEEE/ASME Transactions on Mechatronics*, 22(1):339–348, 2016.

[82] P. Khumprom and N. Yodo. A data-driven predictive prognostic model for lithium-ion batteries based on a deep learning algorithm. *Energies*, 12(4):660, 2019.

[83] I.-S. Kim. The novel state of charge estimation method for lithium battery using sliding mode observer. *Journal of Power Sources*, 163(1):584–590, 2006.

[84] N.-H. Kim, D. An, and J.-H. Choi. *Prognostics and Health Management of Engineering Systems*. Springer, 2017.

[85] B. B. Kocer, T. Tjahjowidodo, and G. G. L. Seet. Centralized predictive ceiling interaction control of quadrotor vtol uav. *Aerospace Science and Technology*, 76:455–465, 2018.

[86] N. Kreciglowa, K. Karydis, and V. Kumar. Energy efficiency of trajectory generation methods for stop-and-go aerial robot navigation. In *Unmanned Aircraft Systems (ICUAS), 2017 International Conference on*, pages 656–662. IEEE, 2017.

[87] E. Kuantama, I. Tarca, and R. Tarca. Feedback linearization lqr control for quadcopter position tracking. In *2018 5th International Conference on Control, Decision and Information Technologies (CoDIT)*, pages 204–209. IEEE, 2018.

[88] R. Kumar, M. Dechering, A. Pai, A. Ottaway, M. Radmanesh, and M. Kumar. Differential flatness based hybrid pid/lqr flight controller for complex trajectory tracking in quadcopter uavs. In *2017 IEEE National Aerospace and Electronics Conference (NAECON)*, pages 113–118. IEEE, 2017.

[89] D. Kwon, M. H. Azarian, and M. Pecht. Remaining-life prediction of solder joints using rf impedance analysis and gaussian process regression. *IEEE Transactions on Components, Packaging and Manufacturing Technology*, 5(11):1602–1609, 2015.

[90] A. L'afflitto, R. B. Anderson, and K. Mohammadi. An introduction to nonlinear robust control for unmanned quadrotor aircraft: How to design control algorithms for quadrotors using sliding mode control and adaptive control techniques [focus on education]. *IEEE Control Systems*, 38(3):102–121, 2018.

[91] C.-H. Lee and C.-J. Jin. A reinforcement learning method of pid parameters in uav's flight control. In *Engineering Innovation and Design: Proceedings of the 7th International Conference on Innovation, Communication and Engineering (ICICE 2018), November 9-14, 2018, Hangzhou, China*, page 135. CRC Press, 2019.

[92] D. Lee, H. J. Kim, and S. Sastry. Feedback linearization vs. adaptive sliding mode control for a quadrotor helicopter. *International Journal of control, Automation and systems*, 7(3):419–428, 2009.

[93] H. Lee and H. J. Kim. Trajectory tracking control of multirotors from modelling to experiments: A survey. *International Journal of Control, Automation and Systems*, 15(1):281–292, 2017.

[94] H. Li, H.-Z. Huang, Y.-F. Li, J. Zhou, and J. Mi. Physics of failure-based reliability prediction of turbine blades using multi-source information fusion. *Applied Soft Computing*, 72:624–635, 2018.

[95] L. Li, L. Sun, and J. Jin. Survey of advances in control algorithms of quadrotor unmanned aerial vehicle. In *2015 IEEE 16th International Conference on Communication Technology (ICCT)*, pages 107–111. IEEE, 2015.

[96] Y. Li and S. Song. A survey of control algorithms for quadrotor unmanned helicopter. In *2012 IEEE Fifth International Conference on Advanced Computational Intelligence (ICACI)*, pages 365–369. IEEE, 2012.

[97] C. K. R. Lim and D. Mba. Switching kalman filter for failure prognostic. *Mechanical Systems and Signal Processing*, 52:426–435, 2015.

[98] D. Liu, Y. Luo, J. Liu, Y. Peng, L. Guo, and M. Pecht. Lithium-ion battery remaining useful life estimation based on fusion nonlinear degradation ar model and rpf algorithm. *Neural Computing and Applications*, 25(3-4):557–572, 2014.

[99] D. Liu, Y. Luo, Y. Peng, X. Peng, and M. Pecht. Lithium-ion battery remaining useful life estimation based on nonlinear ar model combined with degradation feature. In *Annual Conference of the Prognostics and Health Management Society*, volume 3, pages 1803–1836, 2012.

[100] D. Liu, J. Pang, J. Zhou, and Y. Peng. Data-driven prognostics for lithium-ion battery based on gaussian process regression. In *Proceedings of the IEEE 2012 Prognostics and System Health Management Conference (PHM-2012 Beijing)*, pages 1–5. IEEE, 2012.

[101] D. Liu, J. Zhou, H. Liao, Y. Peng, and X. Peng. A health indicator extraction and optimization framework for lithium-ion battery degradation modeling and prognostics. *IEEE Transactions on Systems, Man, and Cybernetics: Systems*, 45(6):915–928, 2015.

[102] D. Liu, J. Zhou, D. Pan, Y. Peng, and X. Peng. Lithium-ion battery remaining useful life estimation with an optimized relevance vector machine algorithm with incremental learning. *Measurement*, 63:143–151, 2015.

[103] J. Liu, A. Saxena, K. Goebel, B. Saha, and W. Wang. An adaptive recurrent neural network for remaining useful life prediction of lithium-ion batteries. Technical report, NATIONAL AERONAUTICS AND SPACE ADMINISTRATION MOFFETT FIELD CA AMES RESEARCH ..., 2010.

[104] Z. Liu, G. Sun, S. Bu, J. Han, X. Tang, and M. Pecht. Particle learning framework for estimating the remaining useful life of lithium-ion batteries. *IEEE Transactions on Instrumentation and Measurement*, 66(2):280–293, 2017.

[105] T. Luukkonen. Modelling and control of quadcopter. *Independent research project in applied mathematics, Espoo*, 22, 2011.

[106] B. MacAllister, J. Butzke, A. Kushleyev, H. Pandey, and M. Likhachev. Path planning for non-circular micro aerial vehicles in constrained environments. In *Robotics and Automation (ICRA), 2013 IEEE International Conference on*, pages 3933–3940. IEEE, 2013.

[107] Q. Man, S. Ma, L. Xia, and Y. Wang. Research on security monitoring and health management system of medium-range uav. In *2009 8th International Conference on Reliability, Maintainability and Safety*, pages 854–857. IEEE, 2009.

[108] G. P. Mayuga, C. Favila, C. Oppus, E. Macatulad, and L. H. Lim. Airborne particulate matter monitoring using uavs for smart cities and urban areas. In *TENCON 2018-2018 IEEE Region 10 Conference*, pages 1398–1402. IEEE, 2018.

[109] J. Meyer, J. Du Plessis, P. Ellis, and W. Clark. Design considerations for a low altitude long endurance solar powered unmanned aerial vehicle. In *AFRICON 2007*, pages 1–7. IEEE, 2007.

[110] Q. Miao, L. Xie, H. Cui, W. Liang, and M. Pecht. Remaining useful life prediction of lithium-ion battery with unscented particle filter technique. *Microelectronics Reliability*, 53(6):805–810, 2013.

[111] M. Mishra, J. Martinsson, M. Rantatalo, and K. Goebel. Bayesian hierarchical model-based prognostics for lithium-ion batteries. *Reliability Engineering & System Safety*, 172:25–35, 2018.

[112] H. Mo and G. Farid. Nonlinear and adaptive intelligent control techniques for quadrotor uav–a survey. *Asian Journal of Control*, 2019.

[113] F. Morbidi, D. Bicego, M. Ryll, and A. Franchi. Energy-efficient trajectory generation for a hexarotor with dual-tilting propellers. In *2018 IEEE/RSJ International Conference on Intelligent Robots and Systems (IROS)*, pages 6226–6232. IEEE, 2018.

[114] F. Morbidi, R. Cano, and D. Lara. Minimum-Energy Path Generation for a Quadrotor UAV. In *IEEE International Conference on Robotics and Automation*, 2016.

[115] Y. Morel and A. Leonessa. Direct adaptive tracking control of quadrotor aerial vehicles. In *Conference on Recent Advances in Robotics*, pages 25–26, 2006.

[116] A. Mosallam, K. Medjaher, and N. Zerhouni. Data-driven prognostic method based on bayesian approaches for direct remaining useful life prediction. *Journal of Intelligent Manufacturing*, 27(5):1037–1048, 2016.

[117] O. Moseler and R. Isermann. Application of model-based fault detection to a brushless DC motor. *IEEE Transactions on Industrial Electronics*, 47(5):1015–1020, 2000.

[118] S. Musa. Techniques for quadcopter modeling and design: A review. *Journal of Unmanned System Technology*, 5(3):66–75, 2018.

[119] G.-A. Nazri and G. Pistoia. *Lithium batteries: science and technology*. Springer Science & Business Media, 2008.

[120] K. S. Ng, C.-S. Moo, Y.-P. Chen, and Y.-C. Hsieh. Enhanced coulomb counting method for estimating state-of-charge and state-of-health of lithium-ion batteries. *Applied energy*, 86(9):1506–1511, 2009.

[121] S. S. Ng, Y. Xing, and K. L. Tsui. A naive bayes model for robust remaining useful life prediction of lithium-ion battery. *Applied Energy*, 118:114–123, 2014.

[122] P. D. Nguyen, C. T. Recchiuto, and A. Sgorbissa. Real-time path generation and obstacle avoidance for multirotors: A novel approach. *Journal of Intelligent & Robotic Systems*, 89(1-2):27–49, 2018.

[123] C. Nicol, C. Macnab, and A. Ramirez-Serrano. Robust adaptive control of a quadrotor helicopter. *Mechatronics*, 21(6):927–938, 2011.

[124] M. E. Orchard and G. J. Vachtsevanos. A particle filtering-based framework for real-time fault diagnosis and failure prognosis in a turbine engine. In *2007 Mediterranean Conference on Control & Automation*, pages 1–6. IEEE, 2007.

[125] M. E. Orchard and G. J. Vachtsevanos. A particle-filtering approach for on-line fault diagnosis and failure prognosis. *Transactions of the Institute of Measurement and Control*, 31(3-4):221–246, 2009.

[126] J. P. Ortiz, L. I. Minchala, and M. J. Reinoso. Nonlinear robust h-infinity pid controller for the multivariable system quadrotor. *IEEE Latin America Transactions*, 14(3):1176–1183, 2016.

[127] G. Ortiz-Torres, P. Castillo, and J. Reyes-Reyes. An actuator fault tolerant control for vtol vehicles using fault estimation observers: Practical validation. In *2018 International Conference on Unmanned Aircraft Systems (ICUAS)*, pages 1054–1062. IEEE, 2018.

[128] G. Ortiz-Torres, C. Garcıa-Beltrán, J. Reyes-Reyes, A. Vidal-Rosas, and C. Astorga-Zaragoza. Control Tolerante a Fallas Pasivo de un Octorotor tipo X8 utilizando Controladores Backstepping en Cascada. pages 1–8, 2015.

[129] N. S. Özbek, M. Önkol, and M. Ö. Efe. Feedback control strategies for quadrotor-type aerial robots: a survey. *Transactions of the Institute of Measurement and Control*, 38(5):529–554, 2016.

[130] A. V. Parshin, V. A. Morozov, A. V. Blinov, A. N. Kosterev, and A. E. Budyak. Low-altitude geophysical magnetic prospecting based on multirotor uav as a promising replacement for traditional ground survey. *Geo-spatial Information Science*, 21(1):67–74, 2018.

[131] A. R. Patnaik, A. Nayak, V. Narasimhan, and P. C. Patnaik. An integrated phm approach for gas turbine engines. In *2006 Canadian Conference on Electrical and Computer Engineering*, pages 2476–2479. IEEE, 2006.

[132] M. A. Patterson and A. V. Rao. GPOPS-II: A MATLAB software for solving multiple-phase optimal control problems using hp-adaptive gaussian quadrature collocation methods and sparse nonlinear programming. *ACM Transactions on Mathematical Software (TOMS)*, 41(1):1, 2014.

[133] M. Pecht and J. Gu. Physics-of-failure-based prognostics for electronic products. *Transactions of the Institute of Measurement and Control*, 31(3-4):309–322, 2009.

[134] Y. Peng and M. Dong. A hybrid approach of hmm and grey model for age-dependent health prediction of engineering assets. *Expert Systems with Applications*, 38(10):12946–12953, 2011.

[135] D. Pinzón and C. Andres. Nonlinear model predictive control for aggressive maneuvers in a variable pitch quadrotor based on the extended modal series method. 2018.

[136] G. L. Plett. Extended kalman filtering for battery management systems of lipb-based hev battery packs: Part 3. state and parameter estimation. *Journal of Power sources*, 134(2):277–292, 2004.

[137] G. L. Plett. *Battery management systems, Volume I: Battery modeling*, volume 1. Artech House, 2015.

[138] G. L. Plett. *Battery management systems, Volume II: Equivalent-circuit methods*, volume 2. Artech House, 2015.

[139] P. Pounds, R. Mahony, J. Gresham, P. Corke, and J. M. Roberts. Towards dynamically-favourable quadrotor aerial robots. In *Proceedings of the 2004 Australasian Conference on Robotics & Automation*. Australian Robotics & Automation Association, 2004.

[140] A. Prach and E. Kayacan. An mpc-based position controller for a tilt-rotor tricopter vtol uav. *Optimal Control Applications and Methods*, 39(1):343–356, 2018.

[141] P. Pradeep, S. G. Park, and P. Wei. Trajectory optimization of multirotor agricultural uavs. In *2018 IEEE Aerospace Conference*, pages 1–7. IEEE, 2018.

[142] V. Praveen, S. Pillai, et al. Modeling and simulation of quadcopter using pid controller. *International Journal of Control Theory and Applications*, 9(15):7151–7158, 2016.

[143] A. Prayitno, V. Indrawati, and C. Arron. H-infinity control for pitch-roll ar. drone. *TELKOMNIKA Indonesian Journal of Electrical Engineering*, 14(3):963–973, 2016.

[144] Y. Quiñonez, F. Barrera, I. Bugueño, and J. Bekios-Calfa. Simulation and path planning for quadcopter obstacle avoidance in indoor environments using the ros framework. In *International Conference on Software Process Improvement*, pages 295–304. Springer, 2017.

[145] C. Richter, A. Bry, and N. Roy. Polynomial trajectory planning for aggressive quadrotor flight in dense indoor environments. In *Robotics Research*, pages 649–666. Springer, 2016.

[146] H. Ríos, R. Falcón, O. A. González, and A. Dzul. Continuous sliding-mode control strategies for quadrotor robust tracking: real-time application. *IEEE Transactions on Industrial Electronics*, 66(2):1264–1272, 2018.

[147] U. A. V. Roadmap. Roadmap 2002-2027. *US DoD, December*, 2002.

[148] J. F. Roberts, J.-C. Zufferey, and D. Floreano. Energy management for indoor hovering robots. In *2008 IEEE/RSJ International Conference on Intelligent Robots and Systems*, pages 1242–1247. IEEE, 2008.

[149] M. Roemer, L. Tang, S. Bharadwaj, and C. Belcastro. An integrated aircraft health assessment and fault contingency management system for aircraft. In *AIAA Guidance, Navigation and Control Conference and Exhibit*, page 6505, 2008.

[150] M. J. Roemer, G. J. Kacprzynski, and R. F. Orsagh. Assessment of data and knowledge fusion strategies for prognostics and health management. In *2001 IEEE Aerospace Conference Proceedings (Cat. No. 01TH8542)*, volume 6, pages 2979–2988. IEEE, 2001.

[151] D. Rotondo, F. Nejjari, and V. Puig. Robust quasi–lpv model reference ftc of a quadrotor uav subject to actuator faults. *International Journal of Applied Mathematics and Computer Science*, 25(1):7–22, 2015.

[152] I. Sadeghzadeh, A. Chamseddine, Y. Zhang, and D. Theilliol. Control allocation and re-allocation for a modified quadrotor helicopter against actuator faults. *IFAC Proceedings Volumes*, 45(20):247–252, 2012.

[153] B. Saha and K. Goebel. Battery data set. *NASA AMES prognostics data repository*, 2007.

[154] B. Saha and K. Goebel. Modeling li-ion battery capacity depletion in a particle filtering framework. In *Proceedings of the annual conference of the prognostics and health management society*, pages 2909–2924. San Diego, 2009.

[155] B. Saha, E. Koshimoto, C. C. Quach, E. F. Hogge, T. H. Strom, B. L. Hill, S. L. Vazquez, and K. Goebel. Battery health management system for electric uavs. In *Aerospace Conference, 2011 IEEE*, pages 1–9. IEEE, 2011.

[156] S. Saha, B. Saha, A. Saxena, and K. Goebel. Distributed prognostic health management with gaussian process regression. In *2010 IEEE Aerospace Conference*, pages 1–8. IEEE, 2010.

[157] M. Santos, V. Lopez, and F. Morata. Intelligent fuzzy controller of a quadrotor. In *2010 IEEE International Conference on Intelligent Systems and Knowledge Engineering*, pages 141–146. IEEE, 2010.

[158] T. Sasaki, Y. Ukyo, and P. Novák. Memory effect in a lithium-ion battery. *Nature Materials*, 12(6):569, 2013.

[159] B. Satish and N. Sarma. A fuzzy bp approach for diagnosis and prognosis of bearing faults in induction motors. In *IEEE Power Engineering Society General Meeting, 2005*, pages 2291–2294. IEEE, 2005.

[160] C. Sbarufatti, M. Corbetta, M. Giglio, and F. Cadini. Adaptive prognosis of lithium-ion batteries based on the combination of particle filters and radial basis function neural networks. *Journal of Power Sources*, 344:128–140, 2017.

[161] R. Schacht-Rodríguez, J. Ponsart, D. Theilliol, C. García-Beltrán, and C. Astoraa-Zaragoza. Path planning based on state-of-health of the power source for a class of multirotor uavs. In *2018 UKACC 12th International Conference on Control (CONTROL)*, pages 309–314. IEEE, 2018.

[162] R. Schacht-Rodríguez, J.-C. Ponsart, C. García-Beltrán, and C. Astorga-Zaragoza. Prognosis & health management for the prediction of uav flight endurance. *IFAC-PapersOnLine*, 51(24):983–990, 2018.

[163] R. Schacht-Rodríguez, J.-C. Ponsart, C.-D. García-Beltrán, and C.-M. Astorga-Zaragoza. Mission planning strategy for multirotor uav based on flight endurance estimation. *In 2019 International Conference on Unmanned Aircraft Systems, ICUAS 2019*, 2019.

[164] R. Schacht-Rodríguez, J.-C. Ponsart, C.-D. García-Beltrán, C.-M. Astorga-Zaragoza, D. Theilliol, and Y. Zhang. Path planning generation algorithm for a class of uav multirotor based on state of health of lithium polymer battery. *Journal of Intelligent & Robotic Systems*, 91(1):115–131, 2018.

[165] T. Schneider, G. Ducard, K. Rudin, and P. Strupler. Fault-tolerant control allocation for multirotor helicopters using parametric programming. *rN*, 1:r2, 2012.

[166] M. Schwabacher. A survey of data-driven prognostics. In *Infotech@ Aerospace*, page 7002. 2005.

[167] M. Schwabacher and K. Goebel. A survey of artificial intelligence for prognostics. In *Aaai fall symposium*, pages 107–114, 2007.

[168] Y. B. Sebbane. *Planning and decision making for aerial robots*. Springer, 2014.

[169] H. Seker, M. O. Odetayo, D. Petrovic, and R. N. G. Naguib. A fuzzy logic based-method for prognostic decision making in breast and prostate cancers. *IEEE Transactions on Information Technology in Biomedicine*, 7(2):114–122, 2003.

[170] Y. Shao and K. Nezu. Prognosis of remaining bearing life using neural networks. *Proceedings of the Institution of Mechanical Engineers, Part I: Journal of Systems and Control Engineering*, 214(3):217–230, 2000.

[171] M. F. Shehzad, A. Bilal, and H. Ahmad. Position & attitude control of an aerial robot (quadrotor) with intelligent pid and state feedback lqr controller: A comparative approach. In *2019 16th International Bhurban Conference on Applied Sciences and Technology (IBCAST)*, pages 340–346. IEEE, 2019.

[172] J. W. Sheppard, M. A. Kaufman, and T. J. Wilmering. Ieee standards for prognostics and health management. In *2008 IEEE AUTOTESTCON*, pages 97–103. IEEE, 2008.

[173] J.-L. Shi, D.-D. Xiao, M. Ge, X. Yu, Y. Chu, X. Huang, X.-D. Zhang, Y.-X. Yin, X.-Q. Yang, Y.-G. Guo, et al. High-capacity cathode material with high voltage for li-ion batteries. *Advanced Materials*, 30(9):1705575, 2018.

[174] H. Shraim, A. Awada, and R. Youness. A survey on quadrotors: Configurations, modeling and identification, control, collision avoidance, fault diagnosis and tolerant control. *IEEE Aerospace and Electronic Systems Magazine*, 33(7):14–33, 2018.

[175] R. Silva, R. Gouriveau, S. Jemei, D. Hissel, L. Boulon, K. Agbossou, and N. Y. Steiner. Proton exchange membrane fuel cell degradation prediction based on adaptive neuro-fuzzy inference systems. *International Journal of Hydrogen Energy*, 39(21):11128–11144, 2014.

[176] E. Stingu and F. L. Lewis. A hardware platform for research in helicopter uav control. In *Unmanned Aircraft Systems*, pages 387–406. Springer, 2008.

[177] X. Su, S. Wang, M. Pecht, L. Zhao, and Z. Ye. Interacting multiple model particle filter for prognostics of lithium-ion batteries. *Microelectronics Reliability*, 70:59–69, 2017.

[178] K. E. Swider-Lyons, J. A. MacKrell, J. A. Rodgers, G. S. Page, M. Schuette, and R. O. Stroman. Hydrogen fuel cell propulsion for long endurance small uavs. In *The AIAA centennial of naval aviation forum*, volume 100, 2011.

[179] S. Tang, C. Yu, X. Wang, X. Guo, and X. Si. Remaining useful life prediction of lithium-ion batteries based on the wiener process with measurement error. *Energies*, 7(2):520–547, 2014.

[180] P. Tokekar, N. Karnad, and V. Isler. Energy-optimal trajectory planning for car-like robots. *Autonomous Robots*, 37(3):279–300, 2014.

[181] L. W. Traub. Range and endurance estimates for battery-powered aircraft. *Journal of Aircraft*, 48(2):703–707, 2011.

[182] G. Vachtsevanos, L. Tang, G. Drozeski, and L. Gutierrez. From mission planning to flight control of unmanned aerial vehicles: Strategies and implementation tools. *Annual Reviews in Control*, 29(1):101–115, 2005.

[183] M. Valenti, B. Bethke, J. P. How, D. P. De Farias, and J. Vian. Embedding health management into mission tasking for uav teams. In *American Control Conference, 2007. ACC'07*, pages 5777–5783. IEEE, 2007.

[184] J. Van Tooren, H. Martin, A. Knoll, and B. Johannes. Collision and conflict avoidance system for autonomous unmanned air vehicles (uavs), June 15 2010. US Patent 7,737,878.

[185] J. Verbeke, D. Hulens, H. Ramon, T. Goedeme, and J. De Schutter. The design and construction of a high endurance hexacopter suited for narrow corridors. In *Unmanned Aircraft Systems (ICUAS), 2014 International Conference on*, pages 543–551. IEEE, 2014.

[186] H. Voos. Nonlinear control of a quadrotor micro-uav using feedback-linearization. In *2009 IEEE International Conference on Mechatronics*, pages 1–6. IEEE, 2009.

[187] C. Wang, B. Song, P. Huang, and C. Tang. Trajectory tracking control for quadrotor robot subject to payload variation and wind gust disturbance. *Journal of Intelligent & Robotic Systems*, 83(2):315–333, 2016.

[188] D. Wang, Q. Miao, and M. Pecht. Prognostics of lithium-ion batteries based on relevance vectors and a conditional three-parameter capacity degradation model. *Journal of Power Sources*, 239:253–264, 2013.

[189] J. Wang, J. Ding, W. Cao, Q. Li, and H. Zhao. Neural network fuzzy control for enhancing the stability performance of quad-rotor helicopter. *Transactions of the Institute of Measurement and Control*, 40(11):3333–3344, 2018.

[190] J. Wang, R. X. Gao, Z. Yuan, Z. Fan, and L. Zhang. A joint particle filter and expectation maximization approach to machine condition prognosis. *Journal of Intelligent Manufacturing*, 30(2):605–621, 2019.

[191] S. Wang, L. Zhao, X. Su, and P. Ma. Prognostics of lithium-ion batteries based on battery performance analysis and flexible support vector regression. *Energies*, 7(10):6492–6508, 2014.

[192] Z.-Q. Wang, C.-H. Hu, W. Wang, and X.-S. Si. An additive wiener process-based prognostic model for hybrid deteriorating systems. *IEEE Transactions on Reliability*, 63(1):208–222, 2014.

[193] N. Watrin, B. Blunier, and A. Miraoui. Review of adaptive systems for lithium batteries State-of-Charge and State-of-Health estimation. In *2012 IEEE Transportation Electrification Conference and Expo (ITEC)*, pages 1–6. IEEE, 2012.

[194] W. Xian, B. Long, M. Li, and H. Wang. Prognostics of lithium-ion batteries based on the verhulst model, particle swarm optimization and particle filter. *IEEE Transactions on Instrumentation and Measurement*, 63(1):2–17, 2014.

[195] Y. Xing, E. W. Ma, K.-L. Tsui, and M. Pecht. A case study on battery life prediction using particle filtering. In *Proceedings of the IEEE 2012 Prognostics and System Health Management Conference (PHM-2012 Beijing)*, pages 1–6. IEEE, 2012.

[196] F. Yacef, N. Rizoug, L. Degaa, O. Bouhali, and M. Hamerlain. Trajectory optimisation for a quadrotor helicopter considering energy consumption. In *Control, Decision and Information Technologies (CoDIT), 2017 4th International Conference on*, pages 1030–1035. IEEE, 2017.

[197] W. Yan, B. Zhang, G. Zhao, S. Tang, G. Niu, and X. Wang. A battery management system with a lebesgue-sampling-based extended kalman filter. *IEEE Transactions on Industrial Electronics*, 66(4):3227–3236, 2019.

[198] S. Yin, J. Pang, D. Liu, and Y. Peng. Remaining useful life prognostics for lithium-ion battery based on gaussian processing regression combined with the empirical model. In *Proceedings of the Second Second European Conference of the Prognostics and Health Management Society*, pages 1–8, 2013.

[199] C. Yuan, Y. Zhang, and Z. Liu. A survey on technologies for automatic forest fire monitoring, detection, and fighting using unmanned aerial vehicles and remote sensing techniques. *Canadian journal of forest research*, 45(7):783–792, 2015.

[200] H. Zhang, Q. Miao, X. Zhang, and Z. Liu. An improved unscented particle filter approach for lithium-ion battery remaining useful life prediction. *Microelectronics Reliability*, 81:288–298, 2018.

[201] Y. Zhang, X. Zhao, W. Liu, J. Zhang, Y. Jia, and T. Feng. Research on gearbox wearing prognosis based on gamma-state space model. In *The Proceedings of 2011 9th International Conference on Reliability, Maintainability and Safety*, pages 279–283. IEEE, 2011.

[202] Z. Zhang, X. Si, C. Hu, and Y. Lei. Degradation data analysis and remaining useful life estimation: A review on wiener-process-based methods. *European Journal of Operational Research*, 271(3):775–796, 2018.

[203] G. Zhao, G. Zhang, Y. Liu, B. Zhang, and C. Hu. Lithium-ion battery remaining useful life prediction with deep belief network and relevance vector machine. In *2017 IEEE International Conference on Prognostics and Health Management (ICPHM)*, pages 7–13. IEEE, 2017.

[204] R. Zhao, R. Yan, Z. Chen, K. Mao, P. Wang, and R. X. Gao. Deep learning and its applications to machine health monitoring. *Mechanical Systems and Signal Processing*, 115:213–237, 2019.

[205] F. Zheng, J. Jiang, M. A. Zaidan, W. He, and M. Pecht. Prognostics of lithium-ion batteries using a deterministic bayesian approach. In *2015 IEEE Conference on Prognostics and Health Management (PHM)*, pages 1–4. IEEE, 2015.

[206] Z.-J. Zhou, C.-H. Hu, D.-L. Xu, M.-Y. Chen, and D.-H. Zhou. A model for real-time failure prognosis based on hidden markov model and belief rule base. *European Journal of Operational Research*, 207(1):269–283, 2010.

[207] E. Zio and G. Peloni. Particle filtering prognostic estimation of the remaining useful life of nonlinear components. *Reliability Engineering & System Safety*, 96(3):403–409, 2011.

[208] A. W. Zollitsch, N. C. Mumm, F. Holzapfel, and J. Schumann. System health management for safe automatic take-off. In *AIAA Scitech 2019 Forum*, page 1960, 2019.

[209] A. Zulu and S. John. A review of control algorithms for autonomous quadrotors. *arXiv preprint arXiv:1602.02622*, 2016.